

**INTELLIGENT MEDICAL DIAGNOSTIC SYSTEM FOR  
RHEUMATOID ARTHRITIS**

Thesis Submitted For the Award of the Degree of

**DOCTOR OF PHILOSOPHY**

**in**

**COMPUTER SCIENCE AND ENGINEERING**

By

**Sujeet More**

**11816272**

Supervised By

**Dr. Jimmy Singla**



**LOVELY PROFESSIONAL UNIVERSITY**

**PUNJAB**

**2022**

## **DECLARATION**

I hereby declare that the thesis entitled "Intelligent Medical Diagnostic System for Rheumatoid Arthritis" submitted by me for the Degree of Doctor of Philosophy in Computer Science and Engineering is the result of my original and independent research work carried out under the guidance of Dr. Jimmy Singla, Associate Professor, Department of Computer Science and Engineering, Lovely Professional University, Punjab, and it has not been submitted for the award of any degree, diploma, associateship, fellowship of any University or Institution.

Sujeet More

(Registration Number: 11816272)

School of Computer Science and Engineering,

Lovely Professional University,

Phagwara, Punjab-144411,

India

Date:

## **CERTIFICATE**

This is to certify that the thesis entitled " Intelligent Medical Diagnostic System for Rheumatoid Arthritis " submitted by Sujeet More for the award of the degree of Doctor of Philosophy in Computer Science and Engineering, Lovely Professional University, is entirely based on the work carried out by him under my supervision and guidance. The work reported, embodies the original work of the candidate and has not been submitted to any other university or institution for the award of any degree or diploma, according to the best of my knowledge.

Dr. Jimmy Singla  
Associate Professor  
School of Computer Science and Engineering,  
Lovely Professional University,  
Phagwara, Punjab-144411,  
India  
Date:

## ABSTRACT

Rheumatoid arthritis (RA) is an autoimmune or chronic disease that can cause damage to various joints such as knee, hands, spine, etc, in the body. This damage to knee joint can cause temporary or permanent stiffness and tenderness of joints. The assessment of knee RA can be performed based on changes and gradual loss of cartilage, meniscus, and synovial fluid. Its early assessment is necessary to stop further degradation of cartilage and other tissues. For early diagnosis of knee RA morphological and volumetric assessment such as joint space narrowing, volume, and thickness of tissues are suitable parameters. Till date magnetic resonance imaging (MRI) has proven to be better with exceptional outcome but with few limitations. These limitations are in terms of noise, weak tissue boundaries, and structural RA poorly characterized. Due to increasing vagueness and complexities, deriving information becomes challenge for the physicians. This challenge could lead to imprecise assessment and inaccurate diagnosis to the patients. Therefore, to avoid these uncertainties an intelligent diagnostic system must be developed to overcome the complex RA evaluation process.

This motivates research to develop intelligent system to aid RA diagnosis from knee MRI and analyse their performance with statistical parameters. The methods proposed in this thesis use machine learning to characterise large volume of RA dataset with one experiment applying an algorithm over 10,000 images. A novel noise reduction technique called as sparse aware noise reduction convolutional neural network is proposed in this thesis that reduces noise, preserving the internal structure of the image. A dictionary is generated during training phase to reduce the computational time for testing.

To overcome other difficulties in early prediction of RA, the thesis also proposes segmentation and feature extraction technique. Feature extraction and segmentation is performed using discrete wavelet transform (DWT) and MultiResUNet architecture, respectively. The method rearranges the data giving threshold to the wavelet coefficient using DWT. In the proposed MultiResUNet architecture the convolutional

network layers are replaced by MultiRes blocks with Res path. The knee tissues are segmented based on intensity levels such as cartilage and synovial fluid are segmented at foreground and bone tissue and meniscus at background. The diagnosis or prediction of RA is carried out with ResNet50 with fifty layers of neural network for precise outcome. The performance of proposed method is assessed in terms of qualitative and quantitative parameters on T1-weighted, T2-weighted and FLAIR MR images of 193 subjects. Various parameters such as peak signal to noise ratio (PSNR), structural similarity index (SSIM), dice similarity coefficient (DSC), root mean square distance (RMSD), sensitivity, specificity, and other performance parameters are estimated comparing with ground truth by expert rheumatologists. Experimental outcomes prove the credibility of proposed model in performing diagnosis and classification of RA with different severity levels assessing physicians with limited number of resources.

## ACKNOWLEDGEMENT

First and foremost, I wish to thank my supervisor, Dr. Jimmy Singla, for his continued encouragement and invaluable suggestions during this work. Ever since, Dr. Jimmy Singla has supported me not only by providing a research assistantship over these years, but also academically and emotionally through the rough road to finish this thesis. He helped me come up with the thesis topic and guided me over almost three years of development. And during the most difficult time of my life when my dad deceased, he gave me the moral support and the freedom I needed to move on. His unflinching courage and conviction will always inspire me, and I hope to continue to work with his noble thoughts

I wish to thank the doctoral committee members for providing valuable suggestions and comments for the improvement of my research work. I wish to express my sincere thanks to the management and staff of Division of Research and Development, Lovely Professional University, for extending the support and facilities to carry out my research work. It's my fortune to gratefully acknowledge the support of some special individuals in life. I would also like to say a heartfelt thank you to my parents for always believing in me, encouraging me to follow my dreams and helping me in financial crunch situations. I thank my brother for celebrating each accomplishment and for helping in whatever way he could during this challenging period. Lastly, I wish to thank my wife for being with me in ups and downs of life, for withstanding my frustration at times and helping me get through this period in the most positive way.

Finally, I thank God, you are the one who let me finish my degree, I will keep on trusting you for my future. Thank you, Lord.

## Table of Contents

Declaration .....	i
Certificate .....	ii
Abstract .....	iii
Acknowledgement .....	v
Table of Contents .....	vi
List of Tables .....	ix
List of Figures .....	x
List of Abbreviations .....	xii
<b>Chapter 1 Introduction</b>	
Medical Background .....	1
Knee Structure and Epidemiology .....	2
Tissues Affected and Detection of Rheumatoid Arthritis .....	4
Magnetic Resonance Imaging .....	5
Significance of Intelligent Medical Diagnostic Systems .....	9
Motivation .....	11
Problem Statement .....	12
Objectives of the Research .....	12
Approach of the Study .....	12
MR Image Dataset .....	13
Architecture Assessment Parameters .....	14
Outline of the Thesis .....	19
<b>Chapter 2 Literature Review</b>	
Introduction .....	21
Challenges in Assessment from MR Image .....	23
Image Artifacts .....	23
Image Properties .....	24
Tissue Structure .....	25
MR Pulse Sequence .....	26
Magnetic Field Strength .....	27

Introduction to Machine Learning .....	28
Machine Learning Paradigms .....	28
Supervised Learning .....	29
Unsupervised Learning .....	30
Reinforcement Learning .....	31
Deep Learning .....	32
Convolutional Neural Network .....	33
Feature Learning .....	35
Noise Model .....	36
Gaussian Noise .....	36
Brownian Noise .....	37
Impulse (Salt and Pepper) Noise .....	37
Rician Noise .....	37
Quantization Noise .....	38
Speckle Noise .....	38
Photon Noise .....	38
Poisson-Gaussian Noise .....	39
Structured Noise .....	39
Pre-processing Techniques for Knee MR Images .....	39
Segmentation and Feature Extraction Approaches .....	47
Manual Techniques .....	47
Semi-Automatic Techniques .....	48
Automatic Techniques .....	53
Feature Extraction Techniques .....	59
Diagnostic and Grading Approaches .....	64
Observations .....	69
Conclusion .....	72
<b>Chapter 3 Denoising MR Images Using Sparse Aware Noise Reduction with Convolutional Neural Network and Dictionary Learning</b>	
Need of Pre-processing .....	73
Introduction .....	74
Noise Distribution .....	76



Pre-processing of Knee MR Images .....	77
Denoising of Knee MR Image using SANR_CNN .....	78
Dictionary Learning .....	79
Results and Discussions .....	81
Conclusion .....	86
<b>Chapter 4 Automatic Segmentation and Feature Extraction of Knee MR Images using Hybrid Architecture</b>	
Introduction .....	87
Methodology .....	89
Discrete-MultiResUNet Architecture .....	90
Initialization of Bone Region Extraction .....	91
Boundary Leakage Correction .....	93
Feature Extraction using DWT .....	95
Masking .....	99
Performance Evaluation and Discussions .....	101
Conclusion .....	106
<b>Chapter 5 Automatic Classification of Rheumatoid Arthritis with KL Grading</b>	
Introduction .....	107
Methodology .....	109
ResNet50 Architecture .....	110
Adam Optimization Technique .....	114
Results and Discussions .....	116
Conclusion .....	121
<b>Chapter 6 Conclusion and Future Scope</b>	
Summary of Deductions .....	122
Future Scope of Work .....	123
<b>List of Publications</b>	125
<b>Bibliography</b>	127

## List of Tables

1.1 Difference Between Medical Modalities .....	6
1.2 TR and TE Time for MR Image Sequences .....	8
1.3 MR Image Dataset Specification .....	14
2.1 Pre-processing Techniques with Input and Output Parameters .....	42
2.2 Semi-automatic Segmentation Techniques for Knee MR Images .....	50
2.3 Automatic Segmentation Techniques for Knee MR Images .....	54
2.4 Quantitative Evaluation of RA Knee Features .....	59
2.5 List of Features Selected for Knee RA .....	62
2.6 Classification Techniques with KL Grading for Knee MR Images .....	65
2.7 Techniques Applied for Arthritis Disease .....	70
2.8 KL Grading for Arthritis Progression .....	71
3.1 Quantitative Parameters with Trials .....	82
3.2 Comparative Analysis of PSNR Value .....	82
3.3 Comparative Analysis of SSIM Value .....	83
3.4 Comparative Analysis of MSE Value .....	83
3.5 Comparative Analysis of EM Value .....	84
3.6 Computational Time for Different Techniques .....	84
4.1 DSC, ASD, and RMSD Value for Local Dataset .....	104
4.2 DSC, ASD, and RMSD Value for OAI Dataset .....	104
4.3 Assessment of Meniscus for Knee MR Images .....	105
5.1 ResNet50 Architecture Layer Description .....	113
5.2 Datasets Used for Experimental Analysis .....	117
5.3 Different Performance Parameters with KL Grade on Local Dataset ....	117
5.4 Different Performance Parameters with KL Grade on OAI Dataset .....	118
5.5 Comparative Analysis of Different Techniques Related to Lateral and Medial Femoral and Tibial Tissue with JSN Value .....	118
5.6 Performance Parameters Achieved for Proposed Model .....	119

## List of Figures

1.1 Difference Between Normal and Health Knee .....	2
1.2 Knee Structure .....	3
1.3 Knee Joint Affected by RA .....	5
1.4 Knee MR Image Types .....	8
1.5 Knee MR Images Views .....	9
1.6 Representation of TP, TN, FP, and FN .....	16
2.1 Healthy Knee Joint .....	22
2.2 Artifacts Induced in MR Images .....	24
2.3 Volume Effect in MR Images .....	24
2.4 Low Visibility Contrast of MR Sequences .....	25
2.5 Irregular Shape of Knee Structure .....	26
2.6 MR Pulse Sequences .....	27
2.7 Classification Process .....	29
2.8 General Classification Model .....	30
2.9 Confusion Matrix .....	30
2.10 K Means Clustering .....	31
2.11 Reinforcement Learning .....	32
2.12 CNN Architecture .....	33
2.13 Denoising Techniques Based on Convolutional Neural Network .....	41
2.14 Manual Segmentation Architecture .....	48
2.15 Manually Segmented Femoral and Tibial Cartilage from MR Image .....	48
2.16 Semi-automatic Segmentation Process .....	49
2.17 Automatic Segmentation Process .....	53
3.1 Challenges in MR Images .....	74
3.2 Proposed Sparse Aware Noise Removal using Convolutional Neural Network (SANR_CNN) Architecture .....	78

3.3 Proposed Dilated Convolutional Neural Network Architecture .....	78
3.4 Denoised Knee MR Images Achieved with SANR_CNN .....	85
3.5 Computational Time Estimated for Comparative Techniques .....	85
4.1 Different Views of Knee MR Image (Sagittal View) .....	88
4.2 Multi-level Architecture for Automatic Segmentation and Feature Extraction.	89
4.3 MR Slice with Edge Detection .....	90
4.4 Proposed Segmentation Architecture .....	90
4.5 Slices Consisting of Bone and No-Bone Region .....	92
4.6 Bone Region Extraction .....	92
4.7 2D Discrete Wavelet Transform .....	96
4.8 Knee MR Image with 2-level Wavelet Decomposition .....	97
4.9 Automatic Seed Point Selection and Bone Region Extraction .....	101
4.10 Boundary Correction and Segmentation Overlaid Images .....	102
4.11 Masked MR Images Surrounded by Bone Tissues .....	103
5.1 KL Grading Stages for Knee RA .....	108
5.2 Proposed Classification Framework with KL Grading .....	110
5.3 Skip Connection Used in ResNet Architecture .....	111
5.4 Identity Block in ResNet Architecture .....	111
5.5 Convolutional Block in ResNet Architecture .....	112
5.6 Confusion Matrix for Proposed Architecture .....	120

## List of Abbreviations

CT	Computed Tomography
MRI	Magnetic Resonance Imaging
RA	Rheumatoid Arthritis
RF	Radio Frequency
TR	Repetition Time
TE	Time to Echo
PSNR	Peak to Signal Noise Ratio
SSIM	Structural Similarity Index
MSE	Mean Squared Error
MAE	Mean Absolute Error
DESS	Dual Echo Steady State
SSFP	Steady State Free Precision
FISP	Fast Imaging Steady State Precision
IMDS	Intelligent Medical Diagnostic System
SVM	Support Vector Machine
DT	Decision Tree
KNN	K-Nearest Neighbor
NN	Neural Network
PCA	Principal Component Analysis
ICA	Independent Component Analysis
TDL	Temporal Difference Learning
SARSA	State Action Reward State Action
KB	Knowledge Base
ANN	Artificial Neural Network
ML	Machine Learning
DL	Deep Learning
CNN	Convolutional Neural Network
OAI	Osteoarthritis Initiative
FOV	Field of View

FA	Flip Angle
ST	Slice Thickness
MS	Matrix Size
BW	Bandwidth
EM	Enhancement Measure
DSC	Dice Similarity Coefficient
VD	Volumetric Difference
VOE	Volume Overlap Error
RMSD	Root Mean Squared Error
ASD	Average Surface Distance
TP	True Positive
TN	True Negative
FP	False Positive
FN	False Negative
MSD	Mean Surface Distance
ROI	Region of Interest
JSN	Joint Space Narrowing
JSW	Joint Space Width
ARA	American Rheumatism Association
PD	Proton Density
SPGR	Spoil Gradient Echo
MFS	Magnetic Field Strength
ST	Scan Time
CS	Computer Science
ROC	Receiver Operating Characteristic
AUC	Area Under Curve
DNN	Deep Neural Network
RNN	Recurrent Neural Network
DSN	Deep Stacked Network
ReLU	Rectified Linear Unit
GMM	Gaussian Mixture Model
RF	Random Forest

JD-CNN	Joint Denoising Convolutional Neural Network
SToRM	Smoothness Regularizations on Manifolds
GAN	Generative Adversarial Network
CPMD	Clean Pixel Median Deviation
EPD	Edge Pixel Difference
GS	Gerchberg Saxton
DSSBPNNet	Deep Spatio-Spectral Bayesian Posterior Network
FEB	Feature Extraction Block
SCNAB	Spatial Channel Noise Attention Block
BN	Batch Normalization
CGAN	Conditional Generative Adversarial Network
DWT-SVD	Discrete Wavelet Transform Singular Value Decomposition
SWT	Stationary Wavelet Transform
AIR-AHE	Average Intensity Replacement Based Adaptive Histogram Equalization
LREK	Local Regional Information on Expandable Kernel
LSLSM	Locally Statistically Level Set Method
VFC	Vector Field Convolution
GVF	Gradient Vector Flow
SSM	Statistical Shape Model
HMT	Hit or Miss Transform
AAM	Active Appearance Model
ACL	Anterior Cruciate Ligament
ELM	Extreme Learning Method
HOG	Histogram Oriented Gradient
HNN	Holistically Nested Network
KL	Kellgren and Lawrence
SWNN	Simple Weighted Nearest Neighbor
LSTM	Long Short-Term Memory
VGG	Visual Geometry Group
MLEAA	Machine Learning based Ensemble Analytic Approach

SANR_CNN	Sparse Aware Noise Reduction using Convolutional Neural Network
NLM	Non-local mean filter



# Chapter 1

## Introduction

This chapter provides an overview of research presented in the thesis. Section 1.1 discusses the medical background. Section 1.2 provides a detailed information about significance of intelligent systems. The motivation behind this proposed model is presented in Section 1.3. Section 1.4 defines the problem statement. Section 1.5 describes the research objectives. Section 1.6 provides contribution of the thesis. A brief introduction about content of each chapter is outlined in Section 1.7.

### 1.1 Background of Study

Arthritis is joint inflammation featuring disorder of joints with wear and tear of tissues. In arthritis, common types are Osteoarthritis and rheumatoid arthritis. Firstly, Osteoarthritis causes degrading of cartilage, ligaments, and joints. Secondly, Rheumatoid arthritis (RA) is a chronic, inflammatory, and systematic autoimmune disorder that mainly affects the tissue regions such as (knee, spine, and hands) that causes erosion. The term rheumatoid comes from a Greek word meaning “flowing current”, indicates flow of pain and swelling in the entire body. Y. Tanaka defines RA as, “Rheumatoid arthritis is an autoimmune inflammatory disease primarily characterized by synovitis commonly affecting woman in their 30s and 50s accompanied by multi-organ disorder, pain swelling, and stiffness of multiple joints” [1].

RA was first investigated in 1800 by a physician with severe joint pain mainly affected women often than men. Many studies have shown that genetics is not only sole determinant for RA, but there are many triggering roles such as cartilage thickness, meniscus and synovial fluid volume, tissue structure, thickness, erosion etc. Pain, inflammation, limited joint movement are the symptoms for RA. Pain is primary in the joint through activity, but as RA progresses it may be observed with minimal movement or even while resting. Joint space narrowing, damage of tissues can be observed as underlying feature in RA. RA commonly affects the joints of the knee, finger, spine, shoulder as shown in figure 1.1. Figure 1.1 illustrates the knee structure

affected by RA and comparison of normal knee with RA affected knee. The treatment and response vary from person to person: some develop mild problems and other develop disability.

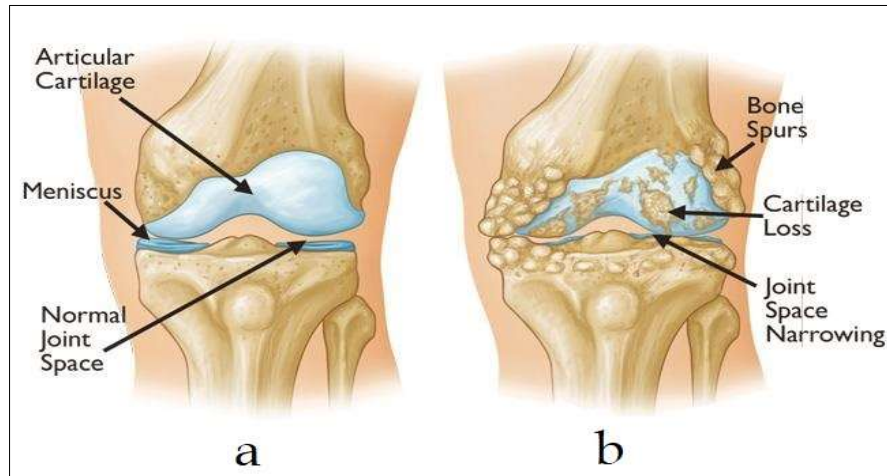


Fig. 1.1 (a) Normal and healthy knee (b) Rheumatoid arthritis knee(Source: OrthoInfo)

### 1.1.1 Knee Structure and Epidemiology

The section presents the data prevalence of RA and especially considering various factors associated with it. The occurrence of RA increases with age and commonly affects women more than men. RA affects joints of knee, finger, hips, and shoulder, but common in knee[2][3]. The RA has affected 44 million people globally with 18% of women and 9% of men aged over 50 years have symptomatic RA. It is estimated that nearly 78 million people may be affected by RA around 2045[4]. It is reported that the prevalence of RA in India is 22% to 39%. The data presented here varies accordingly with gender, weight, lifestyle, etc.

The epidemiology data[5] presented that the knee RA is high worldwide and increases day-by-day. The development of knee RA is due to heterogenous conditions involving all components of joint associated with cartilage, fluids present between tissue and joint erosions[6]. Thus, it is important to understand the structure of knee and various symptoms in knee RA. The human knee is the major tissue region in the body consists of two joints one between femur and tibia, another between femur and patella. The knee is helpful for functional movement and for performing daily activities. Knee is

composed of several hard tissues such as femur, tibia, patella, fibula, and soft tissues such as cartilage, ligaments, synovial fluid, meniscus[6][7]. Understanding anatomical structure is important before proceeding to RA.

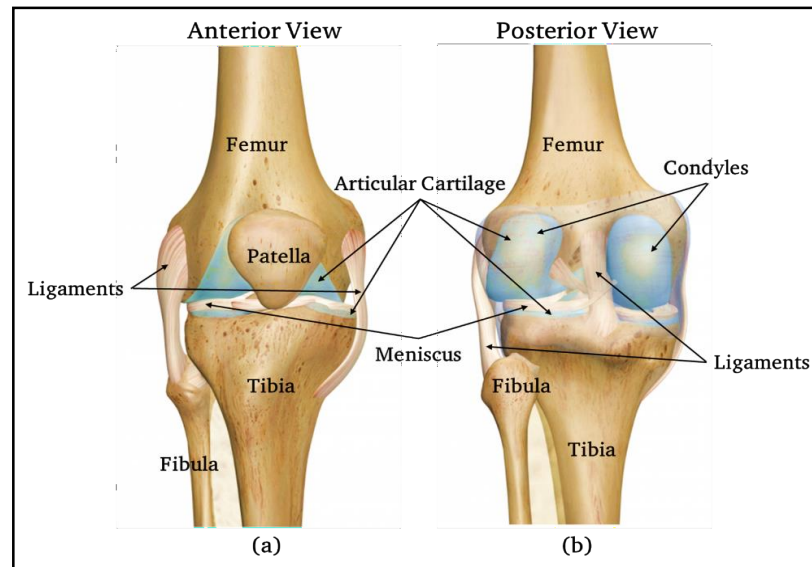


Fig. 1.2 Knee structure (a) anterior view (b) posterior view (Source: OrthoInfo)

### ***Bones***

The knee structure consists of four bones femur, tibia, patella, and fibula [8] as shown in figure 1.2. It is the bones that provides strength, flexibility to the knee joint. Femoral tissue is known as thigh bone; it is the toughest and biggest bone in the human body. Tibia is also known as shin bone that starts from knee joint to ankle joint. Patella is also known as kneecap, that is wedge shaped bone provides movement to the leg. The patella is attached to femoris muscles facilitating strength increasing movement. Fibula is thin bone that runs alongside tibia from knee joint to ankle joint.

### ***Cartilage***

Cartilages is smooth elastic tissue that covers and protects the joint of the bones. Cartilage is composed of cells known as chondrocytes that produces large number of elastic fibers. In posterior view round knobs like structure at the end of the bone called as condyles. Another type of cartilage in knee joint is meniscus that acts as cushion performing shock absorption task.

## ***Ligaments***

Ligaments are the link and fibrous connectivity between bone to bone ensuring the knee joint is resistant and stable, as shown in figure 1.2. Ligaments are not flexible but strong tough bands that stay stretched and retains their original shape. Ligaments are divided into different types such as medial ligament, lateral ligament, anterior ligament, and posterior ligament.

## ***Meniscus, Tendons, Synovial fluid***

Meniscus is C-shaped rubbery, tough cartilage that acts as shock absorber attached at end of tibia bone. The meniscus improves the congruency between the tibia and femur bone. The meniscus is common to get damage and torn easily due to various factors[9][10]. A tendon is tough tensile band of fibrous connective tissue that connects bones to muscle. These tendons are similar to ligament but made of collagen attaching muscles to bones. Synovial fluid is like egg-white like consistency to reduce friction between cartilage during movement. The synovial fluid enters joint space that lubricates the joints producing albumin and hyaluronic acid.

### **1.1.2 Tissues Affected and Detection of Rheumatoid Arthritis**

Rheumatoid arthritis is the pervasive sort of chronic arthritis, that gradually increases to severity at older age[11]. It can be observed with various symptoms including increase in pain, inflammation, stiffness, decrease in mobility, difficulties in sitting and standing, and creaking sounds during knee movement[12]. Rheumatoid arthritis has the damage of cartilage, reduction in joint space, bone erosion, that leads to friction of bones as shown in figure 1.3.

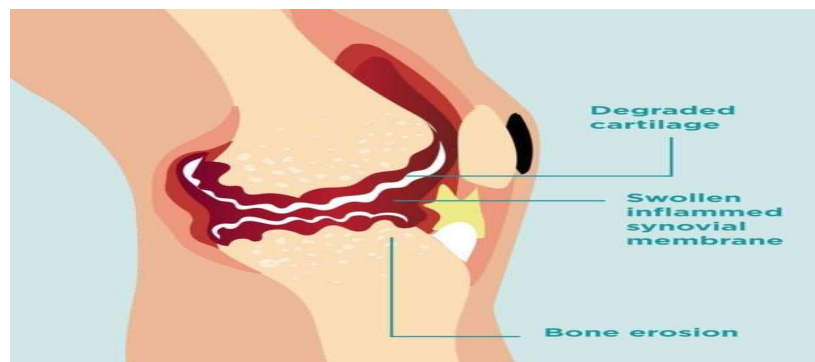


Figure 1.3 Knee joint affected by RA (Source: Creakyjoints)

The loss of cartilage can also be observed on patella, but early degradation starts between femur and tibia[13]. The bone erosion can be observed on early on femur and tibia tissues. Followed by these, the ligaments and tendons are stretched resulting in abnormal functioning of knee. As the cartilage has no nerves, so the degraded cartilage is not the only cause of pain in knee. The bone erosion, friction amongst knee bones causes pain and inflammation. Thus, early diagnosis of RA in early stage, will be better for patients as per the rheumatologist. The only way to identify and monitor the progression is non-invasive modality like MR image. The severity of knee RA linked with tissues can be tracked in several stages using KL grading. Various studies are presented and are inconclusive in identifying the exact changes. Thus, this research investigates various associated features of RA through changes observed and quantifies the proposed techniques on dataset using MR images.

### **1.1.3 Magnetic Resonance Imaging (MRI)**

The critical features are visible in medical modalities like X-ray[14], Computerized Tomography scan (CT)[15], ultrasound[16], and magnetic resonance imaging (MRI)[17][18]. Table 1 demonstrates the advantages and limitations of these modalities. Out of these modalities magnetic resonance (MR) images provides in-detail information regarding tissues and its structure. Although, X-ray, CT-Scan, Ultrasound can be used to detect several features as shown in table 1.1. Unfortunately, there are several limits involved to such procedures as exposure to radiation, intrusive experiments, low resolution of images. Non-invasive assessment for detection of RA features (volume, thickness, erosion, joint space narrowing) can accurately and consistently be performed using magnetic resonance imaging has not been studied for early detection of RA. Magnetic resonance images purvey structural and functional analysis of tissues in knee joint at various stages of RA development. MR images can be utilized to determine variations in joint space narrowing, cartilage volume, tissue erosion, etc. MR images are beneficial to analyze early RA provided well exactitude due to excellent structure presented in images[19].

Table. 1.1 Difference among medical modalities

<i>Modality</i>	<i>Pros</i>	<i>Cons</i>	<i>RA feature</i>
<i>X-ray</i>	Dislocation and fracture of bones can be detected.	Fails to detect muscle damage, soft tissues, organs. Body exposed to radiations.	Joint space width
<i>Ultrasound</i>	Nerves, fascial planes can be identified.	Artifacts are common occurred. Bone blocks the ultrasound waves.	Inflammation, cartilage thickness, roughness, stiffness, water content, collagen content.
<i>CT-scan</i>	Detect severe injuries and blood vessels.	Cannot detect the locations of diseases. More expensive than x-ray.	Joint space width, cartilage surface, volume, roughness.
<i>MRI</i>	No radiation like X-ray. Detects soft tissues, ligaments, tendons, joints.	Expensive compared to other modalities. More acquisition time is required.	Joint space width, Osteophytes, cartilage thickness, roughness, surface area, collagen content, water content, erosion.

MRI is based on atomic nuclei's magnetizing capabilities. The protons that are usually randomly orientated inside the water nuclei of the tissue being studied are aligned using a strong, uniform outside magnetic field. The alignment (or magnetization), by introducing an external Radio Frequency (RF) energy, is next disturbed or disrupted. The nuclei are re-aligned by different relaxation processes and produce RF radiation. The emitted signals are measured after certain period after initial RF. The frequency information in the signal from each position in the image plane will be converted into matching intensity levels by Fourier processing. These are then presented as grey

tones in a matrix arrangement of pixels. Different image kinds are formed by variation in RF pulse sequence used. This research uses different commonly used MR images such as T1-weighted, T2-weighted, and FLAIR images associated with RA.

### ***Types of MR images***

T1-weighted image is basic pulse sequences in MR image produced by short Repetition time (TR) and Time to echo (TE). T1 characteristics of tissue determine predominantly the contrast and brightness of the image. In T1-weighted images the compartments with high fat content appear bright and compartments filled with water appears dark. If the knee images weighted by T1 had no short periods (TRs), all the protons would regenerate their alignment with the main magnet field and the image would be evenly intensive. Choosing a TR short of the recovery time of tissues helps you to distinguish between them, such as tissue contrast. The sequences of T1-weighted images present the best contrast for paramagnetic disparity agents such as blood vessels around brain, spinal cord, substances passing through central blood system. T1-weighted shows the lesions and damages with black holes.

T2-weighted image [19] is common sequences in MR images produced using longer TE and TR times. T2 characteristics of tissue determine predominantly the contrast and brightness of the image. In knee images with T2-weight compartments filled with water appear bright and dark appearance with fat content tissues. The T2-weighted images are used to detect vascular lesions and tissues. It is necessary to remove the abnormalities to produce appropriate peak signal to noise ratio (PSNR) and structural similarity index (SSIM). Dual Echo Steady State (DESS) is a constant state sequence of GRE. First, the TR is short compared to T2-weighted next to radio frequency (RF) is applied. Second, the RF pulses are evenly scattered with same flip angle with constant TR. Based on the concept explained in [20], the instantaneous acquisition of two independent steady state free precision (SSFP) echo allows two diverse contrast formation for MR images.  $S + =$  (FISP) fast imaging steady state precision, and  $S - =$  PSIF (Reverse of FISP). The PSIF leads to high contrast T2 images, whereas FISP leads to contrast dominated T1/T2 ratio images. The DESS images has potential to extract the morphological and functional analysis with high resolution.

The Flair sequence[21] is comparable to T2 images with the exception of that the TR and TE times are very prolonged. So that, bright region deformities remain in the image and fluid attenuated make it dark. Flair images are free of water is now dark and tissues remain dark. Table 1.2 discusses the different types of commonly used MR images with TE and TR times. As shown in the figure 1.4 the three different MR images are illustrated. Figure 1.5 shows the sagittal view, coronal view, and axial view of the same MR image. It can be observed that the tissues are clearly visible in all the plane views of knee structure.

Table. 1.2 TR and TE time for MR image sequences.

<i>Type of MR Image</i>	<i>TR (msec)</i>	<i>TE(msec)</i>
<i>T1-weighted</i>	550	13
<i>T2-weighted</i>	4700	91
<i>Flair</i>	9800	114

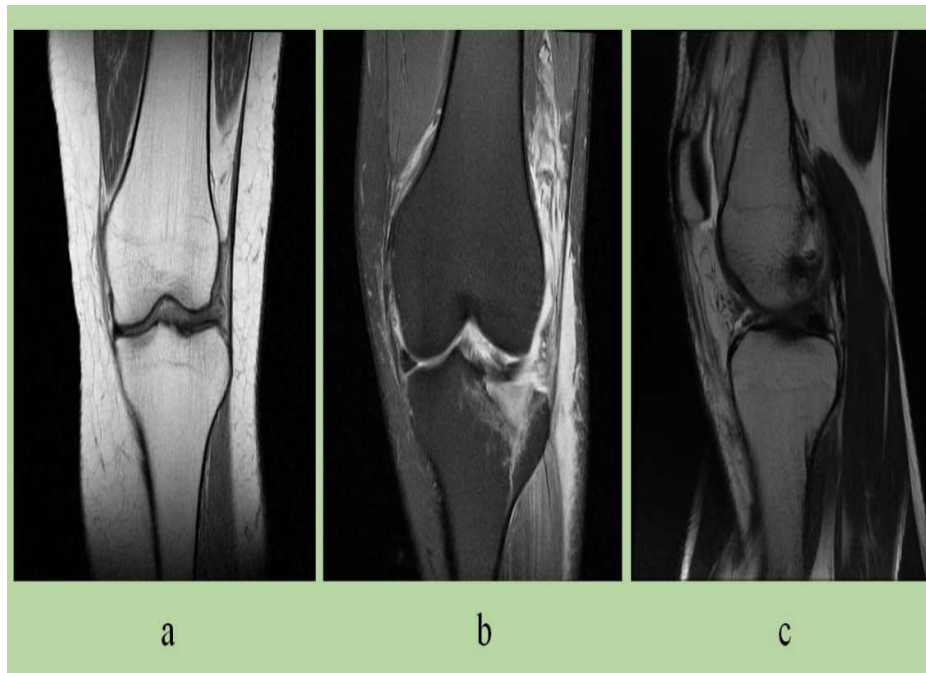


Fig. 1.4 Knee MR image types (a) T1-weighted (b) T2-weighted (c) Flair



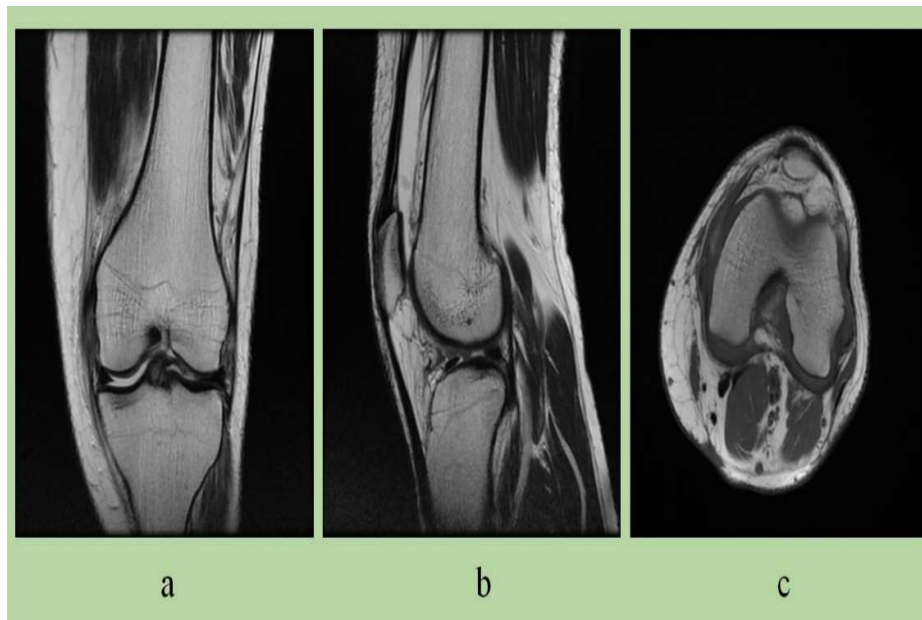


Fig. 1.5 Knee MR image views (a) Coronal view (b) Sagittal view (c) Axial view

## 1.2 Significance of Intelligent Medical Diagnostic System

Intelligent medical diagnostic system (IMDS) is a term that refers to techniques which can be applied to almost any complex medical problem [22]. IMDS enable computer systems to think and interpret, to collect and integrate domain information, to learn from acquired information, to apply information and experience for manipulating the environment, to conclude condition with hairiness and vagueness, to identify and infer in rational ways, to retort quickly and efficiently to new circumstances, to differentiate the relative importance of dissimilar elements in a state, to alter their conduct and respond to changes in the outer environment and to make sense out of imprecise or incongruous information. IMDS generate solutions to complex medical problems; by capturing information, identifying hidden patterns in multi-dimensional data, that is too hard for humans to understand. IMDS provides solutions in domains like, image processing, expert systems, computer vision, etc. The major applications are medical application, manufacturing and business, web-based services. IMDS may adopt different styles in order to get efficient and precise results. The styles include supervised learning, unsupervised learning, reinforcement learning [23][24][25].

The supervised learning has labelled input data and a target variable in which the training process continues until the model achieves maximum possible accuracy. A few techniques for supervised learning are support vector machine (SVM), Decision trees (DT), K-nearest neighbor algorithm (KNN), etc. The second learning i.e., unsupervised learning has unlabeled data and do not have target variable to predict the model. A few techniques for unsupervised learning are neural network (NN), Apriori algorithm, principal component analysis (PCA)[26], independent component analysis (ICA), etc. Third learning is reinforcement learning where the input data consists of labelled and unlabeled instances, and system trains itself using trial and error to make decisions. A few techniques are temporal difference learning (TDL), Q-learning, state-action-reward-state-action (SARSA), etc. Knowledgebase (KB) or expert systems like fuzzy are specially defined to represent a set of rules for a specific task. These expert systems have potential dealing with uncertainty and imprecision. These expert systems [27] are capable of representing data in situations of inconsistency and imperfect data.

Intelligent medical diagnostic systems (IMDS) are categorized into several groups that include clustering techniques, regression techniques, association rule-based techniques, artificial neural network techniques (ANN), instance-based techniques, ensemble techniques, clustering techniques, and deep learning (DL) techniques[28]. Clustering techniques arranges the instances into groups using hierarchal approaches. Regression approaches measure the error for refinement in predictions. In broad, multidimensional datasets, association-based rule learning approaches are in the form of rules in connection to characteristics. Artificial neural networks function through the selection of data, network creation and formation, the evaluation and validation of the objectives and performance using confusion matrices and medium square error. Instance-based techniques construct the training data model and then use similarity measurements between instances to predict fresh data. The ensemble is the combination of two or more self-trained procedures which integrate predictions to generate a final prediction. Deep learning[29] is a subset of machine learning that has networks capable of learning unlabeled data to build complex neural structures.

Computer aided diagnostic systems build using intelligent techniques provides efficient outcomes for all possible medical related problems[12]. These systems filter the information overflow, knowledge eventually to provide better outcome. Intra-observer and Inter-observer are subjected to individual preferences and observations. Intelligent system improves the human decisions and provide ability to systems to learn from some tasks and act suitably with environment for increasing success of model. It makes automated system to learn with more data and cross validate the model with different methods like holdout method, stratified cross validation, leave-p-out cross validation, k-fold cross validation to validate the performance of the approach. Performance is assessed employing various quantitative measurements like accuracy, precision, sensitivity, specificity, and many more. Selection of IMDS depends on volume, class, and structure of data. No intelligent system is dominant to all other on given problem. Sometimes a specific technique fits the problem, and best way is to try numerous techniques for finding the best fit.

### **1.3 Motivation**

Modern computing has extended its reach to the intense and efficient use of intelligent medical systems. Owing to the ambiguity and intricacy in medical data, obtaining vital information turn out to be a foremost challenge for physicians. This challenge can lead to inaccurate diagnosis of the illness, which would extend lead to inadequate medication. Therefore, it is beneficial for patients if the medical professionals cross check their assessment with the help of intelligent medical diagnostic systems (IMDS). IMDS are developed resourcefully for analyzing complex and ambiguous medical data. IMDS efficiently persuade over the inadequacies, help in obtaining better classification and system performance adaptable. IMDS decreases the probability of diagnostic errors, reducing the cost, time and efforts needed in clinical trials. Nowadays, the IMDS are developed by integrating two or more techniques for more proficient learning and task completion. However, the individual techniques also produce same result as integrated depending on nature of problem. Research in this field is increasing year by year with new thoughts and methodologies. Few widely used IMDS are fuzzy theory and systems, neural networks, machine learning based on popularity for knee RA classification.

Early detection of knee rheumatoid arthritis (RA) has been considered as an important problem among rheumatologists, and researchers, as it stops further degradation of tissue, reducing inflammation, swelling in joints, stiffness, and pain in knee. This can be achieved by assessing the changes in knee tissue structure at early progression of disease using non-invasive imaging modalities. As discussed, early features that changes rapidly are essential to analyze early RA. A broad literature assessment has shown that the whole transition from no RA to early RA characteristics has not been quantified successfully and that studies are undertaken to assess features in separate studies or multiple features utilizing various modalities. Now, the challenge is to detect early RA to severe RA by combining one or more features to enable improved sensitivity and specificity in progression of RA. In addition, various morphological features associated with RA can precisely, non-invasively quantified using MR images. Thus, this motivated us to design and develop an intelligent medical diagnostic system (IMDS) for assessing the progression RA.

#### **1.4 Problem Statement**

The main intention of this research study would be to develop an intelligent medical diagnostic system (IMDS) for assessment of knee RA using MR images based on KL grading. Formulating a novel preprocessing technique along with efficient segmentation and feature extraction approach based on morphological structure through MR images for assessment.

#### **1.5 Research Objectives**

The objectives of the research are following:

- 1) To remove the noise from Magnetic Resonance Images and to enhance its color.
- 2) To perform segmentation and feature extraction on Magnetic Resonance Images.
- 3) To propose an intelligent medical diagnostic system for Rheumatoid Arthritis using machine learning.
- 4) To compare the performance of proposed system with existing systems.

## 1.6 Approach of the Study

This work provides a survey on intelligent strategies used to treat arthritis, which will aid researchers in understanding the present state-of-the-art. The research describes the following forms of arthritis: rheumatoid arthritis, osteoarthritis, gout, juvenile idiopathic arthritis, psoriatic arthritis, and lupus. The study also discusses pros and cons of different diagnostic systems developed for arthritis. Further, several imaging modalities are reviewed, revealing that MR images has capability to measure early RA progression. The classification of knee RA is achieved in multiple stages that are broadly stated as follows:

1. Preprocessing
2. Segmentation and feature extraction
3. Classification using KL grading

Preprocessing involves denoising and contrast enhancement of MR images that is prior necessary to obtain accurate segmentation. MR images are affected by different types of noise that makes it difficult to feature the tissues. In this research study, a new methodology is proposed based on convolutional neural network (CNN) and dictionary learning that reduces noise from the MR image. This method also enhances the contrast of adjacent tissues by increasing pixel intensity. This approach is superior to many deep learning techniques used earlier in terms of peak to signal noise ratio (PSNR), structural similarity index (SSIM), mean square error (MSE). In this approach a dictionary is generated during training of the model to provide optimization of testing and reducing computational time.

The development of segmentation and feature extraction model plays a great role in assessment of evaluation of features. A novel discrete-MultiResUNet architecture is proposed that is a structure of discrete wavelet transform and MultiResUNet. The morphological measurements such as cartilage thickness, joint space narrowing, meniscus volume for femur and tibia compartments are measurement for approach. Combining multiple features will increase the accuracy, sensitivity, specificity of intelligent system. However, after segmentation the images are classified using

ResNet50 and KL grading is applied ranging from 0 to 4 (no arthritis to severe arthritis) respectively.

The thesis contributes to the development of methodologies for quantification of framework needed for identifying early RA progression. In summary, the proposed model will be useful in assisting rheumatologist, in analyzing patients.

### 1.6.1 MR Image Dataset

In this research, two datasets are used, one is local collected dataset, second is collected from Osteoarthritis Initiative (OAI) database which is publicly available was used for test and validation of developed methodology. MR image dataset of knee consists of T1-weighted, T2-weighted and Flair images with different views (sagittal, coronal, and axial). The parameters of MR image dataset are described in table 1.2.

Table 1.2 MR Image Dataset Specification

<i>Sr. No</i>	<i>Parameter</i>	<i>Specifications</i>	
		<b>Local dataset</b>	<b>OAI dataset</b>
1	Repetition time (TR)	2280msec	16.3msec
2	Echo time (TE)	38.1msec	4.7msec
3	Field of view (FOV)	140 X 140 mm <sup>2</sup>	140 X 140 mm <sup>2</sup>
4	Flip angle (FA)	25 Degree	25 Degree
5	Slice thickness (ST)	0.7mm	0.7mm
6	Matrix size (MS)	512 X 512	512 X 512
7	Bandwidth (BW)	250Hz/pixel	185Hz/pixel
8	No of slices	220	160

### 1.6.2 Architecture Assessment Parameters

The implementation of developed architecture is scrutinized and assessed at early phase. This evaluation assessment is presented in terms of qualitative and quantitative ways. Qualitative factors include visual insight and assessment of results achieved,

however quantitative factors include numerous factors that are conversed in-detail in the following sub-segments.

### ***Denoising and Contrast Enhancement***

The quantitative parameters for denoising and contrast enhancement technique proposed is measured in terms of following parameters: peak signal to noise ratio (PSNR), that evaluates the amount of noise present in medical image in terms of decibels (dB), structural similarity index (SSIM), that evaluates the similarity between denoised image and original image, mean squared error (MSE), that evaluates difference between actual value and obtained value, enhancement measure (EM), that evaluates degree of contrast enhancement.

#### *A. Peak signal to noise ratio (PSNR)*

PSNR is the proportion amongst determined possible power of an image and power of distorting disturbance that influences the characteristic of its interpretation. It is necessary to estimate to compare the maximum clean image with possible power. PSNR can be estimated as shown in equation 1.1.

$$PSNR = 10 \log_{10} \frac{(I-1)^2}{MSE} \quad (1.1)$$

where, I, is the maximum possible intensity in an image.

#### *B. Structural Similarity Index (SSIM)*

SSIM shows the resemblance of two medical images considering image degradation as ostensible transformation in structural data, including contrast masking. SSIM can be estimated as shown in equation 1.2.

$$SSIM(x, y) = \frac{(2\mu_x\mu_y + C_1)(2\sigma_{x,y} + C_2)}{(\mu_x^2 + \mu_y^2 + C_1)(\sigma_x^2 + \sigma_y^2 + C_2)} \quad (1.2)$$

where,  $\mu$ , denotes average value of given image,  $\sigma$ , denotes standard deviation as shown in equation 3.

$$\sigma_{x,y} = \frac{1}{N-1} \sum_{i=1}^N (x_i - \mu_x)(y_i - \mu_y) \quad (1.3)$$

where, x and y are the images compared.

### C. Mean Squared Error (MSE)

MSE is a metric that calculates the difference between the value and the value in effect. MSE is a risk estimator subsequent to the expected value of the squared loss. MSE can be estimated as represented in the equation 1.4.

$$MSE = \frac{1}{PQ} \sum_{i=0}^{P-1} \sum_{j=0}^{Q-1} (X(i, j) - Y(i, j))^2 \quad (1.4)$$

where, X signifies the matrix data of original image. Y denotes the matrix of distorted image. P denotes the number of rows, Q denotes number of columns in pixels, i and j respectively signifies the index value of row and column.

### D. Enhancement Measure (EM)

EM is a measure of contrast enhancement, estimating for both medical images: actual and enhanced medical image. The disparity (contrast) of the medical image is enhanced measured on EM value of enhanced image is larger than that of actual image. EM can be estimated as shown in equation 1.5, where  $b_1$ ,  $b_2$ , are non-corresponding units of size 3 X 3 and  $I_{max}$ ,  $I_{min}$ , are intensity values.

$$EM = \frac{1}{b_1 b_2} \sum_{j=1}^{b_2} \sum_{i=1}^{b_1} 20 \log \frac{I_{max}}{I_{min}} \quad (1.5)$$

### **Segmentation and Feature Extraction**

The proposed segmentation with feature extraction model is measured in terms of dice similarity coefficient (DSC), volumetric difference (VD), volume overlap error (VOE), root mean square surface distance (RMSD), average surface distance (ASD), and meniscus thickness (V), length and width. The efficiency measures are compared by an expert with more than 25 years of expertise with the results produced from the suggested models to the ground reality. Ground truth prepares the manual outline of overall features by an expert rheumatologist. DSC is presented in terms of true-positive, true-negative, false-positive, false-negative in the region of interest. These computations are corresponding the ground reality as shown in figure 1.6. True-positive (TP) is the section labelled as foreground section, true-negative (TN) is the section correctly labelled as background section, false-positive (FP) is the



section incorrectly labelled as foreground section and false-negative (FN) is the section incorrectly labelled as background section.

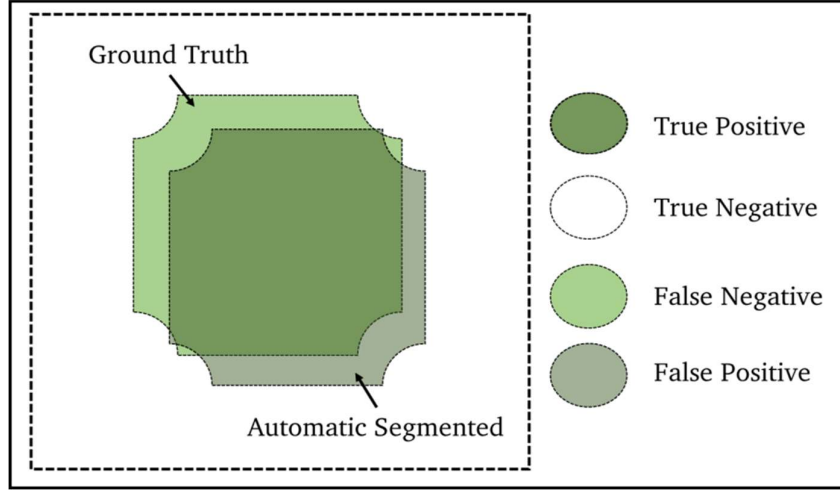


Fig. 1.6 Representation of TP, TN, FP, and FN

#### A. Dice Similarity Coefficient (DSC)

DSC is used to measure the similarity between two images. It evaluates the spatial overlap amongst two segmentations regions validating the segmentation. DSC can be estimated using equation 1.6

$$DSC = \frac{2 \times (P \cap Q)}{(|P| + |Q|)} \quad (1.6)$$

#### B. Mean surface distance and Root mean square surface distance (MSD and RMSD)

Mean or average surface distance (MSD) and root mean square surface distance (RMSD) are estimated on boundary coordinates of segmented tissues. For each individual boundary the closest coordinate is examined, and relative Euclidean distance is mentioned. The procedure is repetitively performed for all the boundaries of the tissues. The RMSD is estimated similarly but the distance is squared before storing. The equations 1.7 and 1.8 provides MSD and RMSD values, respectively.

$$MSD = \frac{1}{\theta^n P + \theta^n Q} \left[ \sum_{i=1}^{\theta^n S} (\min)_{\theta Q} \|P_i - Q\| + \sum_{j=1}^{\theta^n P} (\min)_{\theta P} \|Q - P\|_2 \right] \quad (1.7)$$

$$RMSD = \sqrt{\max_{\theta P} \min_{\theta Q} \|P - Q\|_2} \cdot \sqrt{\max_{\theta Q} \min_{\theta P} \|Q - P\|_2} \quad (1.8)$$

### C. Volume overlap error (VOE) and Volume difference (VD)

The volumetric intersection error concerning the conventional voxels of segmentation P and manual segmentation Q as reference is shown in equation 1.9. The volumetric difference between P and Q is defined in equation 1.10

$$VOE = 100 \left( 1 - \frac{|P \cap Q|}{|P \cup Q|} \right) \quad (1.9)$$

$$VD = 100 \left( \frac{|P| - |Q|}{|Q|} \right) \quad (1.10)$$

### Classification and Grading

The proposed classification model for knee RA progression is assessed in factors of sensitivity, specificity, precision, f1-score, accuracy and mean absolute error. The result also defines joint space narrowing and KL grading for classifying the MR images accordingly.

#### A. Accuracy

Accuracy determines whether the technique is best at distinguishing associations and relationships amongst variables in a dataset built on training data or dataset.

$$Accuracy = \frac{True\ positive + True\ negative}{True\ positive + True\ negative + False\ positive + False\ negative} \quad (1.11)$$

#### B. Precision

Precision is the fraction of relevant instances among the retrieved instances. It also provides ratio of true-positive to total of true-positives and false-positives.

$$Precision = \frac{True\ positive}{True\ positive + False\ positive} \quad (1.12)$$

#### C. Sensitivity or Recall

Sensitivity is also known as recall or hit rate, that provides how well a model can identify true-positive values. It is also a measure of actual true-positive that are predicted as positive.

$$\textit{Sensitivity or Recall} = \frac{\textit{True positive}}{\textit{True positive} + \textit{False negative}} \quad (1.13)$$

#### D. Specificity

Specificity is the estimate representing the portion of true-negative that are precisely known.

$$\textit{Specificity} = \frac{\textit{True negative}}{\textit{True negative} + \textit{False positive}} \quad (1.14)$$

#### E. F1-Score

F1-score measures the perfect precision and recall values. It is a measure to evaluate binary classification of model's accuracy on a dataset.

$$\textit{F1 - Score} = 2 \times \frac{\textit{Precision} \times \textit{Recall}}{\textit{Precision} + \textit{Recall}} \quad (1.15)$$

#### F. Mean Absolute Error (MAE)

MAE is the enormity of disparity amongst the predicted value of an evaluation and actual value of evaluation. The absolute error provides ground truth difference with predicted value.

$$\textit{MAE} = \frac{1}{N} \sum_{j=1}^N |Y_j - \hat{Y}_j| \quad (1.16)$$

## 1.7 Outline of the thesis

This thesis is structured into six chapters, including first chapter describing medical background of arthritis disease, significance of intelligent system, motivation behind this research work, objectives of the study, and providing brief description of each chapter.

Chapter 2 presents a comprehensive literature review on intelligent medical diagnostic system (IMDS) applied to arthritis disease. Intelligent systems are divided into three categories based on objectives. Preprocessing approaches, segmentation and feature extraction approaches, and prediction or diagnostic approaches. This chapter identifies the individual and integrated techniques applicable for arthritis disease.

Performance comparison along with advantages and disadvantages of applied intelligent medical diagnostic system (IMDS) are also presented.

Chapter 3 describes the proposed scheme titled “SANR\_CNN for preprocessing of MR images”. Preprocessing involves the denoising and contrast enhancement of knee MR images. Denoising and contrast enhancement are performed using proposed SANR\_CNN technique. Efficiency of proposed denoising model is assessed with several parameters such as PSNR, SSIM, EM, and MSE.

Chapter 4 discusses the proposed scheme titled “Discrete-MultiResUNet architecture for segmentation and feature extraction”. The region/ area of interest (R/AOI) is estimated by selecting tissue boundaries. Boundary displacement and extracting tissue interface is performed with masking and thresholding. Performance of the proposed model is measured using quantitative parameters such as dice similarity coefficient (DSC), voxel difference (VD), etc.

Chapter 5 presents the proposed scheme titled “ResNet50 architecture for classifying the knee MR images with KL grading”. The preprocessed and segmented MR images are assessed for joint space narrowing (JSN) estimating KL grading. Performance is measured using sensitivity, specificity, accuracy, and confusion matrix.

Chapter 6 draws the conclusion of the thesis with limitations of work. It also presents the future scope of work. The list of publications related to the research work is mentioned at the end of thesis.

## Chapter 2

### Literature Review

This chapter provides an in-detail review of existing systems with their advantages, limitations and applications involved. The chapter is structured in following order: Section 2.1 introduces the need of literature and significance of intelligent medical diagnostic system (IMDS) in RA diagnosis. Section 2.2 presents the challenges in assessing the RA disease using MR images. Section 2.3 incorporates discussion on machine learning approaches followed by discussion on segmentation and feature extraction with manual and automatic approaches in Section 2.4. Section 2.5 presents diagnostic approaches with KL grading. Section 2.6 provides observations and finally concluded in Section 2.7.

#### 2.1 Introduction

The nomenclature of rheumatoid arthritis was framed in 1941 by American Rheumatism Association (ARA), described as “a chronic inflammatory disease of connective tissues with constitutional symptoms of varying degree leading to joint deformities”[30]. However, the symptoms change inevitably due to various factors. So, the new revised definition of rheumatoid arthritis (RA) provided by D. Aletaha[31], “Rheumatoid arthritis (RA) is a chronic inflammation, life altering joint disease that are characterized by tenderness, destruction of synovial joints leading severe disability, and mortality”. Later, S. Murakami[32] defined RA as “autoimmune disease often leads to substantial disability and morbidity due to bone erosion considered irreversible”. The key components of RA are cartilage thickness, bone erosion, meniscus volume, synovial fluid volume, and wear and tear of ligaments. Despite these discrepancies, in definitions, RA comprise of bone erosion, cartilage thickness, and volume of synovial fluid.

Thus, for exactness the definition of RA can be considered with four features to the joint space width/ narrowing between femur and tibia tissue[33], meniscus volume[34], accumulation of synovial fluid[35], and cartilage thickness[36]. The fact the changes in these features at initial stage has been taken into consideration to

define early RA. An example of normal knee and diseased knee structure is illustrated in figure 2.1. Early progression is observed in figure 2.1(b), where the changes are physically visible. In the research, it can be observed that the MR image is most promising modality approach to early assessment of RA. MR image has better soft-tissue contrast, spatial resolution capability, multi planner view, and quantitative assessment abilities. MR images facilitates in accurate joint space narrowing, meniscus volume, cartilage thickness measurements compared to images produced by different imaging modality. Information about knee composition may also be used to accurately evaluate biochemical substance[37][38] assessment using quantitative MR measuring. Thus, in this research, MR images are considered as suitable modality to measure various RA features associated with early assessment.

## RHEUMATOID ARTHRITIS

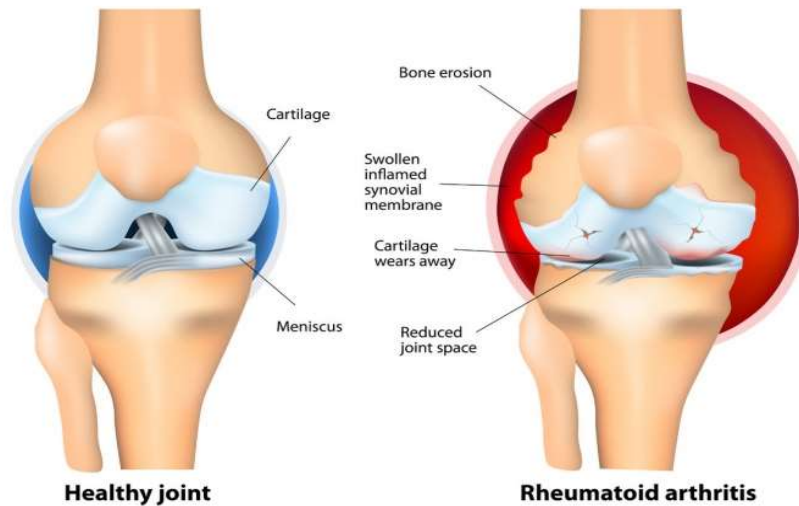


Figure 2.1 (a) Healthy knee joint (b) Rheumatoid arthritis knee joint

Intelligent medical diagnostic system (IMDS) has played a vital role in knee arthritis diagnosis. From statistical techniques to neural networks, all these have extensively deployed on evaluating the clinical trials for arthritis. Due to escalating ambiguity and intricacies in datasets, extracting the valuable information becomes a major challenge for clinical trials. Further, this challenge leads to inaccurate assessment of the disease. So, to avoid uncertainties in treatment to patients, medical experts prefer intelligent

systems interpreting the patient's data. IMDS are widely applied to diagnose and classify RA progression. These IMDS decrease the probability of occurrences of medical error, reduces the cost, time and efforts needed for diagnosis. The IMDS gathers the useful information extracting from medical images with different modalities for the treatment of RA. However, Magnetic resonance imaging (MRI) allow detailed analysis from several modalities. But these MR medical images cannot directly quantify the progression of RA due to certain challenges that are associated with acquisition of MR data that are discussed in sub-section 2.2.

## **2.2 Challenges in Assessment from MR image**

In prior years, studies have shown various endeavors from MR images for quantifying the progression of rheumatoid arthritis. Normally, every recent technique was assessed with distinct constraints used on various test medical images. However, the approaches perform well for particular datasets, but don't give a general measuring solution globally. The main reason for this is the various features of knee joint RA and MR image capture which lead to challenges in analyzing MR knee pictures.

### **2.2.1 Image Artifacts**

MR medical images are usually susceptible to several artefact kinds. These artefacts are evident in the form of chemical changes, pulsation, magic angle, volume effects, tendency which can lead to misdiagnosis in MR images [39][40]. The appearance of brilliant dark frames on the opposite margins of the same tissue results from the chemical artefacts shift. Due to differences in water and fat environments and the chemical shift influence on signal proton encoders of fat and water this distortion occurs[41]. In MR images the computational approach may wrongly interpret signal intensities for region of interest with inclusion and exclusion criteria as shown in figure 2.2(b)[42].

A propensity artifact is caused due to inhomogeneity in magnetic field that outcomes in abnormal sensitive tissue boundaries. It can be observed that metallic foreign bodies, hemosiderin from bleeding are various factors for propensity. This type of tendency might result in tissue areas being misinterpreted by techniques as shown in figure 2.2(a). The partial volume effect causes the shrunk feature of edges in the

region of sagittal plane of MR images. It is highly difficult for an expert to perform segmentation in these regions. Due to different signal intensities caused by variations in pulse sequencing that may lead difficulty in development of computational techniques as illustrated in figure 2.3. Prior to the development of technique for early diagnosis of RA, these artifacts should be considered.

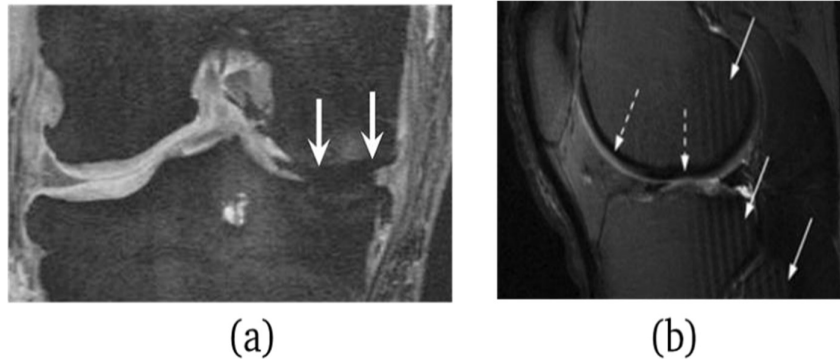


Figure 2.2 Artifacts Induced in MR Images (a) Propensity artifact (b) Substance shift (dotted arrows) and pulse artifacts (solid arrows)

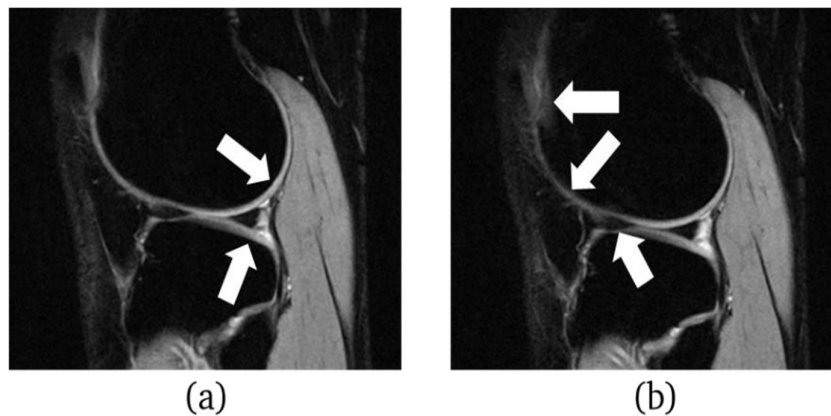


Figure 2.3 Volume effect(a) sharp edges on cartilage region (b) distorted edges on cartilage region.

### 2.2.2 Image Properties

The soft tissues cartilage, meniscus, and synovial fluid have an inhomogeneous intensity, poor contrast and an uneven form of MR images [43]. Due to local differences, numerous problems have been identified in the tissue characteristics which play an essential role in the development of techniques. These problems are found as low point visibility on image sequence datasets, low or high intensities on



soft tissue regions associated to neighboring tissue region[44]. The variable portions of MR images with different intensity variation [45] can be found in figure 2.4.

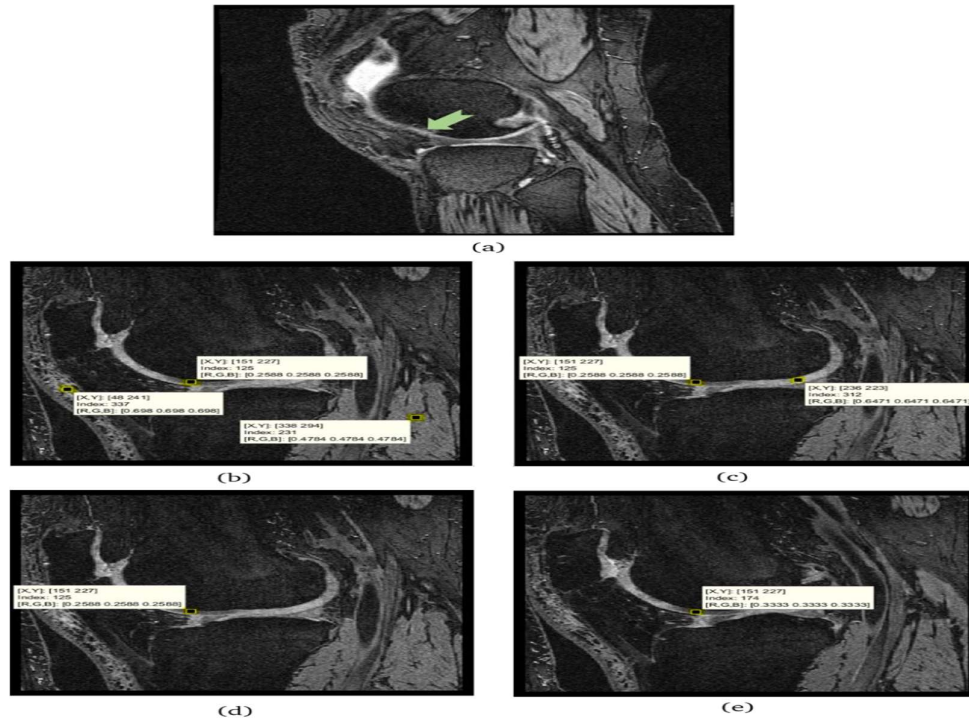


Figure 2.4 (a) Low point visibility contrast (arrow denotes cartilage tissue). (b) low intensity in different tissues (c) variable intensities in cartilage region, (d) and (e) different slices of variable intensity

### 2.2.3 Tissue Structure

The cartilage, and meniscus tissue is about 2mm to 4mm thick, meniscus width of 9 to 10mm, and synovial fluid of 1mm to 6mm thick, in every individual healthy human. These tissue thickness reduces at the rate of 2.43% [46] annually up to 60% [47] with progressive knee RA. These tissues turn into irregular shape and structure in severe RA stage. Figure 2.5(a) illustrates the abnormal structure of knee obtained in sagittal view. The boundaries between femur and tibia still present complexities as illustrated in figure 2.5(b). Consequently, manual and semi-automated segmentation techniques are utilized to deliver consistent assessment.

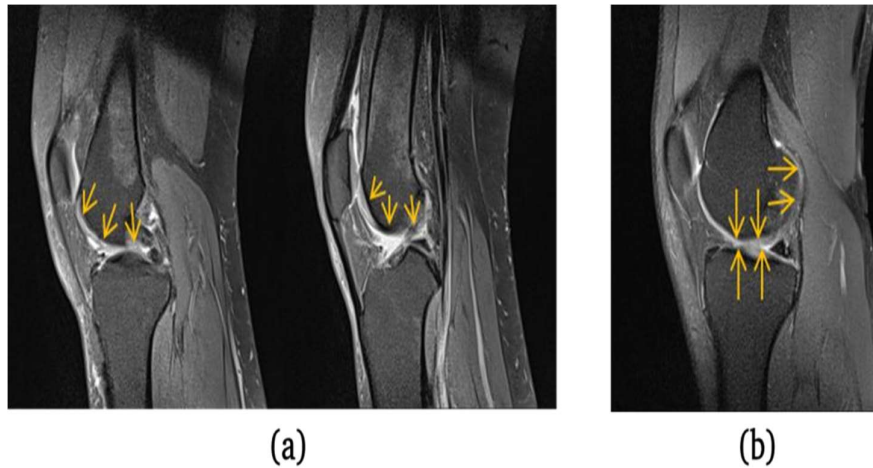


Figure 2.5 (a) Irregular shape of knee structure (b) diffused boundaries between femur and tibia tissues.

#### 2.2.4 MR Pulse Sequence

In developing diagnosis technique, a selection of optimal MR pulse sequence for acquisition of MR knee joint images is vital. Research reveals that the MR pulse sequences that produce a high signal-to-noise ratio in soft tissue regions, a high noise contrast, and a high spatial resolution should be used for soft tissue imaging in a marginal scanning time with its capacity to decrease the artifact[48]. Several MR pulses are typically applied to the knee RA for evaluation purposes, e.g., T1 weighted, T2 weighted, Flair, density of the protons (PD), 3D spoil echo (SPGR), double echo stability (DESS).

In previous studies, most of the researchers have used MR pulse sequences as standard practice and tested the applicability on single sequence images[49][43]. The conventional techniques use some complex information like pixels, edges, voxels, and knee MR scans. Profoundly, the techniques related to diagnosis utilize intensity/ pixel information as area of importance. However, the pulse sequence modification leads to intensity fluctuation and image contrast variations as shown in figure 2.6. This pulse sequence dependency fails many techniques due to pixel or intensity issues. Thus, it is challenging to diagnose the disease using pixel/intensity using different pulse sequences.

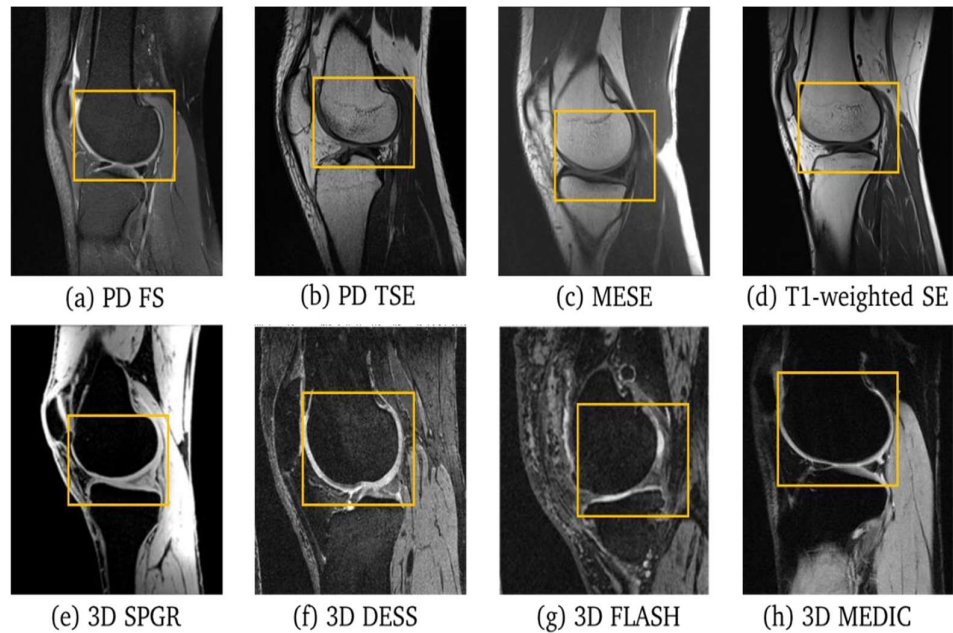


Figure 2.6 MR pulse sequences (a) PD fat suppression (b) PD turbine spin echo (c) multi echo spin echo (d) T1-weighted spin echo (e) 3D spoiled gradient echo (f) 3Ddual echo steady state (g) 3Ddissolute low angle shot (h) 3D multi echo data imaging combination

### 2.2.5Magnetic Field Strength (MFS)

The magnetic field strength (MFS) is proportional to nuclear magnetic resonance (NMR) that measures linearity with polarized magnetic field. This statement defines that 3T MRI system yields double NMR as compared to 1.5T MRI system[50], resulting in peak to signal noise ratio (PSNR) to be doubled in acquired 3T MRI systems. As there is a compromise amongst scan time (ST) and PSNR. At 1.5T, identical PSNR can be achieved by improving the ST. However, increasing scan time certainly leads to increased artifacts in MR images. Thus, 3T MRI systems can be utilized with decreasing scan time to provide better quality images. Studies have shown no or little difference between 3T and 1.5T MRI Systems while assessing the RA diagnosis. However, at minimum magnetic strength (0.18t - 0.20T), contrast to noise properties and surrounding tissues make it difficult to diagnose with low PSNR. An increasing magnetic intensity leads to higher PSNR and high resolution of images but limitations owing to chemical changes, strength deposition and inhomogeneity.

For the diagnose of RA, MR images acquired from 3T and more ( $>7T$ ), gain in PSNR are expected to improve the image quality. These different magnetic fields provide inhomogeneity leads to flip angle in T1-weighted images with varied contrast. In addition, in the case with T2-weighted images, the scan time interrupts artefacts which make interpreting the area of interest and other tissues challenging. These artefacts and other potential problems make it hard to create diagnostic procedures[39].

## **2.3 Introduction to Machine Learning**

### **2.3.1 Machine Learning Paradigms**

Many different definitions have been framed, over the years, for the term machine learning (ML). A. Samuel [51] has defined ML as “Machine learning (ML) is the subfield of Computer Science (CS) that gives computers the ability to learn without being explicitly programmed”. It means the ML tasks are automatically performed without direct human interaction. Often, ML algorithms are data-driven effectively finding solutions to the problems with ability to generalize the data. ML methods usually characterize samples from the training dataset using function vectors to infer interpretations from their background data. A vector represents each sample in the exercise data set, which appropriately reflects the data extraction. The solution acquired from the data during training is a powerful tool to anticipate, analyze and interpret unseen information. It is vital thus that the solution be generalizable and that correct results can be achieved.

A traditional categorization of machine learning paradigms are:

**Supervised learning:** It is a learning process where the system learns based on labels assigned to the data. The performance of the system improves continuously in its learning process.

**Unsupervised learning:** It is a learning process in absence of labelling the data. The machine needs to infer the hidden patterns of the data without any potential solution.

**Semi-supervised learning:** It is learning process between supervised and unsupervised process where some inputs are labelled, and some are not.

Reinforcement learning: It is a learning process to make sequence of decisions to achieve uncertain goal in potential complex environment.

### 2.3.2 Supervised learning

In supervised learning system receives feedback from the information available in the data for the correct solution. More meaningful, in supervised learning the model tries to solve the problem of categorization.

#### *Classification*

Classification is the dilemma of distinguishing the type to which new interpretation belongs based on resemblance with previous data. The classification process[52] is illustrated in figure 2.7. The classification is split into two phases: model construction and model usage. In first phase the model is built to explain the concept. The second phase classifies the samples generating a system the instances. However, the future instances are not available, therefore it is necessary to simulate the model usage. The simulation is done by dividing the data into training case and testing case. The training is making the model to learn the data from training set, and testing is to identify the correct input data. The general approach for validating the classification model is shown in figure 2.8.

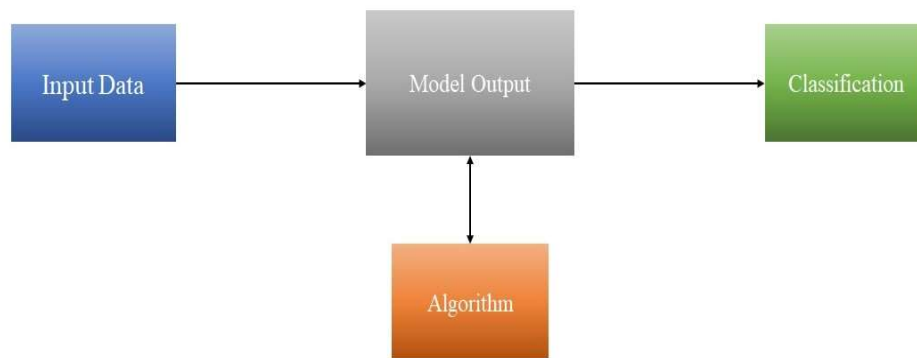


Figure 2.7 Classification process

The validation of model is evaluating how well the model performs with test instances. The performance of model is classified using confusion matrix parameters and Receiver Operating Characteristics (ROC) arc. The confusion matrix represented

in figure 2.9 usually represents positive and negative classes. A ROC curve is an illustration of how the model performs depending on true and false positive rates [53]. The true positive rate is same as sensitivity and represents the positive instances that are correctly classified. The false positive rate indicates negative samples that are incorrectly labelled as correct. The ROC score typically ranges between 0 and 1, often indicating the instance belonging to specific class.

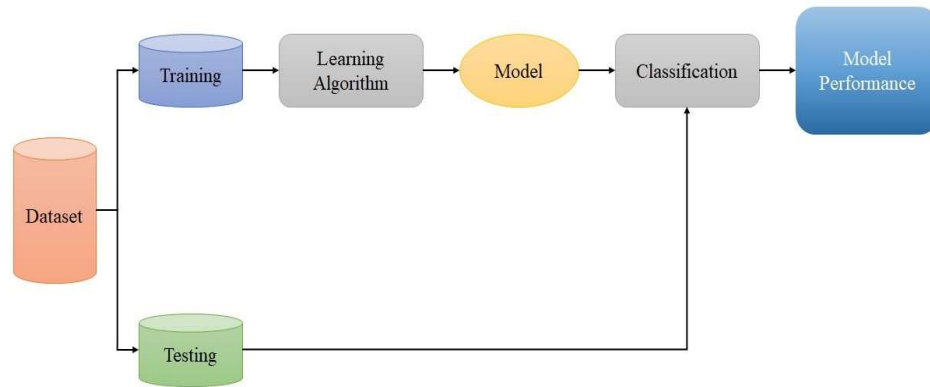


Figure 2.8 General classification model

		Actual Class	
		Positive	Negative
Predicted Class	Positive	True Positive	False Positive
	Negative	False Negative	True Negative

Figure 2.9 Confusion matrix

### 2.3.3 Unsupervised learning

Unsupervised learning is characterized as, making the model to learn without labelling. The system tries to identify patterns automatically within the data without any information about the solution.

#### *Clustering*

It is the task of grouping the same group participants as set of observation known as clusters. Clustering is an operation that can be performed on different algorithms with different measures to assess the similarity[54]. In clustering the k-means algorithm is

simplest and most used algorithm[55]. It works on process of centroids chosen for k parameters with desired clusters. Each datapoint is selected based on nearest centroid with different metrics used to determine the distance between clusters using Euclidean distance algorithm. The process is repeated until no change in cluster points, or centroid remains same as shown in figure 2.10.

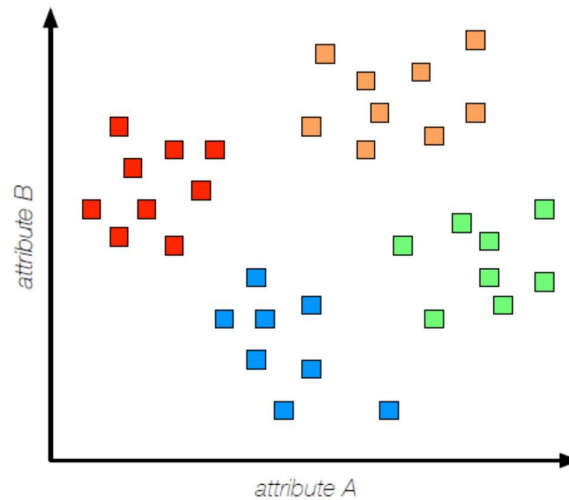


Figure 2.10 K means clustering

The principal component analysis (PCA)[56] is a process that aims to summarize the dataset into smaller set. The PCA preserves the size of original data regardless of transformation. The PCA provides weights needed to interpret a new variable using linear combination.

### 2.3.4 Reinforcement Learning

Reinforcement learning is a kind of machine learning approach in which the agent receives a reward in next time to assess previous action. It is capable of solving many complex problems with comprehensive setup of components that are an agent and an environment as shown in figure 2.11. An agent is apprentice and a decision maker, where the agent learns and determines the measures that must be implemented. The state is the phase, where the agent is present in the system. For every action by the agent, the system delivers reward, representing a mapping function from situations to actions.

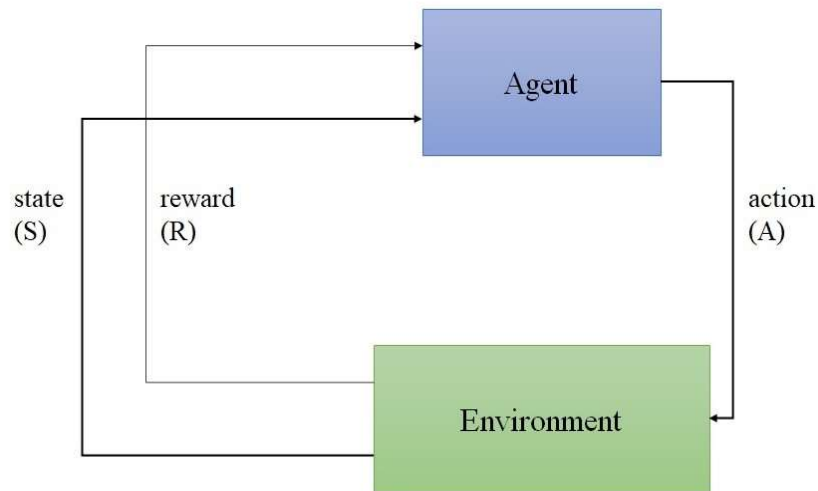


Figure 2.11. Reinforcement learning

## 2.4 Deep Learning

There are several machine learning approaches in the literature with one or more transformations[57]. These architectures have been effective and yield promising outcomes for simple and well-constrained problems. However, deep learning can be effective and economical for difficult and complicated real-world situations. Deep learning is an aspect of the learning of machines and consists of multi-layered sensing algorithms using non-linear processing units. There are several layers in deep learning that learn the high-level characteristics from low levels. Deep learning technique is divided into three phases: a deep network for unsupervised or generative knowledge, a strong network for supervised learning or discriminatory knowledge and a deep hybrid network.

Generative learning accepts high-level properties of the data and their associated attributes. Discriminative learning provides pattern classification characterizing the distribution of classes of the data. The hybrid learning is discrimination but generates the outcome of generative learning through better optimization. Deep neural network (DNN)[58], Recurrent Neural Network (RNN), Convolution Network[32], Deep Belief Networks, deeper stacking network (DBN), and advanced deep neural learning are among the most advanced techniques (DSN). Out of these networks, CNN is tremendously used in many of the real-world applications.



### 2.4.1 Convolutional Neural Networks

Convolutional neural networks (CNN) is a modification of multilayer perception, that is inspired by visible cortex and deep architecture. The feed-forward network generally comprises of multiple layers. CNN architecture is made up of some distinct layers that transforms the high volume of data through differential equations. Each layer consists of neurons with weights and distortions. Between input and exit layer one or more hidden layers are present. The entry layer (convolutional) learns the images and extracts features. The output is estimated by weighted average of all input neurons and passed through an activation function. The activation function such as Rectified linear unit (ReLU), and Sigmoid makes the layers into non-linear values. ReLU refers to non-linear function replacing all negative values by zeros. The ReLU activation layer will apply  $\max(o, x)$  function, thresholding at 0. Figure 2.12 illustrates the CNN architecture with different layers as described.

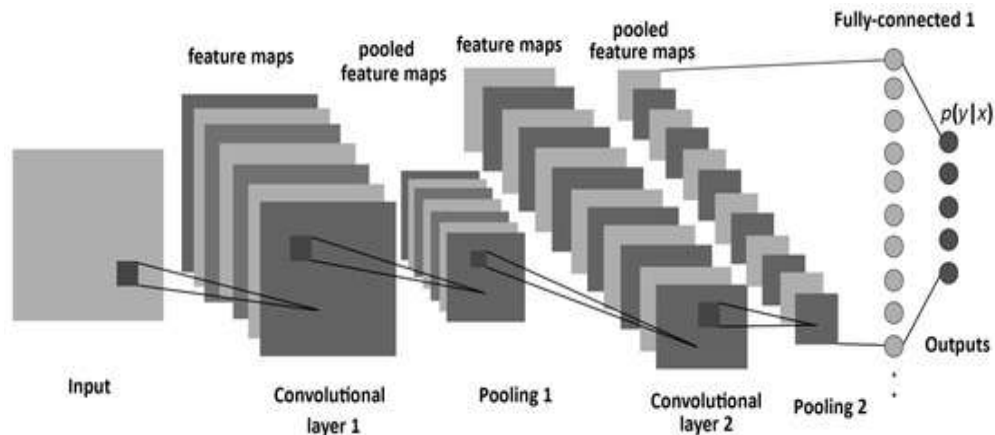


Figure 2.12. CNN architecture

The convolutions obtained will lose data over borders, so zeros are appended and recalculation of convolution with all input values are made known to be padding. These all values or information are captured from obtained image with kernels with striding are estimated with dot product between set of weights. The convolution has some weights, and these weights are shared by all inputs and weight sharing by each input connected by output neuron. In pooling layer, the combination of factors decreases the number and enhances network efficiency. There are three pooling methods for instancetotal, mean, and maximum pooling, among which max pooling is

best one and most used. Always the last layer of CNN will be fully connected layer producing output vector with linear combination. In the volume of characteristics that are supplied, every node in that layer is linked to every other node. The class opportunities are calculated with measurements such as  $[1 \times 1 \times X \times K]$ , where K is total quantity of classes.

### ***Convolutional Layer***

Convolutional layers are basic units of CNN. These layers are made of many filters, which are defined by width, height, and depth. Convolutional layers are reasonable solution for image categorization. Convolutional layers are comprised of subjective matrices called filters, generally known as kernels. These kernels slide move across the input image from top to right covering part of the image known as striding. The depth of the filter is equivalent to quantity of filters in convolutional layer. The output feature map can be estimated with the following function as represented in equation 2.1, where original input image is represented by  $f$ , and  $h$  denotes filter. The output matrix is represented with rows and columns as  $x, y$ .

$$G(x, y) = (f * h)[x, y] = \sum_i \sum_j h[i, j] f(x - i, y - j) \quad (2.1)$$

### ***Activation Layer***

After the convolutional layer, the input image is converted into a heap of feature maps. Every single feature map relates to visible feature at particular location within the image. This feature heap is equivalent to quantity of nodes (filters) in the convolutional layer. The activation function determines the relevance of model prediction. The activation function prevents the problem of vanishing gradient that changes the model prediction.

### ***Pooling Layer***

As the feature maps are stacked over the layers, the complexity increases. Each filter is assigned with task for identifying different features of the image that increases dimensionality, parameters of overfitting. So, pooling after convolutional layers performs down-sampling reducing the number of parameters for further layers. There are different types of pooling that can be performed in CNN. Basically, max pooling

takes two input arguments that are kernel height and width, and stride, then passes these values for corresponding node in the pooling layer. Global average pooling layer feature maps the dimensions reducing the feature stack into one-dimensional vector.

### ***Fully Connected Layer***

Fully connected layer makes the classification considering the input flattened vector of nodes. The vector will be passed through two or three dense layers and decisive initiation function earlier sent to the output layer. There are two common functions such as sigmoid and SoftMax functions for classification. Sigmoid generally uses binary classification problems and SoftMax uses the sum of values and utilized for both binary and multi-class categorization challenges. The decisive vector size will be equivalent to quantity of classes for prediction.

### **2.4.2 Feature Learning**

Feature learning implies to methods that transform unprocessed data into efficient and useful interpretation for additional processing such as segmentation, diagnosis, and categorization. Feature learning captures accurate features by using large number of networks. The deep learning network are multi-layered network that can be applied to understand feature representation in the hidden layer(s). In recent years, these feature learning methods are fine-grained for categorization because of rich representation of shape features. The feature learning can be classified as observed:

- (a) *Supervised feature learning*, is recognized to learn features from designated labelled data. CNN, DBN and multi-tasking are some approaches used to learn supervised functionality.
- (b) *Semi-supervised feature learning*, utilizes unlabeled information to assist supervised data. Some semi-checked functional learning approaches include label propagation, pre-trained data from DBN and a ladder network.
- (c) *Unsupervised feature learning*, is knowledge feature representation from data driven with no labels. The primary aim of this method is to identify and describe the details of unlabeled data. This method also helps to remove redundancies and preserve the essential feature information for classification.

Some of the techniques that adopt unsupervised feature learning are K-means clustering, Gaussian mixture model (GMM), principal component analysis (PCA), sparse coding, and autoencoders.

## 2.5 Noise Model

An image is nothing more than a two-dimensional array of numbers. Preprocessing is a process of preparing the raw data into data that is suitable for machine learning model. An image can be specified by numerical function  $f(x,y)$ , where  $x$  and  $y$  represents two coordinates horizontal and vertical respectively. MR images suffer from different artifacts that affects the accuracy of diagnosis. To solve this problem of artifacts image denoising should be prior step before segmentation the region of interest in the image. Image denoising is an unposed issue handled by the introduction of image priors[59]. Image patches consists of abundant information that provides sufficient priors for image denoising. The fault in acquisition process, transmission or compression may cause different noise.

The noise model can be represented with equation 2.2. The image  $I$ , represents clean or original image, and  $I_o$  represents observed image with noise induced in the image represented with  $N$ .

$$I = I_o + N \quad (2.2)$$

Images can be affected by a variety of forms of noise, depending on the source and cause. Before applying any filter, it is necessary to determine what sort of noise in the image has to be eliminated. Here we are listing different types of noise that can affect the images and hence reducing performance of the model.

### 2.5.1 Gaussian Noise

Gaussian Noise is additionally known as electronic interference as it occurs from electronic devices such as detectors, amplifiers, etc. This type of noise can directly affects or disturbs the gray values in an image causing blurred edges and details. The pdf function can be represented as shown in equation 2.3.

$$P(i) = \frac{1}{\sigma\sqrt{2\pi}} e^{-\frac{(z-\mu)}{2\sigma^2}} \quad (2.3)$$

where,  $i$  is gray level intensity,  $\mu$  is average value, and  $\sigma$  represents average deviation. The white Gaussian noise is a particular case when values are distributed equally and are statistically separate.

### 2.5.2 Brownian Noise

Brownian interference is also commonly known as random walk noise as it is affected by signal produced by Brownian motion of suspended particles in fluid. In Brownian noise, its ability drops  $1/4^{\text{th}}$  of an interval, where the power intensity is proportionate to the square of the occurrence across that octave (6 dB per octave). The Brownian noise is represented in equation 2.4 and 2.5.

$$B_h(0) = 0 \quad (2.4)$$

$$E\{|B_h(t) - B_h(t - \Delta)|^2\} = \sigma^2 |\Delta|^{2h} \quad (2.5)$$

The process follows normal distribution with fractal noise caused by natural process. The fractal noise decays continuously due to increase in frequency, mathematically represented as zero mean Gaussian process ( $B_h$ ).

### 2.5.3 Impulse or Salt and Pepper Noise

Impulse noise or data drop noise is also known as salt and pepper disturbance. This noise is caused by abrupt and precipitous disturbances in medical image. The salt and pepper noise will change some of the pixels or values replacing by corrupted values or minimum values. The salt and pepper noise is represented as shown in equation 2.6.

$$I(x) = \begin{cases} I_a & \text{for } x = a \\ I_b & \text{for } x = b \\ 0, & \text{otherwise} \end{cases} \quad (2.6)$$

where,  $a$  and  $b$  are respective intensities in the image.

### 2.5.4 Rician Noise

Rician noise causes image quantitative estimation difficult. Rician noise is image dependent and computed for both real and imaginary image. Rician noise is mathematically represented by equation 2.7.

$$I(M) = \frac{M}{\sigma^2} e^{-\frac{(M^2+A^2)}{2\sigma^2}} I_0\left(\frac{AM}{\sigma^2}\right) \quad (2.7)$$

Where, A represents absence of noise, M is measured noise,  $I_0$  represents modified Bessel function of zeroth order, and  $\sigma$  represents standard-deviation.

### 2.5.5 Quantization Noise

Quantization noise occurs from amplitude quantization process. It generally occurs due to data conversion from analog to digital. Quantization process can be represented with uniform distribution, so it is also known as uniform noise. Quantization noise can be represented as shown in equation 2.8, where minimum and maximum pixel values are represented with a, and b.

$$Q(x) = \begin{cases} \frac{1}{b-a}, & \text{if } a \leq x \leq b \\ 0, & \text{otherwise} \end{cases} \quad (2.8)$$

### 2.5.6 Speckle Noise

Speckle noise is as well referred as multiplicative noise. This type of noise is affected by unwanted modification to a desired signal. The signal itself varies due to scatters causing difficulty for image interpolation. The speckle noise is represented as shown in equation 2.9 following gamma distribution.

$$S(g) = \frac{g^{\alpha-1} e^{-\frac{g}{a}}}{\alpha-1! a^\alpha} \quad (2.9)$$

### 2.5.7 Photon Noise

The photon noise is caused by electromagnetic radiations such as gamma, x-rays, etc. The noise causes random fluctuation of photons provided spatial and temporal randomness in the image. This type of noise is also well-known as Poisson noise or shot noise. The disturbance can be represented with Poisson distribution as represented in equation 2.10.

$$P(f_\pi) = \frac{\lambda^k t e^{-\lambda}}{k!} \quad (2.10)$$

### 2.5.8 Poisson-Gaussian Noise

The Poisson-Gaussian noise commonly occurs in MR images degrading the visual quality of the image. The joint noise models can cause difficulty in quantitative analysis of original image. The Poisson-Gaussian noise model can be represented as in equation 2.11.

$$P(x, y) = \alpha * P_{\alpha}(x, y) + G_{\alpha}(x, y) \quad (2.11)$$

where, The Gaussian distribution ( $G_{\alpha}$ ) is followed by Poisson distribution ( $P_{\alpha}$ ), with alpha value ( $\alpha > 0$ ).

### 2.5.9 Structured Noise

Stationary or non-stationary in nature is a kind of structured noise. This form of noise is caused by static amplitude or occurrence. This type of noise occurs due to obstructions in electronic devices. Structured noise is represented as shown in equation 2.12 and 2.13.

$$Y_p = x_{(p,q)} + v_p \quad (2.12)$$

$$Y_p = L_{(p,q)} * \theta_q + S_{(p,r)} * \phi_r + v_p \quad (2.13)$$

where, p and q represent rows and columns respectively. y represents the recipient image; r represents the rank in subspace. L is transfer function of linear system. S represents subspace,  $\theta$  represents signal parameter,  $\phi$  represents linear system underlying process, and vector random noise is represented with  $v_p$ .

## 2.6 Preprocessing Techniques for Knee MR Images

In this segment, numerous techniques for CNN denoising are reviewed, which are specifically applied for (i) general images and (ii) particular medical images. The initial methodology uses CNN represent common images such as natural images, symbolic images, etc. The second approach uses denoising CNN intentionally created for specific images such as medical images, remote sensing images, etc. The figure 2.13 illustrates different CNN approaches used for denoising images. As the research concentrates on specific images i.e., medical images, are discussed further. The MR images are associated with some sort of noise or artifacts that causes inadequate

contrast between adjacent tissues introducing difficulties in segmenting of tissues. Thus, preprocessing of MR images like noise filtering or denoising can be beneficial without to increase the performance of classification model without affecting image details. Currently many machine learning techniques have been developed for denoising such as support vector machine (SVM), random forest (RF), and variations in neural network. H. Wang et al., [60] introduced joint denoising convolutional neural network (JD-CNN) that captures high level features among different b-value images by connecting subnetworks. This network is similar to U-Net architecture that preserves resolution of image. A convolutional neural network with Smoothness regularizations on manifolds (SToRM)[61] denoises the image structure iterating N times.

To remove Gibbs artifacts and noise a CNN architecture in diffused images has been proposed. The model was demonstrated on canonical evaluation and image Structure was preserved, denoising with residual encoder and decoder introduced by M. Ran et al., [62]. Autoencoders with CNN for heterogenous images exploits the image details preserving local spatiality. The specific neighboring slices are utilized on generative adversarial network (GAN) estimating the distances of feature space pretrained by VGG-19 network. These GAN are composed of a generative model and a discriminative model. To suppress the impulse noise a blind CNN model had been introduced by J. Chen et al., [63]. This CNN model adapted flexible noise ratio with clean pixel median deviation (CPMD) estimating the edge pixel difference (EPD). Islam et al.,[64] suggested a feedforward network to eliminate combined noise such as Gaussian-impulse noise. A rank-order filtering technique is applied on each stage with convolutional preceded with ReLU and pooling layers.



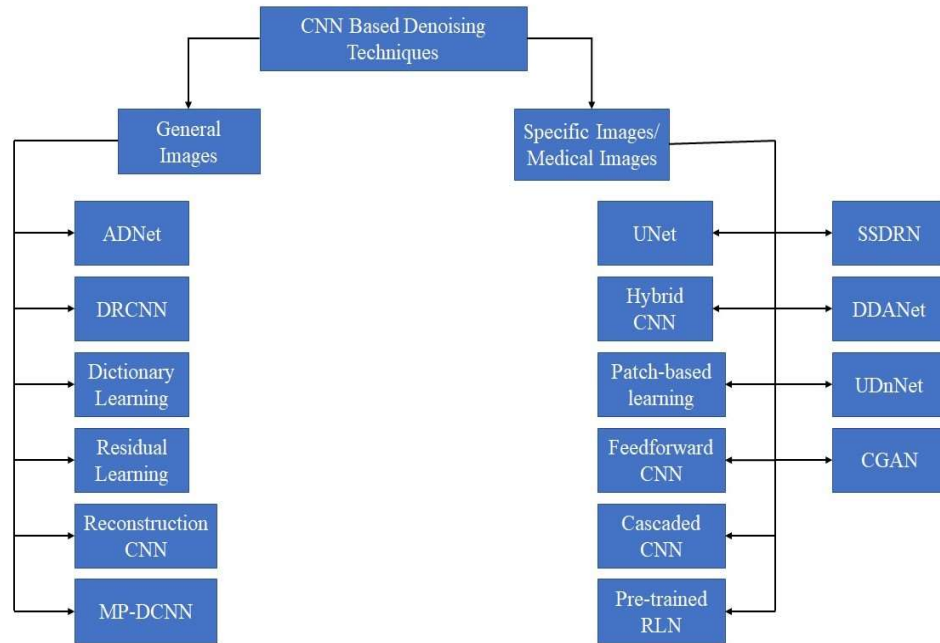


Figure 2.13. Denoising Techniques based on Convolutional neural network

Yin et al.,[65] proposed a deep learning approach based on U-Net and Noise to Noise technique. Traditionally, Gerchberg-Saxton (GS) process was utilized to produce holographs with noise reduction mechanism, obtained with learning rate of 0.001. Unlike other denoising methods SSDRN utilized batch normalization in every unit of method creating patch group to reduce the noise. Similar to that DDANet utilized bucket signal with various noise intensity maps. DDANet has twenty-one layers consisting of entirely linked layers, dense units, and convolutional layers. Zhang et al., [66] suggested a deep spatio-spectral Bayesian posterior network (DSSBPN) that produces spectral gradient for each part of the splitted image. A forward-backward propagation technique was applied to link up both deep spatio-spectral (DSS) and Bayesian posterior (BP).

Cascading residual CNN removed mixed noise combining dilated convolutional, and standard convolutional. The residual learning method estimates the calibration parameter with five feature blocks namely (feature extraction block (FEB), coarse-fine convolutional (CF-Conv), and spatial channel disturbance attention block (SCNAB)). Giannatou et al., [67] proposed a residual learning technique created on DnCNN to evaluate noise with every pixel of medical image. The input unit

comprises of convolutional layer followed by ReLU and batch normalization (BN). The output unit comprises of only a convolutional filter for restoration of the medical image. Jiang et al., proposed generative adversarial network built on UDnNet. The UDnNet composes of two sub-networks (i) a generative network and (ii) a discriminator network. The generative network produces samples with asymmetric codec composition and skip connection. The outcome of this network has convolutional instance and Normalized Leaky ReLU. Finally, a combined CNN classifier (convolutional layer, pooling layer, fully connected layer) was applied to categorize the medical images. For the assessment process, peak to signal noise ratio (PSNR), structural similarity index (SSIM), root mean squared error (RMSE), were used to denoise the image. A foremost challenge is labelling the speckle noise induced images and not labelling the ultrasound images, so it becomes difficult for identifying noise in the images.

Feng et al., [68] suggested a fusion CNN architecture for speckle noise elimination. As speckle noise is similar to Gaussian noise, the distribution parameters estimated are in logarithmic form of transformation domain. The pre-trained residual model [69] for ultrasound images with speckle noise are trained with random patches. The pretrained model consists of 59 layers with Conv, ReLU, and batch normalization (BN). Kim et al., [70] suggested the conditional generative adversarial network (CGAN) for noise elimination and forecast model. The method consists of fourteen layers from random vector noise distribution and discriminative model with 4 layers. A novel CNN-DMRI technique [71] that used convolutional for extracting image features from noise to preserve the details of the image. A down selection and up selection factor was implemented with sixty-four filters followed by convolutional layers and 128 filters in down sampling filter. Eventually, a high-quality image was obtained by extracting noise from medical image with the neural network. Further, few denoising approaches are compared with input features and outcomes. Table 2.1 illustrates several techniques for preprocessing the MR images.

Table 2.1 Preprocessing techniques with input and output parameters

<i>Author, Year</i>	<i>Input/ Features</i>	<i>Attributes/</i>	<i>Techniques Used</i>	<i>Outcome/ Results/ Application</i>
<i>SYu et al., 2016[72]</i>	Caltech101 dataset 30 subjects. VOC 2021 dataset.		Discriminative Dictionary with Convolutional neural network.	Accuracy with different images 82.9%.
<i>H. Wang et al., 2019[60]</i>	16 subjects with 400 slices.		Convolutional neural network.	PSNR average 43dB $\pm$ 1.5
<i>k. Shrinivasan et al., 2018[73]</i>	27 MR image dataset T1-weighted, T2weighted, PD images.	PD	Comparative study of different histogram algorithms.	PD images: Average PSNR 24.3dB. Average RSME 16.04. T2-weighted images: Average PSNR 22.15dB. Average RSME 20.183. T1-weighted images: Average PSNR 23.30dB. Average RSME 17.49.
<i>A. Selvi et al., 2018 [74]</i>	Natural images with noise induced externally.		Fuzzy logic with hybrid filter (mean and adaptive median).	PSNR 55.49dB for 60% noise level, 63.24dB for 10% noise level.
<i>M. Sahnoun et al., 2019 [75]</i>	120 low contrast T1-weighted MR images. (256 X 256) pixel		Discrete Wavelet Transform-	Structural similarity index (SSIM) was 0.98,

	resolution.	Singular Value Decomposition (DWT-SVD)	PSNR value obtained was 12dB.
<i>K. Chen et al., 2020 [76]</i>	Dataset 1: T1-weighted MR images. (181 X 217) resolution. Dataset 2: 8 T1-weighted MR images. (192 X 170) resolution.	Fuzzy C means and adaptive non-local means algorithm.	PSNR value was 31.8dB, SSIM was 0.83, and computational time was 16.93.
<i>H. Rai et al., 2019 [77]</i>	T1 and T2 weighted 9 subjects 27 slices images. (256 X 256) resolution.	Wavelet transform and Independent component analysis.	Noise level 10%: PSNR was 27.84dB, SSIM was 0.8337 Noise level 90%: PSNR was 18.93dB, SSIM was 0.5215
<i>P. Kuppusamy et al., 2019 [78]</i>	T2 Fluid Attenuation Inversion Recovery (FLAIR) and T1 Fast Spin Echo Contrast Enhanced (FS-ECE) images with 5mm slice thickness.	Non-local means adaptive filter.	PSNR was 28.9967dB $\pm$ 0.13
<i>I. Nagarajan et al., [79]</i>	160 MR images of type T1, T2, PD and 810 simulated images.	Block difference-based filtering.	PSNR was 45.94dB at 3%, PSNR was 30.16dB at 30% noise level. SSIM was 0.9956 at 3%

			and 0.9671 at 30% noise level. Execution time for 810 images 26.28sec.
<i>N. Mittal et al., 2019 [80]</i>	4 images of different body type with Haar level 2.	Stationary Wavelet Transform (SWT).	Average Entropy was 5.48 and average standard deviation was 68.30.
<i>V. Magudeeswaran et al., 2017 [81]</i>	Gray MR images with 10 subjects.	Bi-level fuzzy histogram equalization.	Average feature similarity index was 0.98, Average information contents was 7.36, Natural image quality evaluator was 19.88.
<i>H. Lv et al., 2019 [82]</i>	T1, T2, and PD 3D MR images (181 X 181) resolution with voxel resolution of 1mm.	Adaptive Multi-rank estimator.	T1-weighted: PSNR was 33.55dB and SSIM was 0.939. T2-weighted: PSNR was 30.39dB and SSIM was 0.940. PD image: PSNR was 32.58dB and SSIM was 0.932.
<i>K. Sharma et al., 2019 [83]</i>	T1-weighted and T2-weighted simulated	Sylvester-Lyapunov	As noise level increases the

	MR images.	equation and non-local means filtering.	PSNR level decreases. Same as with SSIM value.
<i>P. Kandhway et al., [84]</i>	MIAS, LITFL database with X-ray, MRI, CT scan images.	Krill herd optimization with histogram equalization.	SSIM value was 0.84, Edge preserve index was 1.68, Entropy was 5.06, Relative enhancement was 1.01.
<i>X. You et al., 2019 [85]</i>	40 T1w and T2w MR image. (181 X 181) and 1mm voxel resolution.	Convolutional neural network.	T1w: PSNR with 5% noise level was 37.37dB and SSIM value was 0.98. T2w: PSNR with 5% noise level was 35.28dB and SSIM value was 0.97.
<i>M. Elhoseny et al., 2019 [86]</i>	MRI brain image dataset.	Optimal bilateral filter and convolutional neural network.	PSNR 44.2dB and RMSE 0.45
<i>V. Hanchate et al., 2020 [87]</i>		Block matching combined with 3D filtering and variance	PSNR value was 43.01dB, SSIM value was 0.99, RMSE value was 0.49, Edge

		stabilization transform.	intensity was 2.75 and computation time was 546.54sec.
<i>I. Isa et al., 2017</i> [88]	25 sequences of MRI axial mode T2-weighted and FLAIR images. (512 X 512) resolution.	Average Intensity Replacement based on Adaptive Histogram Equalization (AIR-AHE).	Average PSNR value was 87.36dB and average gradient value was 0.0008

## 2.7 Segmentation and Feature Extraction Approaches

Over the last two decades, numerous attempts have been made to quantify tissue morphology as far as spacing, volume and compositions, such as water, collagen, synovial fluid, are concerned. Out of which MR image has proven as gold standard as it produces excellent detailed joint resolution for quantification. Segmentation of tissues are performed by experts (manually), semi-automated approaches [89] or using automated approaches[90]. However, development of computational approaches is difficult due to challenges as discussed in section 2.2.

### 2.7.1 Manual Techniques

It is commonly found that manual MR-image segmentation procedures make computing approaches trustworthy and accurate. The tissue is divided by experts slice by slice from 2D MR images in manual procedures. Although, manually segmentation is referred as benchmark to assess the performance, but it requires more time for experts with efforts and may lead to inter-observer and intra-observer variability. As these manual techniques are not preferred in clinical practices. Figure 2.14 illustrates the pipeline architecture of manual segmentation that involves experts intra and inter observation.

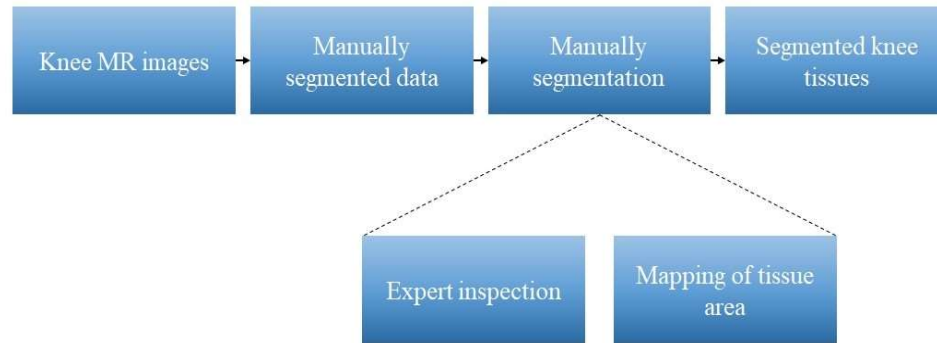


Figure 2.14. Manual segmentation architecture



Figure 2.15. Manually segmented femoral and tibial cartilage from MR image.

### 2.7.2 Semi-Automatic Techniques

Semi-automated segmentation methods [89] have minimal human interaction, which enables accurate illness detection with decreased effort. These methods carry out certain stages with automatic processing and remaining steps followed by human interaction intended for precise results. Generally, semi-automated methods segment different tissues from MR image involves combination of some image processing techniques such as region-based segmentation, active shape model, watershed method, graph-based model, etc. These quantitative approaches are utilized for the segmentation of knee MR imaging tissue. There are several quantitative parameters to



measure the performance using a validation method. Table 2.3 describes several semi-automated methods for segmentation. Figure 2.16 shows semi-automatic segmentation process.

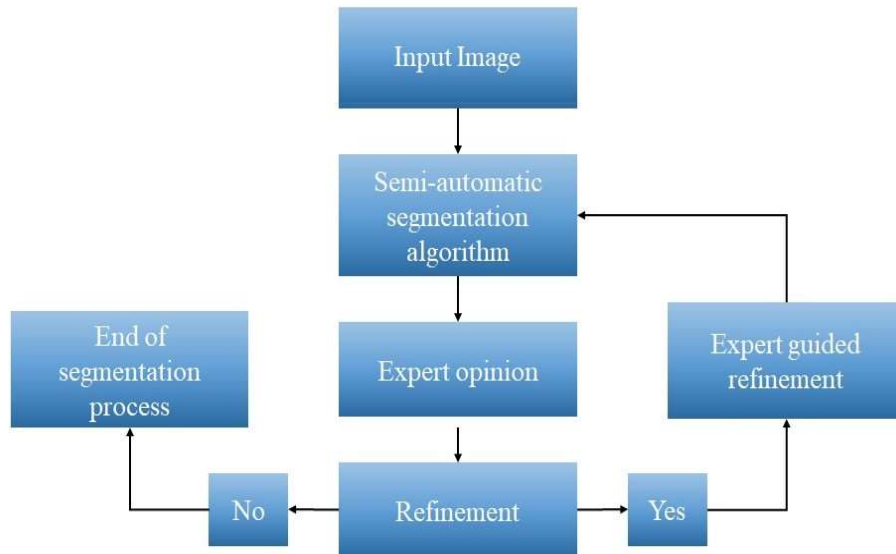


Figure 2.16. Semi-automatic segmentation process

M. Marcan and I. Voiculescu[91] proposed Image partition forest technique that increases the partitions layers across adjacency graph. Paired scan technique with initial evaluation for quantification using active contour model to refine segmented margin. H. Ng et al., [92] proposed improved watershed method that performs thresholding on gradient magnitude with histogram and provides edge map pixels with higher thresholding retains their original values. Quantitative measurement of local variation of joint space with high resolution images are initialized with snake contour method. The improved watershed transform [93] with prior information was proposed with mapping function between pixels. Triplanar convolutional neural network proposed by A. Paasoon et al., Convolutional layers learn small features with random patches from a large image. Subsampling layer reduces number of features to reduce computational complexity, and overfitting issues. M. Swanson et al., [94] proposed a Gaussian fit model using manually selected seed point within the meniscus and estimating the threshold level.

A patch-based iterative technique on atlas selection and label fusion for constructing a Gaussian image pyramid was suggested by Z. Wang et al., [95]. The patch-based method overcomes the problems of multi-atlas approach where structural inconsistency cannot be completely registered. K. Zhang et al., [96] proposed support vector machine combined with discriminative random fields for pixel classification of spatial dependency and to employ feature set encoding. The method also extracts local geometric structure-based features with Gaussian smoothed intensity.

Table 2.2 Semi-Automatic Segmentation Techniques for Knee MR Images

<i>Author, Year</i>	<i>Input/ Attributes/ Features</i>	<i>Techniques Used</i>	<i>Outcome/ Results/ Application</i>
<i>M. Marcan et al., 2016 [91]</i>	12 patients of proton density weighted sequence (PDW SPAIR) MR Imagewith femur and tibia bone obtained using Mimics software.	Image Partition Forest.	Average symmetric surface distance was 0.98mm for femur and 0.73mm for tibia. DSC was 0.95 for femur and 0.93 for tibia.
<i>M. Baldwin et al., 2010 [97]</i>	MR Images with features such as femur, tibia, and patellar cartilage.	Mesh-morphing platform	Edge length of femoral cartilage was 2.0mm-2.5mm, Medial and lateral tibial cartilage was 1.8mm, and patellar cartilage and bone was 2.8mm.
<i>A. Faisal et al., 2015 [98]</i>	19 asymptomatic subjects parallel segmented for	Local regional information on expandable	DSC for femoral condyle was 0.91, meniscus was 0.88,

	femur, tibia, and meniscus tissues.	kernel(LREK) with Active contour.	and tibial plateau was 0.94.
<i>H. Gan et al., 2016</i> [99]	DESS with water excitation for cartilage segmentation.	Conventional semi-automated seed generation model with k-means clustering.	Dice coefficient of femur was 0.11, tibia was 0.10, and patella was 0.10.
<i>A. Faisal et al., 2017</i> [100]	80 subjects with short axis view of femoral cartilage with knee fully flexed.	Locally statistical level set method (LSLSM).	DSC and Hausdorff distance with average value of $0.91 \pm 0.01$ and $6.21 \pm 0.59$ respectively.
<i>H. Ng et al., 2006</i> [92]	50 T1-weighted images with edge mapped.	K-means clustering and improved watershed algorithm.	Number of partitions for an image achieved nearly 85-90%.
<i>A. Prasoon et al., 2013</i> [101]	114 subjects with 2 million voxels.	Triplanar Convolutional Neural Network	The average DSC of 0.79, accuracy of 99.91%, sensitivity of 78.58%, and specificity of 99.95%.
<i>Z. Zhou et al., 2017</i> [102]	20 subjects with 8 channel phased array and 45 image slices.	Convolutional Encoder Decoder architecture.	DSC value of 0.97 for femur, 0.96 for tibia, 0.93 for muscle, 0.91 for other tissues. DSC value of 0.806 for femoral

			cartilage, 0.801 for tibial cartilage, 0.898 for patella, 0.807 for patellar cartilage, 0.831 for meniscus, 0.815 for tendons.
<i>K. Zhang et al., 2013 [103]</i>	MR sequence spatially associated using an automatic multi-modal registration algorithm.	SVM with spatial dependencies.	DSC value of 0.864 for femoral, 0.880 for tibial, and 0.841 for patellar.
<i>Z. Wang et al., 2013 [95]</i>	Multi-resolution with Atlas selection providing spatial information.	Patch-based segmentation without registration.	AvgD, and RMSD of 1.72mm, 2.36mm for femur, 1.74mm, 2.40mm for tibia respectively. Volumetric overlap error (VOE) of 75.7mm for femoral cartilage, 76.8mm for tibial cartilage. Volumetric difference (VD) of -6.3 for femoral cartilage and -2.2 for tibial cartilage.

### 2.7.3 Automatic Techniques

Automatic segmentation techniques are performed with extensive research where the process need to be complete fast and reliable. Research shows that development of segmentation technique to segment tissues from MR images are fully automated[89]. To assess the disease with valuable information segmenting various tissues, there are automated methods such as statistical methods, optimal graph, registration methods, etc. Table 2.2 illustrates several automated methods for segmentation of knee MR images.

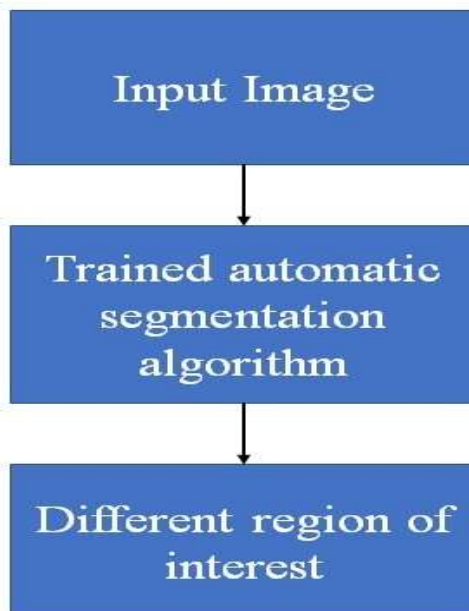


Figure 2.17. Automatic Segmentation process

C. Ozturk and S. Albayrak[104] suggested auto-segmentation technique using the region-growing algorithm of an enhanced voxel classification. The central coordinate computation with subsampling and dimensionality reduction are significant features of the method. H. Seim et al., [105] suggested statistical shape model and graphic-based optimization for the femur and tibia tissue surface segmentation. Bone regions are selected with side selection and positioning with parameter initialization and cartilage surface is selected with minimum and maximum intensity profile. Segmentation of levels based on adaptive strength function and template has been

proposed by C. Ahn et al. [106]. The contours are accepted and shifted by reducing local intensity using the automated initialization spatial fuzzy means. The template provides initial contours for femoral, tibial, and patella cartilage. F. Ambellan et al., [90] proposed convolutional neural network and statistical shape knowledge to extract anatomical shape. H. Bakir and J. Zrida[107] proposed a combined approach of vector field convolution (VFC) and radial search algorithm. The algorithm finds the femoral center, which receives the edge map with a canny detector.

J. Folkesson et al., [108] proposed k nearest neighbor classifier for cartilage segmentation. The images were manually labelled to describe the geometry of the cartilage. Sixty features establishing a tolerance level for the method to perform posterior probability. A voxel classification (kNN classifier) [43] that defines three classes to separate tibial medial cartilage, femoral medial cartilage, and background. It selects randomly sampled voxels (cartilage), and process continues selecting neighboring voxels until no voxel is found. J. Lee et al., [109] proposed a multi-atlas and local structure analysis method that applies local weights and region adjustment by graph-cut method. This method optimizes the operational parameters and provides ability to examine internal operation. C. Kauffmann et al., [110] proposed quantification approach for volume, and thickness of cartilage. A two-dimensional active contour method was used to extract the edges with continuous iteration over the boundary. J. tang et al., [111] proposed directional gradient vector flow (GVF) snakes to extract surface and thickness of cartilages. The GVF are computed by diffusion process utilizes edge detection for estimating the boundaries using map function.

Table 2.3 Automatic Segmentation Techniques for Knee MR Images

<i>Author, Year</i>	<i>Input/ Attributes/ Features</i>	<i>Techniques Used</i>	<i>Outcome/ Results/ Application</i>
Z. Zhou et al., 2017 [102]	7 different tissues femoral cartilage, tibial cartilage, patella, patellar cartilage,	Convolutional neural network	Dice coefficient for femoral cartilage 0.806 ± 0.062, tibial cartilage 0.801 ±

	meniscus, quadriceps, patellar tendons, and infrapatellar fat pad.		0.052, patella 0.898 ± 0.033, patellar cartilage 0.807 ± 0.101, meniscus 0.831 ± 0.031, quadriceps and patellar tendons 0.815 ± 0.029, infrapatellar fat pad 0.882 ± 0.040.
<i>A. Tack et al., 2018</i> [112]	88 subjects with Meniscus volume, tibial coverage, meniscus extrusion.	U-Net architecture	Dice similarity coefficient: medial meniscus 83.8%, lateral meniscus 88.9%.
<i>L. Shan et al., 2014</i> [113]	Femoral cartilage, Tibial cartilage	Three-label atlas method	Femoral cartilage: mean value was 0.856, median was 0.862, standard deviation was 0.057. Tibial cartilage: mean value was 0.859, median was 0.861, standard deviation was 0.047. Computational time 9hours.
<i>A. Raj et al., 2018</i>	176 knee MR	Fully Volumetric	Dice score of

[114]	images with structures such as (femoral cartilage, left and right tibial cartilage, left and right menisci, and patellar cartilage)	Convolutional neural network ( $\mu$ -Net)	femoral cartilage was 0.834 and tibial cartilage was 0.825. Volume overlap error (VOE) was 28.302 and volume difference was 12.504.
<i>C. Lindner et al., 2013</i> [115]	Femur bone, tibia bone.	Random forest regression voting	Global search error 99.0%, median value 91.2%
<i>S. Kashyap et al., 2016</i> [116]	15 subjects with 53 MR images for femur and tibia tissues.	Hierarchical Classifier and Random forest for feature set.	Signed 0.03 and unsigned femur value 0.55. Signed 0.10 and unsigned tibia value 0.61.
<i>J. Fripp et al., 2010</i> [40]	20 subjects of FS SPGR MR sequence containing. Bone cartilage extraction and articular cartilage	Flokesson method with non-rigid scheme registration.	DSC of 0.83, 0.83, 0.85 for patellar, tibial, and femoral cartilage respectively. Median volume difference error 4.65, and absolute thickness difference was 0.24mm.
<i>E. Dam et al., 2015</i> [117]	140 knee MR images with tibial	Multi-atlas registration	Volume overlaps for tibial and



	lateral and medial cartilage, femoral lateral and medial cartilage, lateral and medial meniscus		femoral medial cartilage compartments were 0.804 and 0.866 respectively.
<i>C. Chu et al., 2015</i> [118]	30 CT scan images with inter-slice resolutions of 1.6mm	Multi-Atlas Segmentation Constrained Graph (MASC G)	Average surface distance error of 0.16mm, 0.21mm, 0.20mm for acetabulum, left femur, right femur respectively. Computational time was 3.05 min
<i>A. Gandhamal et al., 2017</i> [119]	160 slices of preprocessed MR images with tibia and femur bones.	Seed point detection applying 3D multi-edge intersecting approach.	Mean sensitivity 91.14%, specificity 99.12%, and dice similarity coefficient (DSC) 90.28%.
<i>F. Ambellan et al., 2018</i> [90]	60 training samples applied for medial and lateral tibia cartilage.	Statistical structure learning and CNN.	DSC was 98.6% for femur and 98.5% for tibia tissue, 89.9% for femur and 85.6% for tibia cartilage.
<i>H. Seim et al., 2010</i> [105]	60 MR image subjects with no and mild symptoms.	Side selection and positioning, with graph cut method.	DSC achieved was 0.84, sensitivity was 94.1%, specificity was

			99.9%, and average surface distance was 0.49mm. Cartilage was $54.4 \pm 8.8$ points.
<i>C. Ahn et al., 2016 [106]</i>	20 preprocessed cartilage samples with advanced normalization tool to create template image.	Level-set based algorithm.	DSC of 87.1%, 84.8%, and 81.7% were achieved for femur, patella, and tibia cartilage.
<i>C. Ozturk et al., 2016 [104]</i>	33 subjects preprocessed for noise removal with smoothed intensities.	Seed selection and region growing algorithm.	DSC of 82.6%, 83.1%, and 72.6% for femur, tibia, and patella cartilage are achieved. Sensitivity of 79.9%, 84.0%, 71.5%, and specificity of 99.8%, 99.9%, 99.9% for femur, tibia, and patella cartilage are obtained.

### 2.7.4 Feature Extraction Techniques

Joint space narrowing (JSN), cartilage thickness, tissue erosion are few feature inputs for classification of RA severity. These individual features were continuously

assessed for evaluation of KL grading, and significant correlation between them. To examine the progress of knee tissue severity, B. Ashinsky et al., [120] suggested MR-classification approach employing weighted neighboring distances using the complex hierarchy of morphological algorithms (WND-CHRM). The cartilage mask is segmented with medium femoral slices bearing center weight. The biomarker [13] in cartilage thickness loss was measured by analyzing central, external, internal, anterior, and posterior subregions of tibial with central, external, internal femoral subregions.

N. Bien et al., proposed deep learning assisted diagnosis method (MRNET), a convolutional neural network with 50 iterations. A weighted average of 256 CNN feature maps is generated with logistic regression to weight the prediction. S. Gaj et al., suggested an automatic method for feature segmentation of cartilage and meniscus with conditional generative adversarial networks (CGAN) [121]. Generative adversarial networks (GAN) consist of two networks, first network (G) producing synthetic samples, and second discriminator (D) acting as binary classifier. In CGAN, the G is a mapping function which is defined as  $G(y) = \hat{x}$ , where  $\hat{x}$  defines segmented mask. The loss function is solved by training the discriminator (D) with synthetic and manual segmentation masks. A computer aided method for meniscal tears was introduced by A. Saygili and S. Albayrak. HOG method (rectangular window) was implemented to extract the features containing spatial information and membership weights distributed across the image pixels. M. Byra et al., [7] proposed attention U-Net by outlining region of interest (ROI) by manual experts. Self-attention mechanism was used to improve segmentation for small objects leading to more focused ROI. Table 2.4 describes the quantitative assessment features with MR image sequences.

Table 2.4 Quantitative evaluation of RA Knee features

<i>Assessed features</i>	<i>Image planes</i>	<i>MR image sequences</i>
<i>Bone lesions</i>	Axial, sagittal, coronal	T2-weighted fat saturated FSE or PDw fat-saturated FSE or

		STIR.
<i>Articular cartilage</i>	Sagittal	3D high resolution GRE sequence and T2-weighted fat saturated FSE/ TSE.
<i>Synovitis or synovial fluid</i>	Sagittal	T2-weighted fat-saturated FSE/TSE or PDw fat-saturated FSE/TSE.
<i>Meniscus</i>	Coronal, sagittal	T1-weighted fat-saturated spin-echo. T2-weighted fat-saturated FSE/TSE. PDwfat-saturated FSE/TSE.
<i>Ligaments</i>	Axial, coronal, and sagittal	PDwfat-saturated FSE/ TSE.
<i>Osteophytes</i>	Axial, sagittal, coronal	3D high resolution GRE sequence and T2-weighted spin-echo sequences.

B. Normal et al., [34] proposed automated CNN for cartilage and meniscus feature extraction. The model experiment was performed on DESS datasets for evaluating dice coefficient. V.Pedoia et al., [122] suggested severe meniscus and cartilage staging that was utilized to assess with 3D CNN technique. Meniscus and patellar cartilaginous anterior and posterior areas have been assessed with the entire MR tissue image scoring method adjusted (WORMS). A. Tack et al.,[112] proposed statistical shape model (SSM) for lateral and medial meniscus generating triangulated meshes. SSM with CNN were employed for segmentation masks using voting scheme. Extreme learning machine was introduced by K. Zhang et al., [123] for discriminative random fields (DRF) to estimate neighboring voxels in spatial dependencies.

E. Choi et al., [124] proposed XGBoost algorithm that is combination of (random forest and extreme gradient boosting). This method evaluates synovial white blood cell (WBC) count to diagnose arthritis with multivariate analysis. The model was applied on independent dataset for estimating the probability and discriminatory power. R. Hemalatha et al., proposed automatic detection and diagnosis of arthritis with grading of synovial region. The process of localization for each segment are determined by different algorithms. Bone region localization is detected by Hit or miss transform (HMT) algorithm that works on intensity variation and signal strength. The joint region localization is detected by Euclidean distance map and intensity profile as shown in equation 2.13. The knee joint region is determined based on the distance between the bone structure. The position of tissue joint is defined with pixel intensity profile. The synovial region localization is detected by active contour technique. The synovial region is then graded with CNN with 20 layers consisting of input, output, kernels, pooling, and fully connected layers.

$$d(x, y) = d(y, x) = \sqrt{\sum_{i=1}^n (y_i - x_i)^2} \quad (2.13)$$

I. Iqbal et al., [125] suggested transfer learning method on knee joints to identify the synovial fluid. The residual network (ResNet) consisting of nine convolution layers for identifying unpretentious structures such as femoris and tibial tissue, thirty convolution layers for intricate areas such as patellar, seventy-five convolution layers for more multifaceted structures such as synovial fluid, then remaining nine convolution layers for precise features. The Tensorflow interface library evaluates the model on COCO dataset. T. Perry et al., [126] proposed semi-automated quantitative approach for measurement of synovial tissue. The synovitis region was estimated using active appearance model (AAM), targeting the threshold synovitis voxels with manual editing the volume. B. Heard et al., [37] proposed a method for categorizing normal and abnormal patients in arthritis. The artificial neural network (ANN) technique significantly identifies cytokines biomarkers with high level of sensitivity and specificity. Table 2.5 describes the several features of knee and their techniques with outcome.

Table 2.5 List of features selected for knee RA

<i>Author, Year</i>	<i>Features selected</i>	<i>Techniques Used</i>	<i>Outcome/ Results/ Application</i>
<i>N. Bien et al., 2018 [127]</i>	Anterior cruciate ligament (ACL) and meniscus tears	MRNet with class activation mapping	AUC of 0.937, 0.965, and 0.847 for abnormality detection, ACL tear, and meniscus tear respectively. Kappa grade of 0.508, 0.800, and 0.745 for abnormality detection, ACL tear, and meniscus tear respectively.
<i>A. Saygili and S. Albayrak, 2017 [128]</i>	Knee meniscus	Extreme learning method (ELM) and random forest (RF)	Dice similarity measurement of 82%. Sensitivity 99.78%.
<i>I. Stajduhar et al., 2017 [129]</i>	ACL injury and rupture from sagittal knee MR images.	Histogram of oriented gradient (HOG) descriptor, SVM and RF	AUC of 0.894 for wrong discovery and 0.943 for shatter recognition.
<i>C. Ozturk and S. Albayrak, 2016 [104]</i>	Cartilage	Voxel classification driven region growing algorithm and vicinity correlated subsampling	Mean DSC value 82.6%, 83.1%, and 72.6%, Sensitivity of 79.9%, 84.0%, and 71.5%, and specificity of 99.8%, 99.9%, and 99.9%,

			for femur, tibia, and patella cartilages respectively.
<i>R. Cheng et al., 2019</i> [130]	2D sagittal surface of femur, patella.	Holistically nested network (HNN) architecture	Average absolute error value 0.33mm, dice coefficient of 97%, 94% for patella and femur.
<i>E. Dam et al., 2018</i> [131]	Cartilage cavity and lesion volume.	Gradient peak method	Cartilage cavity was 7.1%/3.0%.
<i>F. Liu et al., 2017</i> [132]	Tibia, femur, and patella cartilage	SegNet CNN architecture	(Volumetric difference (VD), Volume overlap error (VOE)) values for femur tibial, and patellar cartilage are (29.1%, 4.6%), (33.4%, 1.6%), and (24.2%, 7.1%)
<i>T. Perry et al., 2018</i> [126]	Synovial tissue volume	Active appearance modelling (AMM)	Mean difference 207.2mm, confidence interval 95%, intra-observer correlation coefficient 0.83.

## 2.8 Diagnostic and Grading Approaches

Knee arthritis scoring/ grading depends upon pathological features like tissue erosion, changes in tissues and joint space width. These parameters are directly associated with scoring system such as KL grading system. Kellgren and Lawrence (KL)

classifying method measures RA severity of knee under five categories. In this literature review the categorization evaluation for analysis of knee severity is approached in two ways (i) classification based on grading system such as KL grade, (ii) classification based on quantification of features.

An automatic diagnosis for RA with KL-score was suggested for knee MR image assessment was achieved, applying various transformations. Simple weighted nearest neighbor (SWNN) was applied to categorize the basic modality images with KL score. The method was enhanced employing a new method using morphological algorithm. The method first extract features and further classifies the images into normal and abnormal. The extracted features are then classified using support vector machine (SVM) and random forest (RF) to standardize the automatic classification of knee RA. T. Yang et al., [133] classified ultrasound images with SVM and various feature descriptors. The method separates synovial region and phalangeal bone region with Otsu's method.

A fine-tuned CNN architecture proposed by J. Antony et al., [134] quantifies the severity of knee arthritis. The CNN architecture uses 5D fully connected layer, softmax function and regression network with linear activation. The regression network is trained with regression loss and rounded labels. P. Chen et al., [58] proposed fully automatic severity grading using CNN classifier. The ResNet34 architecture also provides cross entropy loss and ordinal loss to achieve best accuracy. The artificial neural network (ANN) proposed by Y. Du et al., [135] consists of single hidden layer with n neurons constructing hyperplanes with map function. Y. Feng et al., [136] proposed a combined architecture of highway network, CNN, a residual network. The highway network is likelong shortterm memory (LSTM) in conjunction with 18 layers and 150 units in each layer. CNN consisting of 32 filters and residual network (ResNet) with 20 layers that solves the degradation problem.



Table 2.6 Classification Techniques with KL-grading for Knee MR Images

<i>Author, Year</i>	<i>Input/ Attributes/ Features</i>	<i>Techniques Used</i>	<i>Outcome/ Results/ Application</i>
<i>K. Ureten et al., 2019 [137]</i>	180 Images of normal and rheumatoid arthritis (RA) cases with swelling, pain. Data augmentation is used for irrelevant patterns, and overfitting problems.	Convolutional Neural Network (CNN).	Accuracy of 73.33%, error rate of 0.0167, sensitivity of 0.6818, specificity of 0.7826, and precision of 0.7500 was achieved.
<i>B. Liu et al., 2019[138]</i>	2770 random images were labelled into 5 groups using KL grade scheme.	Faster R-Convolutional Neural Network (FCNN).	Standard precision of 0.82, sensitivity of 78%, specificity of 94%.It took 0.33s to test each individual image.
<i>P. Chen et al., 2019 [58]</i>	1656 knee image joints splitted into 639 for grade 0, 296 for grade 1, 447 for grade 2, 223 for grade 3, 51 for grade 4 manually annotated to measure joint space.	Convolutional Neural Network.	Accuracy of 70.4%, Mean absolute error (MAE) of 0.358.
<i>K. Thomas et al., 2020 [139]</i>	4090 images pretrained from	169-layer convolutional	Accuracy 87.2%, Precision 0.884,

	ImageNet.	neural network.	Recall 0.849, F1-score 0.866.
<i>B. Norman et al., 2018 [140]</i>	40490 bilateral PA fixed-flexion images localized using U-Net model.	Densely Connected Convolutional Neural Network (Dense-Net)	Sensitivity value for no arthritis was 83.7%, mild arthritis was 70.2%, moderate arthritis was 68.9%, and severe arthritis was 86.0%. Corresponding specificity values were 86.1%, 83.8%, 97.1%, 99.1%.
<i>Y. Huang et al., 2020</i>	3740 images segmented of metacarpal bones and analyzed for textual features.	Deep ten-network	ROC curve was 0.69, positive predicted value was 0.64.
<i>J. Antony et al., 2016 [134]</i>	4476 images with grade 0 consisting of 3233, grade 1 with 1589, grade 2 with 2355, grade 3 with 1222, and grade 4 with 295.	Convolutional Neural Network.	The multiclass classification accuracy of network with regression loss was 59.6%. Mean precision was 0.43, recall was 0.44, f1-score was 0.43.
<i>J. Antony et al.,</i>	Automatically	Fully	Accuracy 60.3%,

2017 [141]	localized and extracted knee joints from 1200 images.	Convolutional Neural Network (FCNN).	Mean-squared error 0.898. ROC (AUC) for grade 0 was 0.87, grade 1 was 0.71, grade 2 was 0.82, grade 3 was 0.96, and grade 4 was 0.99.
<i>S. Dang et al., 2020</i> [142]	416 samples with hand joints one joint at least scoring 3 and above.	Convolutional Neural Network.	Accuracy was 90.8%, Root mean square standard deviation (RMSD) was 15.6635.
<i>J. Cheung et al., 2020</i> [143]	Images annotated with distal femur and proximal tibia for estimating tibiofemoral joint.	Convolutional neural network with ResU-Net architecture.	Joint space width (JSW) of 0.7801. For 32-point multiple JSW AUC score was 0.656 progression to 0.587 and 0.554.
<i>R. Hemalatha et al., 2019</i> [35]	Preprocessed images with bone localization using HMT algorithm, and synovial region localization with active contour technique.	Convolutional neural network.	Accuracy $95.02 \pm 2.78$ , Precision $95.42 \pm 2.08$ , Specificity $95.86 \pm 1.98$ , Sensitivity $98.02 \pm 0.78$ .
<i>T. Hirano et al., 2019</i> [144]	108 subjects clipped and scored for bone erosion	Convolutional neural network.	Accuracy of model and clinical data was 49.3-65.4% for

	and joint space narrowing.		JSN, and 70.6-74.1% for erosion. Sensitivity and specificity were 88.0-94.2% and 52.0-74.8% for JSN and 34.8-42.4% and 88.2-89.4% for erosion respectively.
<i>S. Murakami et al., 2017 [32]</i>	129 cases with removal of soft tissues, initializing phalanges region by multiple scale gradient vector flow.	Deep CNN.	Bone erosion: Average True positive rate 80.5%, false positive rate 0.84%.
<i>J. Rohrbach et al., 2019 [145]</i>	Images with Ratingen score stage 0: 69067, stage 1: 27853, stage 2: 2316, stage 3: 1041, stage 4: 597, stage 5: 1391.	VGG16 with Adam optimization.	Global accuracy of 77.5%, Balanced accuracy of 82.9%.
<i>R. Wahyuningrum et al., 2019 [146]</i>	4796 preprocessed images and feature extracted using Visual geometry group (VGG-16).	CNN combined with LSTM	Average accuracy of 75.28% is achieved.
<i>S. Shanmugam et</i>	Learning data with	Machine learning	AdaBoost gave

<i>al., 2018 [147]</i>	sample set independently that fit in memory.	based Ensemble Analytic Approach (MLEAA).	best accuracy of 85%, then SVM provided with 75.4%, ANN and Naïve Bayes provided 72.2% and 71.1% respectively.
<i>H. Nguyen et al., 2019 [148]</i>	3445 images with grade 0 consisting of 1550, grade 1 with 568, grade 2 with 520, grade 3 with 559, and grade 4 with 248.	Semixup: In and out manifold regularization.	Accuracy of 70.9% $\pm$ 0.8 was achieved. Mean squared error (MSE) was 0.440, and AUC was 0.963 for (KL>2).

## 2.9 Observations

Joint space narrowing evaluation is the primary stage in determining knee rheumatoid arthritis development (RA). The assessment can be done with proper segmentation and feature extraction from MR images. The segmentation can be discussed into three different categories manual, semi-automatic and automatic. Manual segmentation is very tedious due to difference in inter-observer and intra-observer assessment. Studies have shown significantly large variations resulting lower clinical significance. In comparison to the conventional approach, the semi-automatic would be less tedious, but the intra- and inter outcomes stay the same. All the semi-automatic techniques quantify maximum specificity and sensitivity by using watershed-based methods. Many researchers have developed automated segmentation approaches with a view to eliminating the intra- and inter-server unpredictability that generates mistakes, both manually and semi-automatically.

Automated techniques are very reliable and robust, but validation of these techniques is required for satisfactory results. These automated techniques are based on region growing, seed selection point, and based on voxels of tissues. Some researchers have also come up with techniques such as multi-object, multi-contrast, and multi-level segment. Although there are numerous automated segmentation approaches accessible in the study, many of which have gaps as outlined in Table 2.6. All the preceding studies indicate substantial changes which might lead to low clinical relevance. Based on the above studies table 2.7 have been prepared. This table illustrates the detailed applicability of techniques with arthritis disease, and diversified features applicable for the disease.

Table 2.7 Techniques applied for arthritis disease

*Arthritis disease features*

	Cartilage	Meniscus	Lesions	Ligaments	Synovial fluid	Femur bone	Tibia bone	Patella bone
<i>SVM</i>	2	1				1	1	1
<i>RF</i>	1	1				1	1	
<i>DT</i>		1						
<i>ANN</i>	1	1				1	1	1
<i>CNN</i>	4	2	1	1	1	5	5	5
<i>K-means</i>	1	1						
<i>Seg-Net</i>	1	1				1	1	1
<i>U-Net</i>	2					2	3	1
<i>ResNet</i>	2	1						
<i>VGG</i>	2					1	1	
<i>HNN</i>							1	1
<i>Dense-Net</i>	1	1						
<i>AMM</i>					1			

During the study it has been observed that the term “Intelligent medical diagnostic system” has not at all used as keyword in any article. Instead of this many articles refer the terms like ANN, CNN, hybrid technique, or integrated technique, DWT, etc. So, in this thesis we introduce a new keyword “Intelligent Medical Diagnostic System” which refers to all the methodologies mentioned in this thesis. Along with many benefits, preparing the literature review also has several limitations. The author must gather extensive information for studying, and classifying the articles based on techniques used, publication language other than English cannot be included, limit the number of databases and time constraint. Hopefully, this thesis provides researchers a quantitative state-of-the-art and systematic review in developing medical decision-making for assessing the rheumatoid arthritis (RA).

Many quantitative approaches are based on a KL grade provided in Table 2.8 to evaluate the progression or diagnosis of MR images. The joint space width/ narrowing assessment is involved in RA progression, where knee whose KL grade is  $\leq 1$ , is considered normal or doubtful RA. If KL grade  $\geq 2$ , then considered as mild, moderate, or severe RA. Therefore, grading is foremost important for fair measurement of RA progression. Automated RA severity assessment comprises two phases: (i) automatic area of concern detection (ROI), (ii) knee joint classification. Many researchers have examined automated techniques; however, this is a challenge.

Table 2.8 KL grading for arthritis progression

<i>KL grade</i>	<i>Description</i>
0	Normal joint space and no possibility of RA.
1	Uncertain reduction of joint space and possibility of RA.
2	Potential reduction of joint space and significant (mild) RA.
3	Obvious reduction of joint space and moderate RA.
4	Apparent reduction of joint space and critical RA.

## 2.10 Conclusion

This chapter addresses the issues in the present techniques such as to denoise, automatic segmentation with no human intervention. Mostly, the CNN and its variant techniques outperforms most of the studies. Some approaches are assessed on ground truth and existing techniques for comparison. The subsequent chapters discuss proposed architecture of denoising, segmentation, and classification in detail.

Researchers have proposed many studies based on segmentation, feature extraction, and classification approach as reviewed and discussed in previous sections. These approaches are preferred on different selection criteria such as features (cartilage, meniscus, synovial fluid, lesions, and tissues). There are various techniques to knee RA assessment in the literature using image functionality extracted, particularly GLCM, statistical features, local binary pattern. There are some approaches that uses large number of feature set based on pixel, objects, edge, texture, histogram, and transforms. Various ML classifications such as K neighbor (KNN), vector aid (SVM) as well as decision tree model (RF) have been introduced. But these techniques still have inadequate multi-class assessment effectiveness, and a difficulty continues to classify the knee RA.

In recent years, the use of deep learning approaches has outperformed many techniques. Specially in deep learning work in the realm of disease, such as formal feature extraction, segmentation of tissue in knee MR image, deep neural network (CNN) has proven immensely effective. Even though automatic techniques provide best outcomes and have much scope in the research but lacks as discussed above. Most approaches initially need a high level of training and even a minor change in training instances influences the result. The approaches offered demand a significant amount of time and even significant computations. This thesis therefore gives investigators with an opportunity to provide efficient time and computation approaches to this area of study. The performance of the proposed new architecture is also analyzed on a comparable scale with the existing system for a reasonable and accurate evaluation. Further, the subsequent chapters discuss the proposed architecture in-detail.



## **Chapter 3**

# **Denoising MR Images Using Sparse Aware Noise Reduction with Convolutional Neural Network and Dictionary Learning**

This chapter presents the proposed denoising technique using CNN. The chapter is organized as follows: Section 3.1 describes the need of preprocessing. Section 3.2 presents the introduction. Section 3.3 describes the pre-processing methodology used for denoising knee MR images. Section 3.4 discusses the details of the experiment carried out and the findings achieved. The chapter concludes with Section 3.5.

### **3.1 Need of Preprocessing**

Intelligence medical diagnostic systems (IMDS) or Computer aided diagnosis (CAD) systems are growing rapidly to detect and diagnose RA automatically. Such systems rely on the images obtained from the various medical imaging modalities. Segmentation and feature extraction are important steps in diagnosis of RA from MR images using intelligent systems. These images are prone to noise, inadequate contrast, and brightness that restricts the diagnosis of disease. Performance of these intelligent systems are also degraded by misinterpretation of knee features by experts. The design and development of IMDS depends on image quality and features to be used[149]. Now-a-days due to high quality medical machines the contrast and brightness are of superior quality. However, most of the images acquired using MR imaging modality exhibit noise that leads to difficulties in quantitative measurements such as segmentation, categorization and assessment of tissue-related morphological characteristics.

Insufficient brightness also negatively impacts the possibility to segment and classify the inadequate tissue limits of the intelligent system. Other challenges in MR images also includes the complex knee structure, varying intensities of single tissue due to the preferential impact of volume[150]. The in-detail challenges are discussed in section 2.2, that leads to improper diagnosis of RA. Figure 3.1 shows the noise and contrast issues in knee MR images. Therefore, pre-processing is important step because of

noise present in medical images that leads to inaccurate segmentation of tissues and in-turn affects the diagnosis capability of IMDS. Therefore, the Gaussian noise is recommended to be filtered from medically based images as part of the pre-procedure approach to this thesis Sparse Aware Noise Reduction using Convolutional Neural Networks (SANR CNN).

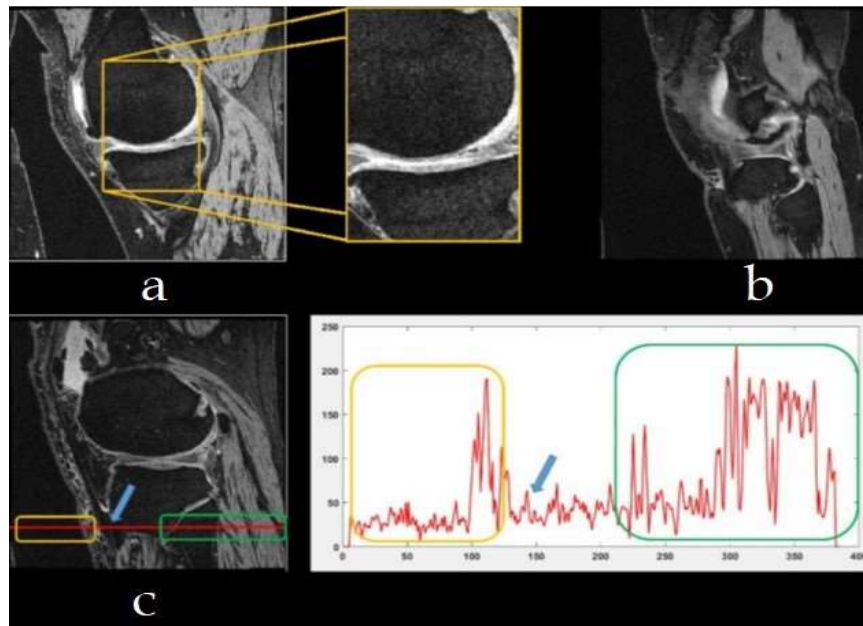


Figure 3.1. Challenges in MR images (a) Noise present, (b) complex structure of knee, (c) inadequate contrast of knee MR image.

### 3.2 Introduction

Chronic diseases are generally defined as long lasting disease with limitations to day-to-day activities. Common talk about chronic disease refers to cancer, heart disease, and diabetes. On contrary, there is no such alertness about arthritis disease and its leading cause of mobility and mortality around the globe. Arthritis is the swelling and tenderness of one or more joints causing inflammation, stiffness, and pain. Arthritis disease is of different types (i) Osteoarthritis (OA), (ii) Rheumatoid arthritis (RA), (iii) Gout (iv) Juvenile arthritis (JA), (v) Spondyloarthropathies (vi) Reactive and infectious arthritis (IA)[151]. Osteoarthritis is a kind of degenerative arthritis that breaks down the joints causing inflammation, bone injury, and pain. This type of arthritis is caused by wear and tear/ damage of cartilage and joints. Rheumatoid

arthritis is caused by lining of joints, tough membrane causing swollen and inflammation of joints with destroying cartilage and bone joints. RA affects hands, arms, knee making it difficult for daily tasks. Juvenile arthritis (JA) mostly affects the children causing autoimmune disorder. JA causes joints to misalign, muscle and tissues to tighten, bones to erode, swelling, and stiffness. Spondyloarthropathies attacks the tendons and ligaments attached to spine and pelvis bones. SA causes spinal deformity and arm and knee instability. Reactive and infectious arthritis (IA) is an infection of joint causing pain and swelling. This type of arthritis is caused by bacteria, viruses, or parasites. IA when causes infection in one part of body triggers dysfunction of immune system. Gout is a chronic autoimmune disease induced by urinary crystal buildup in the tissues. Gout causes big toe and potential affects other joints with swelling, and redness.

Medical interpretations from clinical and laboratory data are highly demanded for arthritis diagnosis. Analyzing these medical records or images are complex due to fuzziness present in it. Fuzziness may be in terms of noise, and artifacts that causes difficult for processing of images. Moreover, accurate diagnosis is not guaranteed as human experts are prone to errors due to abundant clinical workload, and other health issues. In recent years, intelligent medical diagnostic system (IMDS) has been widely used in hospitals for assisting experts in analyzing the patients' health. For experimentation and learning medical images are stored in large datacenters, created with the use of useful resources. Intelligent systems are applied on these images for providing information for diagnosing the diseases. Each intelligent system has unique steps for processing the data and producing distinct outcomes. However, the primary step in image processing is pre-processing when thereis raw data or primary data. Pre-processing is a stage of reducing or removing the raw data such as noise, and irregularities (artifacts) in the image. During these past few years, a broad variety of preparatory procedures for MR pictures to improve the quality of MR images were created. Most methods come from the non-local mean filter (NLM) [76] to estimate their comparable patches in the search window by weighted average, in the current pixel. One of the critical drawbacks of NLM filter is time consuming. NLM has been explored extensively in several forms to improve the problem of MR denoising.

Specifically, the optimized block-wise version of NLM (ONLM) reduces computational complexity. In addition, other state-of-the-art techniques such as block-matching and 3D (BM3D) combines nonlocality and domain transform using DCT for estimating multiple arrogates at each location. An improved version of BM3D has been introduced, BM4D for processing of volumetric data and adapting analytical transforms.

In recent years, deep learning has made tremendous impact on image processing field. In addition, deep learning is being implemented for low-level tasks, like denoise, deblurring and contrast improvement, except for comprehensive study on high-level tasks. The multilayered sensing, autoencoders and neural nets were used for image restore and outcomes were achieved which are commensurate with advanced techniques. However, to the best of our understanding, MR image denoising research seems to be quite restricted as represented in [4]. Despite significant study into MR image de-noising, approaches still suffer from a number of shortcomings like computational complexity, enhancement and parameter estimation.

The original MR images are associated with the noise in the form of speckles and insufficient contrast of tissues causing difficulties in segmentation and diagnosis of tissues. Thus, preprocessing of MR images like noise reduction is performed using the Sparse aware noise reduction with Convolutional neural network (SANR\_CNN) approach [149]. The denoising approach should filter the noise present in the MR images with affecting the essential information such as edges, contrast, brightness, etc. Many techniques have been proposed but fail to preserve the image information. Thus, the image details are preserved using proposed SANR\_CNN technique for further process.

### **3.2.1 Noise Distribution**

In general, Gaussian noise degrades medical MR pictures, which are simple to deal with and are signal dependent. The visual quality and quantitative features are impeded by the noise. The Gaussian noise disrupts the gray value in medical MR images, the distribution function is shown in equation 3.1.

$$P(G) = \frac{1}{\sigma\sqrt{2\pi}} - e^{-\frac{(i-\mu)^2}{2\sigma^2}} \quad (3.1)$$

where,  $i$  is gray intensity,  $\sigma$  is standard deviation,  $\mu$  is average value. The Rician noise is represented as in equation 3.2.

$$R(n) = Y_i + Y_o \quad (3.2)$$

Where,  $Y_i$ , and  $Y_o$ , are imaginary and original values.

$$Y_i = I \cos \theta + \omega_1 \quad (3.3)$$

$$Y_o = I \sin \theta + \omega_2 \quad (3.4)$$

### 3.3 Preprocessing of Knee MR Images

The proposed methodology SANR\_CNN is divided into subsequent stages: (i) Dictionary creation stage, (ii) fusing the sparse data with dictionary phase, and (iii) parametric restoration of MR image. The CNN architecture includes several specific hidden layers with scarce characteristics to generate images of high quality. The CNN design relies primarily on image interpretation based on past expertise and appropriate noise training. As seen in Figure 3,2 the image is partitioned into chunks by the window technique.

The proposed CNN architecture as illustrated in figure 3.3 estimates the weights for each layer obtained and creates a dictionary by storing them for further processing. During testing of the model these generated dictionary values are applied, to enhance the model and increase the performance. The model reconstructs the input image into high-quality and denoised MR image. There are two benefits to the suggested CNN architecture: (i) local reliance, and ii) variability of scale. Local dependency indicates that the information may be linked to the information around the point at the present moment. Variability of scale indicates that in the magnitude, recurrence, and synchronization the study item does not vary. The CNN was set with initial parameters of learning rate  $1 \times 10^{-3}$ , epsilon  $1 \times 10^{-8}$ .

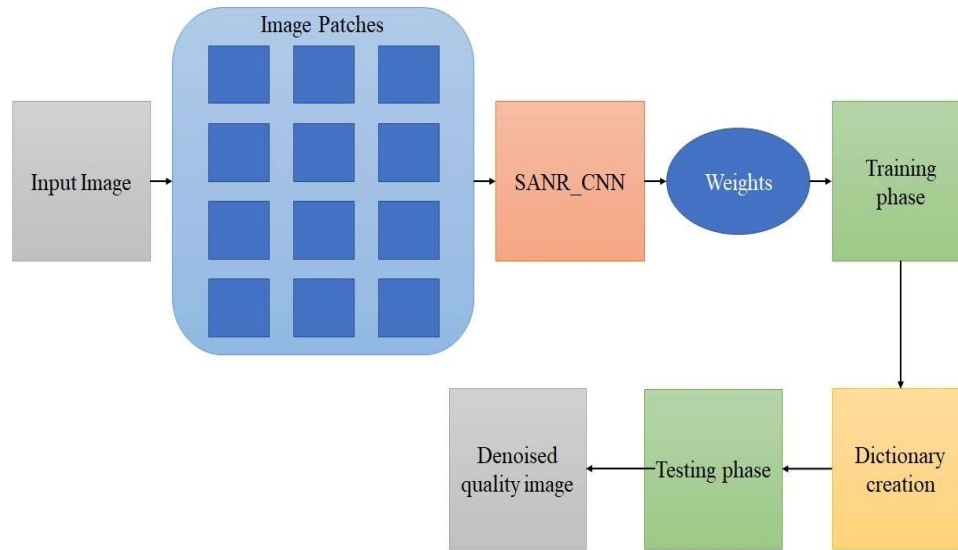


Figure 3.2. Proposed Sparse aware noise removal with Convolutional neural network (SANR\_CNN) architecture.

### 3.3.1 Denoising of Knee MR Image using SANR\_CNN

The proposed Convolutional neural network (CNN) architecture consists of 17 layers with different layers such as: convolutional layer, Rectified linear unit (ReLU), and dilated convolutional network layer. The 1<sup>st</sup> and 16<sup>th</sup> layer of the architecture are convolutional and ReLU combined. The second, fifth, ninth, and twelfth layers are dilated convolutional layers, with the last layer functioning as a convolutional layer. The kernel size of 128 X 1 X 40 X 40 for first and final layer and 128 X 64 X 40 X 40 for other remaining layers.

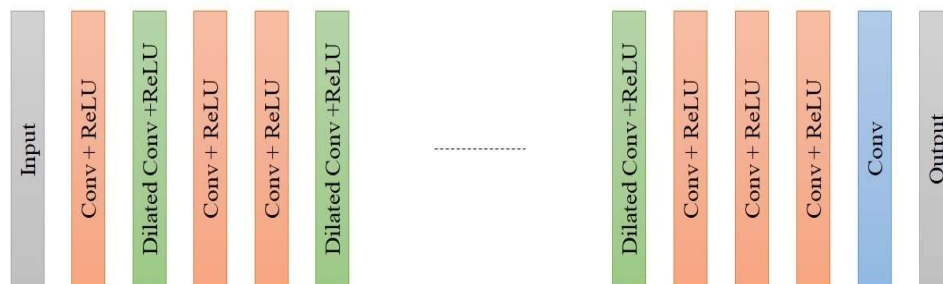


Figure 3.3. Proposed Dilated convolutional neural networks architecture

In classic CNN design, the pooling procedure can provide the kernels a bigger appropriate field. Extensive aggregating procedures, on the other hand, eventually result in additional information loss. As a result, the dilated convolution operation extends the corresponding field without aggregating, providing every other convolution to hold a diverse range of information. The dilated convolution layer is a discrepancy on the standard convolutional procedure. The basic idea behind dilated convolutional is to provide a constant factor 0 that would not change throughout the process of learning amongst kernel and accomplish the goal of dilating the relevant field without increase in the number of factors associated. The dilation rate with one-dimensional convolution is denoted by equation 3.5, wherein  $x(i)$  and  $z(i)$  indicate the input and output signals, correspondingly, 'y' signifies the size of the convolutional kernel, and 'd' is the dilatation rate. In equation 3.6,  $d$  is the dilation factor,  $1 * K$ , represent convolution kernel.

$$z(i) = \sum_i^n x(i + dy)w(y) \quad (3.5)$$

$$K(d) = K + (k - 1)(d - 1) \quad (3.6)$$

### 3.3.2 Dictionary Learning

In recent years the convolutional dictionary learning has been aroused as better learning approach[152][153]. The approach is an enhancement of conventional dictionary learning, with the goal of capturing the essential features of image data and increasing feature classification ability. Convolutional dictionary learning adheres to CNN's design yet employs a hierarchical approach. In dictionary learning, the convolutional correlates to the independent variables in this study stages. Let  $\{D_n\}_{n=1}^N$  be N-layer convolutional dictionary, with  $D_n \in R^{d \times K_n}$  is the dictionary in the n-th layer dictionary and  $K_n$ , being the value of  $D_n$ . The convolutional representation may be written as  $Z \approx D_1 D_2 \dots D_N A_N$ . The composition can be expressed in depth as shown in equation 3.7.

$$Z \approx D_1 A_1, Z \approx D_1 D_2 A_2, Z \approx D_1 D_2 D_3 A_3, \dots Z \approx D_1 D_2 \dots D_N A_N \quad (3.7)$$

The dictionary learning method is performed to optimize the denoising approach for knee MR images. Let ‘n’ be the noise blended with input image indicated by patch intensity ‘i’ as given in the equation 3.8.

$$Y = i + k \quad (3.8)$$

Each patch is measured as  $m \times m$ , with ‘k’ value ranging from 8 to 12 pixels. All these patches are integrated together inside a frame to reconstruct the image. As an initiation procedure, the feature component ranges are supplied, and a sparse linear technique is applied to eliminate noise all chaotic patches obtained from the medical image. As demonstrated in equation 3.6, the noisy error can be minimized by designating with a pre-defined factor ( $\epsilon$ ) and Y as a noisy patch.

$$\min \|\alpha\|_0 \text{ s.t. } \|D_\alpha - Y\|_2 \leq \epsilon \quad (3.9)$$

The pseudo normalization parameter is used to impose sparsity characteristics ( $l_0$ ). However, the normalization problem cannot be solved using pseudo parameter. So, epsilon ( $\epsilon$ ) was chosen for better approximation of normalization error defined by its variance. As stated in equation 3.10, dictionary learning may be split into rows and columns using a fitness function. The dictionary can be updated using the equation 3.11, with Z denoting the weighted sparse factor and  $D_i$ , signifies the dictionary.

$$D(j) = XZ_i^T \|XZ_j^T\|_2 \quad (3.10)$$

$$D_i = \min \|X - D_i Z\|_f^2, d_j \|_2 \leq 1 \quad (3.11)$$

---

**Algorithm:** Creation and Updating the dictionary

---

**Input**

A training subclass from category  $i$ , the factors  $Z_i$ , the dictionary  $D_i$

Let  $Z_i = [Z_1, Z_2, \dots, Z_n]$  and  $D_i = [d_1, d_2, \dots, d_n]$  where  $i = 1, 2, \dots, n$ ,  $i^{\text{th}}$  is the row vector of  $Z_i$  and  $j^{\text{th}}$  is the column vector of  $D_i$

**for**  $j=1$  **to**  $n$  **do**

Fix all  $d_i, i \neq j$ , and update  $d_j$ . Let X be the minimization function

---



---

Place equation 3.8 here,

By solving this objective function

Place equation 3.9 here,

**End for**

**Output**

Update of dictionary (equation 3.10)

---

### 3.4 Results and Discussion

The knee dataset obtained from local hospital and from Osteoarthritis Initiative (OAI) was used in this experimental study. Investigations were performed out on several MR Image datasets to illustrate the applicability of the suggested method. Additionally, quantitative analysis was used to assess the effectiveness of the denoising approach. Peak signal to noise ratio (PSNR), structural similarity index (SSIM), mean squared error (MSE), and enhancement measure (EM) were used in quantitative research, as indicated in formulas 1.1, 1.2, 1.3, 1.4, and 1.5. The suggested approach's performance characteristics were evaluated with those of the conventional and most extensively used approaches.

The details of knee MR image dataset are given in the section 1.2. The aforementioned denoising method was trained on 12000 pictures of 512 X 512 resolution. T1-weighted images totaled 5600, T2-weighted images were 3800, and Flair images totaled 2600. The dataset includes of three different kinds of MR images (i) T1-weighted with TE of 9.7 and TR of 760.0, (ii) T2-weighted with TE of 34.7 and TR of 2740.0, and (iii) Flair images with TE of 104.9 and TR of 3360.0. Table 3.1 describes the quantitative parameters with trials for proposed model. The table demonstrates an average PSNR value of 41dB and 0.87 as SSIM value. Many trials are carried out for obtaining better quantitative values. The comparative techniques used in the experiment are Block Matching 3D Denoising (BM3D), Trainable Nonlinear Reaction Diffusion (TNRD), Denoising Convolutional Neural Network (DnCNN), Convolutional Neural Network with joint loss function (MP-DCNN) and

proposed Sparse Aware Noise Reduction with Convolutional Neural Network (SANR\_CNN). For obtaining better results the experiment was conducted with many trials. But for illustration just 7 trials are described. Table 3.6 describes the computational time or execution time required to process the knee MR images. As computational time is the major issue with image processing, the proposed approach utilizes the time efficiently by creation of dictionary learning concept and reducing the testing time.

Table 3.1. Quantitative parameters with trials

<i>Parameter</i>	<i>Trial</i>	<i>Trial</i>	<i>Trial</i>	<i>Trial</i>	<i>Trial</i>	<i>Trial</i>	<i>Trial</i>	<i>Summary</i>
	<i>run 1</i>	<i>run 2</i>	<i>run 3</i>	<i>run 4</i>	<i>run 5</i>	<i>run 6</i>	<i>run 7</i>	
<i>PSNR</i> <i>(dB)</i>	40.59	41.72	40.17	43.81	42.92	41.23	41.58	41 ± 3.00
<i>SSIM</i>	0.81	0.92	0.86	0.90	0.87	0.89	0.92	0.87 ± 0.08
<i>MSE</i>	0.005	0.003	0.004	0.006	0.006	0.005	0.005	0.004 ± 0.002
<i>EM</i>	55.13	58.78	58.56	61.63	62.79	60.10	61.95	59.84 ± 3.00

Table 3.2. Comparative analysis of PSNR value.

<i>Techniques</i>	<i>Trial</i>	<i>Trial</i>	<i>Trial</i>	<i>Trial</i>	<i>Trial</i>	<i>Trial</i>	<i>Trial</i>	<i>Summary</i>
	<i>run 1</i>	<i>run 2</i>	<i>run 3</i>	<i>run 4</i>	<i>run 5</i>	<i>run 6</i>	<i>run 7</i>	
<i>BM3D</i>	19.21	19.23	19.11	19.23	19.26	19.09	19.27	19 ± 0.30
<i>TNRD</i>	23.45	25.81	24.15	24.68	23.86	23.94	24.79	24 ± 3.00
<i>DnCNN</i>	29.92	32.43	30.52	31.12	32.71	31.01	32.30	31 ± 2.00
<i>MP-DCNN</i>	17.51	20.72	18.53	18.51	19.56	20.76	20.85	19 ± 3.00
<i>SANR_CNN</i>	40.59	41.72	40.17	43.81	42.92	41.23	41.58	41 ± 3.00

Table 3.3. Comparative analysis of SSIM value.

<i>Techniques</i>	<i>Trial run 1</i>	<i>Trial run 2</i>	<i>Trial run 3</i>	<i>Trial run 4</i>	<i>Trial run 5</i>	<i>Trial run 6</i>	<i>Trial run 7</i>	<i>Summary</i>
<i>BM3D</i>	0.64	0.68	0.63	0.68	0.69	0.63	0.65	0.65 ± 0.05
<i>TNRD</i>	0.59	0.54	0.58	0.60	0.56	0.58	0.59	0.57 ± 0.05
<i>DnCNN</i>	0.78	0.79	0.74	0.76	0.73	0.76	0.77	0.75 ± 0.7
<i>MP-DCNN</i>	0.67	0.63	0.64	0.66	0.69	0.62	0.65	0.65 ± 0.05
<i>SANR_CNN</i>	0.81	0.92	0.86	0.90	0.87	0.89	0.92	0.87 ± 0.08

Table 3.4. Comparative analysis of MSE value

<i>Techniques</i>	<i>Trial run 1</i>	<i>Trial run 2</i>	<i>Trial run 3</i>	<i>Trial run 4</i>	<i>Trial run 5</i>	<i>Trial run 6</i>	<i>Trial run 7</i>	<i>Summary</i>
<i>BM3D</i>	0.015	0.015	0.013	0.015	0.015	0.012	0.015	0.014 ± 0.003
<i>TNRD</i>	0.003	0.003	0.003	0.003	0.003	0.003	0.003	0.003 ± 0.001
<i>DnCNN</i>	0.01	0.01	0.01	0.01	0.01	0.01	0.01	0.01 ± 0.003
<i>MP-DCNN</i>	0.02	0.02	0.02	0.02	0.02	0.02	0.02	0.02 ± 0.001
<i>SANR_CNN</i>	0.005	0.003	0.004	0.006	0.006	0.005	0.005	0.004 ± 0.002

Table 3.5. Comparative analysis of EM value

<i>Techniques</i>	<i>Trial run 1</i>	<i>Trial run 2</i>	<i>Trial run 3</i>	<i>Trial run 4</i>	<i>Trial run 5</i>	<i>Trial run 6</i>	<i>Trial run 7</i>	<i>Summary</i>
<i>BM3D</i>	21.98	22.07	22.05	22.27	23.10	24.20	24.25	22.84 ± 2.00
<i>TNRD</i>	30.92	32.24	31.66	32.30	33.66	33.81	33.67	32.60 ± 1.70
<i>DnCNN</i>	33.29	33.77	33.90	34.38	35.54	34.92	35.98	34.54 ± 1.80
<i>MP-DCNN</i>	39.23	41.55	41.92	41.12	43.06	44.18	44.72	42.25 ± 2.00
<i>SANR_CNN</i>	55.13	58.78	58.56	61.63	62.79	60.10	61.95	59.84 ± 3.00

Table 3.6. Computational time for different techniques

<i>Techniques</i>	<i>Time(sec)</i>
<i>BM3D</i> [154]	835.12
<i>TNRD</i> [155]	792.53
<i>DnCNN</i> [156]	654.09
<i>MP-DCNN</i> [157]	631.31
<i>SANR_CNN</i>	567.77

The experiment was conducted on T1, T2, and Flair MR images. Table 3.2 shows the PSNR value with seven different trails. The proposed SANR\_CNN model produces outstanding result with PSNR value of 42.92dB in trial 5. The average PSNR for all 7 trials is 41dB and the nearest value with DnCNN on trial 7 is 32.30dB. The results obtained in table 3.3 provides the SSIM values, that shows the similarity of image structure. For proposed technique 0.92 value was obtained for trial 2 and trial 7, and average value of 0.87. The SSIM values shows the edge contents and details of knee

MR images are preserved. This value restoration aids post-processing operations such as MR dimensionality reduction, feature extraction, and classifications.

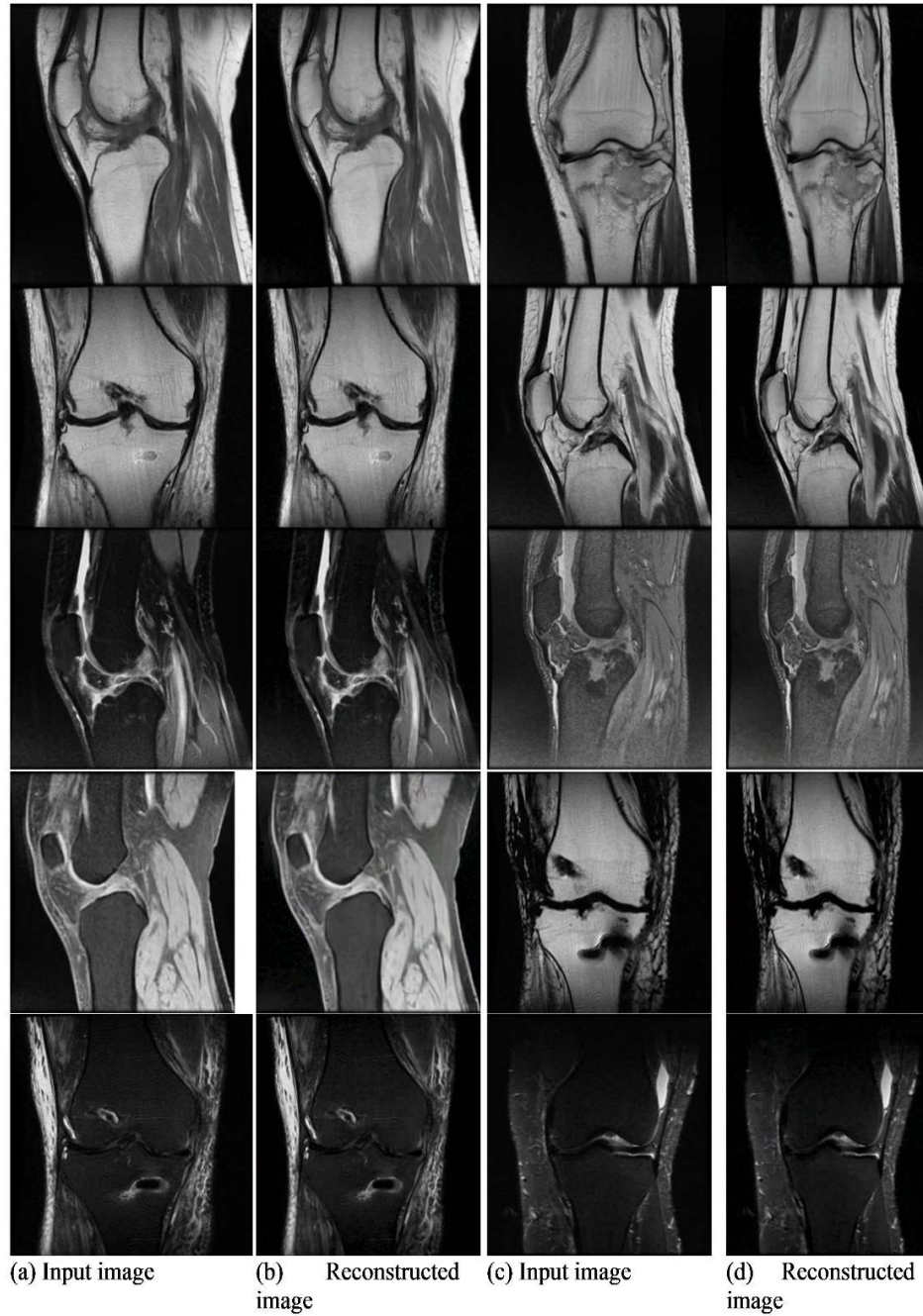


Figure 3.4. Denoised Knee MR images achieved with SANR\_CNN.

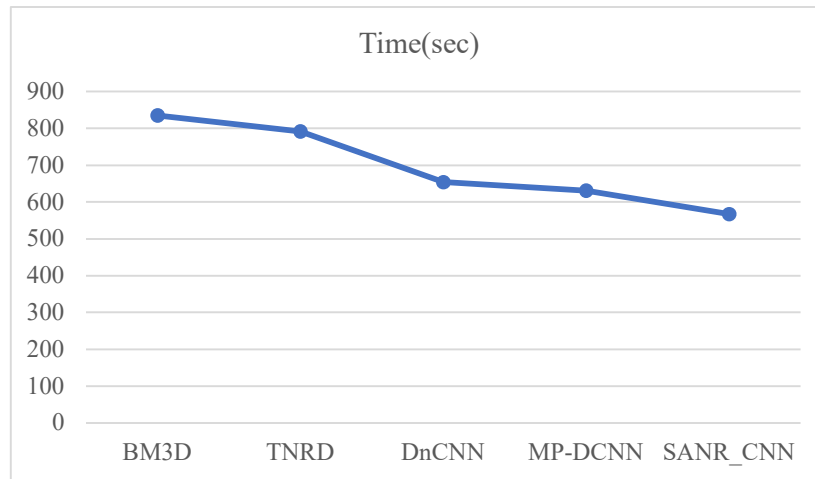


Figure 3.5. Computational time estimated for comparative techniques.

Figure 3.4 illustrates the input images and denoised images. In table 3.4 the mean squared error (MSE) value for proposed technique obtained was 0.005. The TNRD also for some good result for MSE value. Table 3.5 describes the enhancement measure (EM) obtained for comparative techniques. The EM obtained for proposed SANR\_CNN technique was 59.84 on average trials. Comparatively with proposed technique, MP-DCNN technique also performs better in conditions of different considerations. Figure 3.4 shows the comparative analysis of computational time taken for execution of proposed and similar techniques. From the figure 3.5 it can be visualized that the computational time of proposed technique is lesser than the similar compared techniques.

### 3.5 Conclusion

Implementation of these intelligent medical diagnostic system (IMDS) has contributed to major transformation in the field of information retrieval and processing. The IMDS with proper decision making can be helpful in diagnosing the chronic disease such as rheumatoid arthritis. As a part of constant effort of making knee arthritis diagnosis, preprocessing is an important phase, as the MR images are affected to noise artifacts during image acquisition. So, in this chapter a new denoising technique for knee MR images is proposed. Inadequate contrast and noise are issues in MR images that cause ineffective segmentation and classification outcomes. Denoising obtained by proposed dictionary CNN approach reduces the

noise artifacts present in the knee MR images. The dictionary approach with CNN exceptionally reduces the computational time required for testing phase.

The outcomes of the experiment conducted shows capability of SANR\_CNN over other compared methods. The new denoising technique helps to resolve erroneous and inappropriate MR data. The improved knee MR images may be utilized to segment hard tissues such as joints and give a significant increase in classifications.

## Chapter 4

### Hybrid Architecture for Knee MR Image Segmentation and Feature Extraction

This chapter presents the proposed hybrid architecture of discrete wavelet transform (DWT) and MultiResUNet. The following is how the chapter is structured: Section 4.1 introduces segmentation and feature extraction techniques, Section 4.2 discusses seed point selection approach and bone area retrieval utilizing the suggested MultiResUNet architecture, Section 4.3 demonstrates performance assessment and discussion, and Section 4.4 closes the chapter.

#### 4.1 Introduction

Segmentation and feature extraction in knee MR images are challenging task that involves challenges like complicated knee structure, MR image artifacts, partial volume effect, varying intensity level, etc., as discussed in section 2.2. Many approaches are shown in the review to autonomously slice the ROI and extraction of features from MR images, but they all have drawbacks, as mentioned in the review. The majority of existing approaches are training-based, model-based, or atlas-based, requiring large datasets, model, and atlas development. Slight variation in the training data, model or atlas demand the retraining of entire system otherwise it affects whole system outcome. Even the model training and designing phase requires huge time and manual efforts of experts to annotate training data and designing the model. This increases inter and interobservers inconsistency, which has a significant impact on the performance of morphological operations and extraction approaches.

Thus, in this research a new model automatic multi-stage architecture is proposed for segmentation and feature extraction. Figure 4.1 illustrates the different sagittal views of knee MR image, and it can be observed that the femur, and tibia bones occupy major portion of MR image. Tables 2.2 and 2.3 indicate that the computational approaches for segmentation seem to be either automated or semi-automatic. Whereas semi-automatic approaches produce effective outcome, but are limited by manual intervention, which could lead to dependability issues. The fully automatic methods



had gained lot of attraction and are either supervised or unsupervised. These approaches yielded substantial findings, but they resulted in varied intra and inter-observer unpredictability, resulting in divergent conclusions amongst experts working with the same dataset.

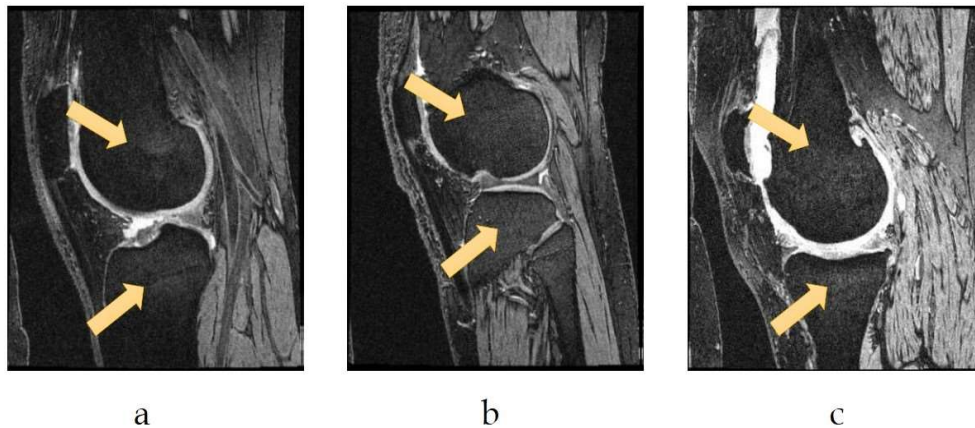


Figure 4.1. Different views of knee MR image (Sagittal view)

Thus, to address the issues related to segmentation and feature extraction, a fully automatic technique is proposed in this work. Bone segmentation is obtained in two stages such as initial bone region extraction, that extracts the bone regions but with boundary loss because of weak tissues. The bone region extraction is performed with MultiResUNet architecture followed by boundary correction. Second stage involves post processing with masking the tissue structure surrounded by femur and tibia bones. As shown in figure 4.2 the multi-level architecture proposed for segmentation and feature extraction is followed in three stages: pre-processing, region of interest extraction, and post-processing. The developed framework initially takes input as stacked sequences of knee MR images. Next, in first stage the noise and contrast issues are resolved by applying proposed SANR\_CNN approach.

Using the proposed MultiResUNet architecture, the preprocessed knee medical images are then utilized to identify seed point selection. The seed point initializes the bone region extraction stage. The boundary leakages and corrections are applied after segmenting the bones from knee MR images. Finally, the required feature set are extracted from knee MR images using discrete wavelet transform, and further which

will help for classification of knee MR images. A detailed discussion is presented in subsequent sections.

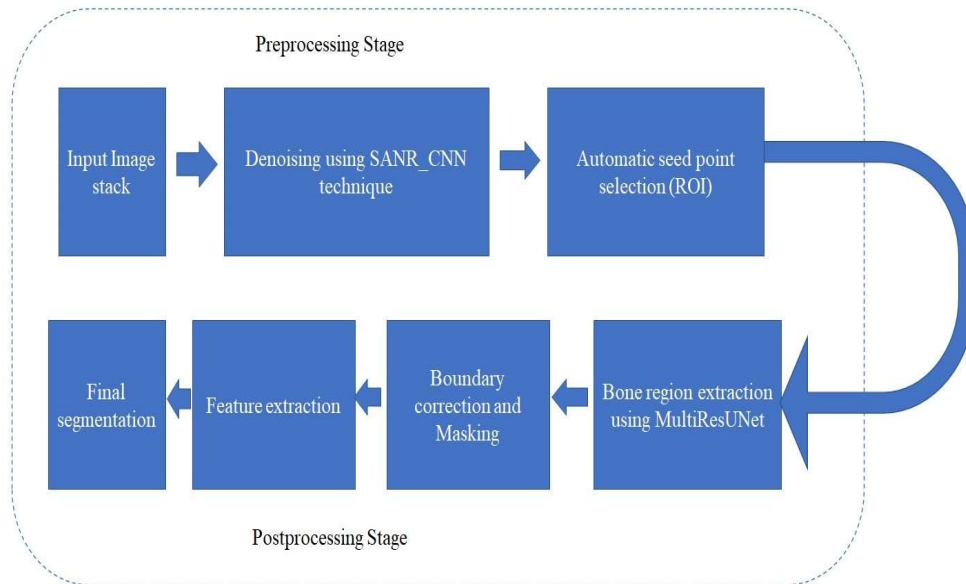


Figure 4.2. Multi-level architecture for automatic segmentation and feature extraction

## 4.2 Methodology

The MR images are prone to noise that are introduced during image acquisition process. These images cause difficulties in segmentation and feature extraction and further classification. As a result, there is a requirement to filter away noise in MR images, which enhances subsequent algorithm development. In this research SANR\_CNN filtering is used as denoising technique that reduces the interference in knee MR images and preserves the image features such as edges, and intensity level. The detailed discussion about SANR\_CNN is done in earlier section 3.3.

To acquire the seed points autonomously, the middle 25% of the data slices are analyzed, i.e., given a sequence of 160 slices, 61-100 are chosen depending on actual positioning inside the image stack. The centre is chosen due to the obvious defined and maximum bone area in those slices, as described in figure 4.3. Edge detection is used on transitional slices, and images are layered on top of one another. Determining the azimuth and elevation, image intensity characteristics in 3D generated from multi-edge overlapped slices identifies the region with low edge intensity. As shown in

figure 4.3 (b), the deepest and vertical intensity profile with local valleys are selected to recognize the seed points in femoral and tibial tissues.

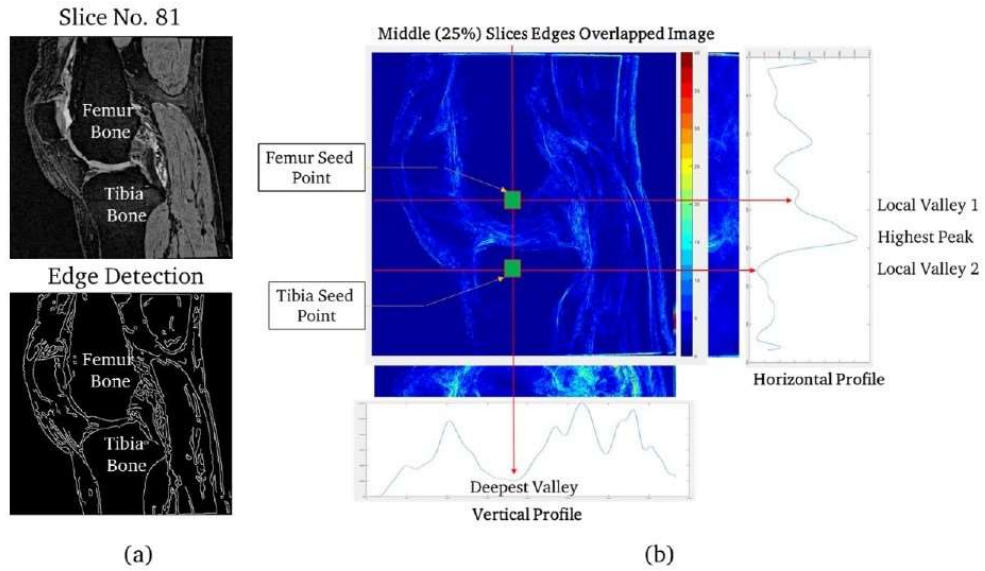


Figure 4.3. (a) MR Slice number 81 with edge recognition (b) Seed point detection.

#### 4.2.1 Discrete-MultiResUNet Architecture

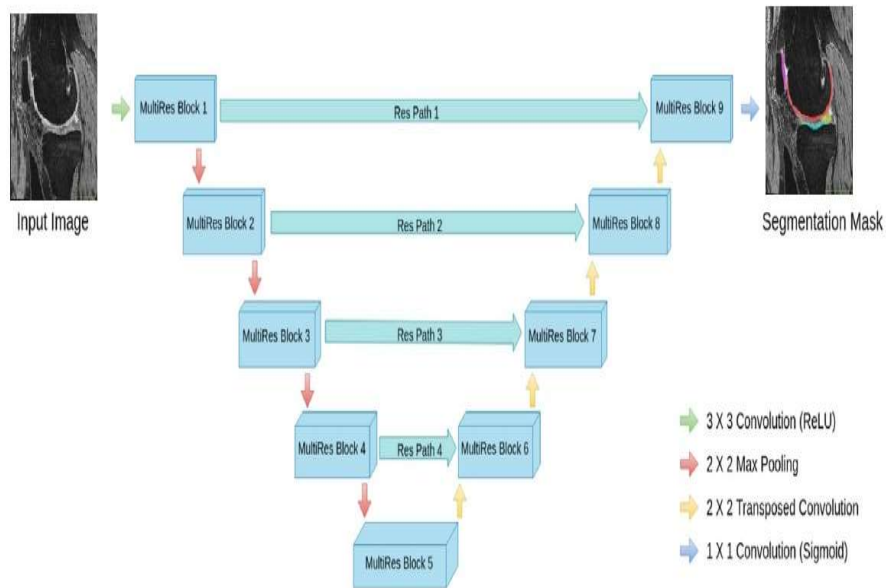


Figure 4.4. Proposed segmentation architecture

The suggested MultiResUNet architecture improves on U-Net in order to execute segmentation tasks properly. The design is adapted to the assigned task, including 3 x 3 convolution layer, a 2 X 2 maximum pooling procedure, a 2 X 2 transposed convolution, and a 1 X 1 sigmoid activation function. The model convolution is equipped with a rectifier linear unit to ensure the effectiveness of the segmentation job (ReLU). The wavelet transform is used to provide spatial support during the feature extraction process. To evaluate the image's characteristics, the segmented image is split into sub-bands. Despite previous methods, wavelet transformations allow for signal time-frequency localization.

#### **4.2.2 Initialization of Bone Region Extraction**

The first bone segments belonging to the femur and tibia are retrieved through using MultiResUNet architecture, which includes automated seed point determination. The seed points generated from the 3D overlapped technique are first utilized to build an appropriate level in MultiResUNet, which develops across the femur and tibia bone areas and retrieves initial bone sections from the MR image. After that, the bone areas are extended further to identify geometrical coordinates. The coordinates found is then utilized to initialize the subsequent slices. This method is repeated for the entire dataset, and geometrical coordinates are updated for every slice taken from the femur and tibia bone areas. If the thresholding goes below a specific level, the algorithm ends the bone region's initialization procedure. Figure 4.5 depicts roughly 40 bone-free slices at the commencement and conclusion of the slice series. When the region of the femur and tibia bone slices becomes less than 100 pixels, the procedure immediately ends.

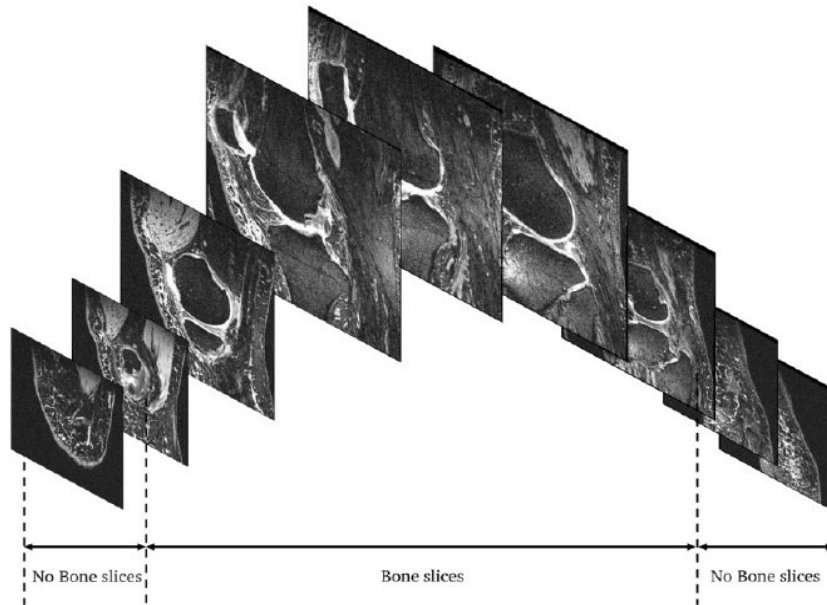


Figure 4.5. Slices consisting of bone and no-bone regions.

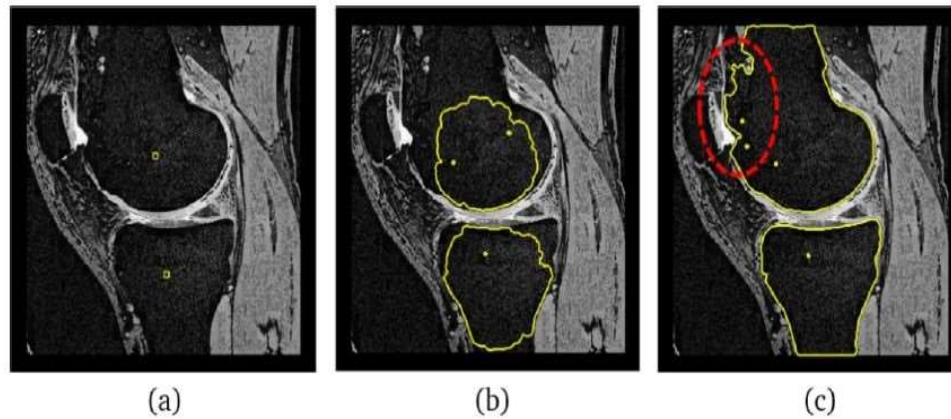


Figure 4.6. Bone region extraction (a) Seed selection, (b) Intermediate stage, (c) Final stage of bone region extraction.

Figure 4.6 depicts the extraction of a bone area using an automated seed selection technique. Other tissues, in addition to bone areas, are retrieved in this illustration. These other tissues are corrected or removed during post processing process. Once the bone region is corrected then the remaining region is masked to obtain the joint space narrowing (JSN) between femur and tibia.

### 4.2.3 Boundary Leakage Correction

Point-to-point endpoints are calculated by calculating the distance between both the present and subsequent endpoints in two successive slices. The variation in bone tissue architecture is quite tiny and changes gradually. Distances that exceed a predetermined threshold are labeled as leakages, and they are rectified by moving the points corresponding to the outliers from the neighboring border. The proposed boundary correction is provided in following equations. The current boundary coordinates ( $B_{cur}$ ), and adjacent boundary coordinates ( $B_{adj}$ ) are shown as follows in equation 4.1 and 4.2.

$$B_{cur} = \{x, y | (x_i, y_i), i = 1: N\} \quad (4.1)$$

$$B_{adj} = \{x, y | (x_i, y_i), j = 1: M\} \quad (4.2)$$

where  $x, y$  are the bone's coefficient vectors and  $M, N$  are the number of cartesian coordinates in the neighboring and contemporary boundaries, appropriately. To calculate the point-to-point proximity, the number of data points in each dataset is equalized utilizing normal approximation. As indicated in equation 4.3, the distance amongst consecutive slice boundaries is calculated using Euclidean distance.

$$E(dist) = dist(B_{cur}, B_{adj}) = \sqrt{(Y_{cur} - Y_{adj})^2 + (X_{cur} - X_{adj})^2} \quad (4.3)$$

The present and neighboring boundaries are identified as set outlier's points based on the point-to-point distance computed utilizing equation 4.3, ( $P(cur)_o, P(adj)_o$ ), and non-outlier's points ( $P(cur)_{no}, P(adj)_{no}$ ).

$$P(cur)_o = \{x, y | B_{cur}(X_i, Y_i), if dist > \tau\} \quad (4.4)$$

$$P(adj)_o = \{x, y | B_{adj}(X_i, Y_i), if dist > \tau\} \quad (4.5)$$

$$P(cur)_{no} = \{x, y | B_{cur}(X_i, Y_i), if dist \leq \tau\} \quad (4.6)$$

$$P(adj)_{no} = \{x, y | B_{adj}(X_i, Y_i), if dist \leq \tau\} \quad (4.7)$$

where, threshold distance is denoted with  $\tau$ . If the Euclidean distance exceeds this preset criterion, the points are classed as outliers; otherwise, they are labelled as non-outliers. After identifying specific locations, the border is adjusted by moving the

points pertaining to the outliers from the neighboring and contemporary contours. This is quantitatively expressed by equations 4.8 and 4.9, wherein  $x(dis)$  and  $y(dis)$  are displacement position information from the neighboring boundaries and  $d(dis)$  is the averaged displaced distance from the neighboring to the contemporary contour, as indicated in equation 4.10.

$$x(dis) = x + \frac{d_{dis}}{\sqrt{1+m(i)^2}} \quad (4.8)$$

$$y(dis) = y + \frac{d_{dis}}{\sqrt{1+m(i)^2}} \quad (4.9)$$

$$d(dis) = \mu(dist(p(cur)_{no}, P(adj)_{no})) \quad (4.10)$$

In equation 4.10 the  $dist(p(cur)_{no}, P(adj)_{no})$ , is estimated as shown in equation 4.3. The set of displaced point coordinates are given by the equation 4.11.

$$P_{no}^{dis}(i) = P_{no}^{adj}(i) + d(dis) = \{x, y | x_{dis}(i), y_{dis}(i)\} \quad (4.11)$$

The corrected boundary coordinates ( $B_{cur}$ ) corresponding to non-outlier set of points is shown in equation 4.12 and 4.13.

$$P(corr) = [P_o^{cur}, P_{no}^{dis}] \quad (4.12)$$

$$B'_{cur} = \{x, y | P(corr)(x, y)\} \quad (4.13)$$

If the outlier points set is non-empty, boundary adjustment is necessary; alternatively, the adjusted boundary parameters are the same as existing boundary parameters. The boundary correction algorithm is illustrated in algorithm 1. Thus, the new corrected coordinates serve same as adjacent boundary coordinates and this process is repeated until all boundary parameters in the dataset have been adjusted. The equation 4.14, and 4.15 shows the current adjacent reference values estimated to boundary coordinates.

$$If, P(cur)_o = \emptyset \quad (4.14)$$

Then,

$$B'_{cur} = B_{cur} \quad (4.15)$$

**Algorithm 1.** Boundary Correction and displacement**Input:** MR slices**Output:** Boundary corrected and masked MR slice

1. Determine the set of boundary parameters for an MR slice.
2. Interpolate the points to make equal slices.
3. Using equation 4.3, calculate the point-to-point distance between the two coordinates.
4. Applying equations (4.4, 4.5, 4.6, 4.7), categorize points as outlier or non-outliers.
5. If the outlier points are set as null ( $P(cur)_o = \emptyset$ ), then go to step 8, else go to step 5.
6. Using equations (4.10, 4.11), reposition the endpoints in the slice that corresponds to the outlier by  $d(dis)$ .
7. Applying equation 4.15, incorporate the relocated endpoints from the slice with the non-outlier set of endpoints.
8. Populate in any boundary gap that exists to obtain a final adjusted contour.
9. Repeating steps 1–7 to adjust the boundaries all throughout dataset.

**4.2.4 Feature Extraction using DWT**

The proposed architecture uses discrete wavelet transforms (DWT) for extracting the features from segmented image. Higher - level wavelet coefficients are adjusted, and the continuous wavelet transformation  $f(x)$  and real – valued discrete wavelet function  $f(x)$  are used  $\Psi(x)$ , is described in equation 4.1. In equation the scaled and transition parameters are represented as  $s$  and  $t$  respectively. The wavelet function  $\Psi_{s,t}(x)$  is generated from  $\Psi(\cdot)$ , by constraining  $s$  and  $t$  to a discrete lattice with  $s=2^j$  and  $t=2^j k$ , and as illustrated in equation 4.18.

$$W_{\Psi}(s, t) = \int_{-\infty}^{\infty} f(x) \Psi_{s,t}(x) dx \quad (4.16)$$



where,

$$\Psi_{s,t}(x) = \frac{1}{\sqrt{s}} \Psi\left(\frac{x-t}{s}\right); s \in \mathfrak{R}, t \in \mathfrak{R} \quad (4.17)$$

$$DWT_{f(n)} = \begin{cases} A_{j,k}(n) = \sum_n f(n) G_j^*(n - 2^j k) \\ D_{j,k}(n) = \sum_n f(n) H_j^*(n - 2^j k) \end{cases} \quad (4.18)$$

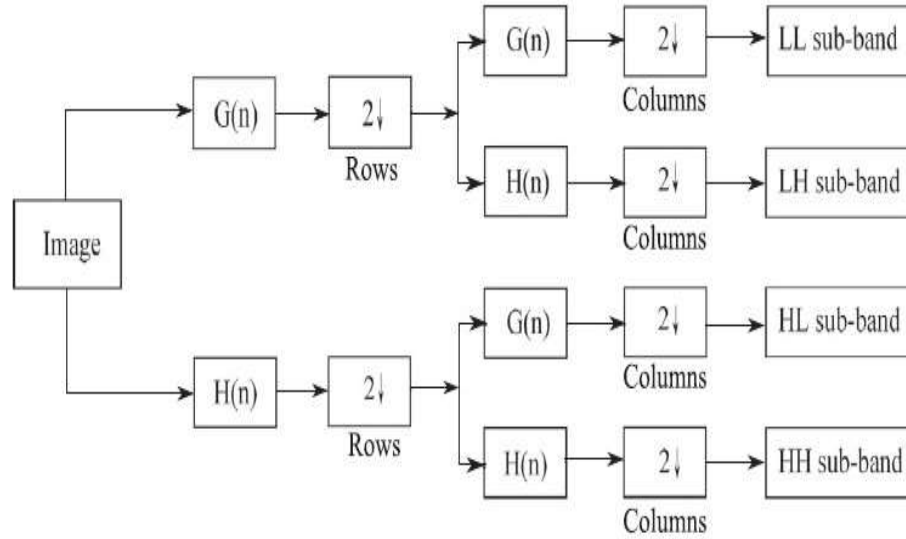


Figure 4.7. 2D discrete wavelet transform.

Figure 4.7 depicts the images adhered to every dimension individually into rows and columns of the image after it has been subjected to linear and two-dimensional Wavelet transform. As a consequence, four bands are produced to get pictures at every level (LL: low-low, LH: low-high, HL: high-low, HH: high-high). Images from three specific sub-bands are included, LH ( $D_j^h$ ), HL ( $D_j^v$ ), HH ( $D_j^d$ ) are detailed images that run horizontally, vertically, and diagonally. The approximation image applied for two-dimensional estimation at the following level is LL ( $A_j$ ) sub-band. Figure 4.8 depicts a knee MR image with a two-channel discrete wavelet transform.

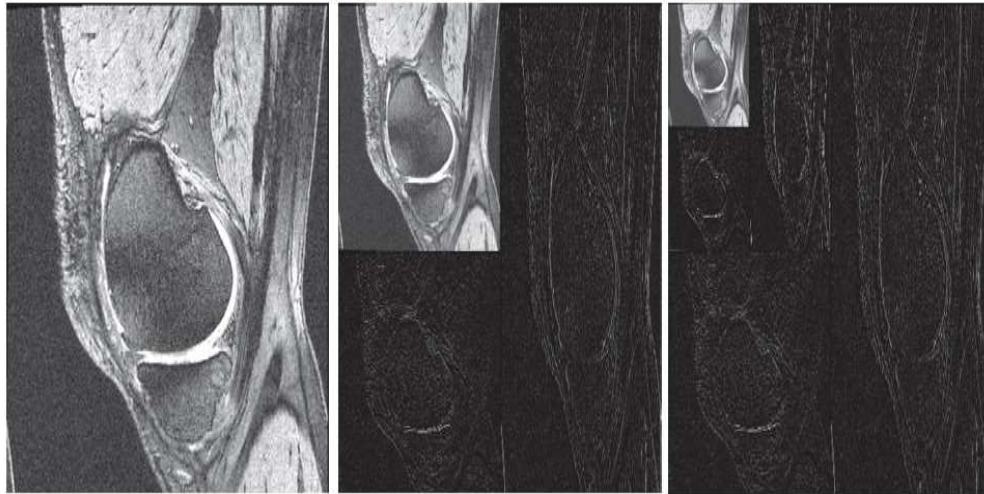


Figure 4.8. Knee MR Image with wavelet transforms coefficient at two-channel decomposition.

There are several varieties of wavelet transforms, the most common of which being the Harr wavelet. Because the Harr wavelet is both orthogonal and symmetrical, it produces satisfactory accuracy. Furthermore, it is computationally efficient when extracting morphological information from the images. In this dissertation, we analyzed and calculated the two-channel decomposition of the Harr wavelet as a feature vector (FV) for every image. By aggregating all of the FV from N pictures, an approximate feature vector of size  $N \times M$  comprising M features with each image is generated. Algorithm 2 shows the processes for creating a feature extraction matrix.

The feature vector obtained by the two-channel decomposition is pretty excellent and result in higher computational efficiency. To address the issue of the system's reduced capability to deal with missing information, feature normalization is employed, thereby boosting the overall efficiency of the system. For example, if the image size is  $256 \times 256$ , the feature vector size is  $32 \times 32 = 1024$ . In general, all characteristics are irrelevant for categorization and are utilized to reduce the dimensionality. Algorithm 3 depicts the feature normalization algorithm. The techniques of two-channel dimensionality of the Harr wavelet for feature extraction decrease the number of parameters to  $32 \times 32 = 1024$ . These major characteristics are merely normalized while maintaining the same quantity of features, i.e., 1024. However, the feature

vector size is still too huge and therefore should be minimized. As a consequence, feature reduction is often used to reduce the dimension of the feature vector. Algorithm 4 depicts the feature reduction.

**Algorithm 2.** Feature Extraction Process

**Input:** N: Total quantity of knee MR images with size K X K

**Output:** Feature Matrix (FM): [1: N, 1: M], wavelet coefficient of level-2 Harr wavelet.

1. Initialize  $i \leftarrow 1$ ,  $M \leftarrow k/8 \times K/8 =$  Total number of features to be obtained from the image.
2. Empty matrix (EM) and empty vector (EV) to be created.
3. **for**  $n \leftarrow 1$  to N **do**
4. Get MRI(n)
5.  $EM(n) [1: k/8, 1: k/8] \leftarrow$  wavelet coefficient
6. **while**  $i \leftarrow M$  **do**
7. **for**  $s \leftarrow 1$  to  $(k/8)$  **do**
8. **for**  $t \leftarrow 1$  to  $(k/8)$  **do**
9.  $FV(n) [1:i] \leftarrow EM(n) [s,t]$
10.  $i \leftarrow i+1$
11. **end for**
12. **end for**
13. **end while**
14.  $FM[n, 1:M] \leftarrow [1, 1:M]$
15. **end for**

<b>Algorithm 3.</b> Feature Normalization Process
<p><b>Input:</b> FM [1: N, 1: M]: Feature Matrix (N: Total quantity of images, M: Total quantity of features)</p> <p><b>Output:</b> NFM [1: N, 1: M]: StandardizedFM, avg(), and std().</p> <ol style="list-style-type: none"> <li>1. Empty matrix NFM [1: N, 1: M] and two empty matrices MU [1, 1: M] and SU [1, 1: M] to be created.</li> <li>2. MU [1, 1:M] &lt;- avg(FM)</li> <li>3. SU [1,1: M] &lt;- std(FM)</li> <li>4. <b>for</b>i&lt;- 1 to M <b>do</b></li> <li>5.   NFM [1: N, i] &lt;- (FM [1: N, i] – MU [1,i]) / SU [1,i]</li> <li>6. <b>end for</b></li> </ol>

<b>Algorithm 4.</b> Feature Reduction Process
<p><b>Input:</b> NFM [1: N, 1: M]: Feature Matrix (N: Total quantity of images, M: Total quantity of features)</p> <p><b>Output:</b> X [1: N, 1: R]: MinimizedFM., ca (): compute coefficient</p> <ol style="list-style-type: none"> <li>1. Choose R: Minimized dimension.</li> <li>2. Empty matrix X [1: N, 1: R] to be created.</li> <li>3. X[1: N, 1: R] &lt;- ca(NFM,R)</li> <li>4. Get empty matrix X.</li> </ol>

#### 4.2.5 Masking

The extraction of cartilage and synovial fluid is attached to the subchondral bone such as femur and tibia can be localized and masked by proposed architecture. The architecture involves several steps using proposed technique to mask the boundary points. Therefore, the design of masking for whole dataset is proposed in this research. The bone segmentation is followed by multiple levels such as cartilage and synovial fluid masking.

The extraction of bone cartilage interface is given by simple dot operation as shown in equation 4.19. In equation 4.20 the dilation operator and erosion operator represented as  $\oplus$ , and  $\ominus$ . The corrected bone segments are shown as  $Stack(corr)$ , and  $S(mask)$  is the structuring element for dilation and erosion. The bone cartilage interface (BCI) such as cartilage, meniscus and synovial fluid can be obtained through masked BCI image. Use of Otsu's thresholding as shown in equation 4.21 for estimating the BCI image into three classes background, non-cartilage, and cartilage-synovial region. In equation 4.21  $T_1$  and  $T_2$  defines optimal threshold values with a maximum variance defined by  $\sigma_v$ , and  $L$  defines the maximum gray level. Through the studies carried out the cartilage thickness is 4mm, synovial tissue thickness is limited to 4mm. As the segmented region of cartilage and synovial fluid are different, so it is required to obtain accurate estimation. However, there are some additional features that are incorporated with tissue structure. Therefore, the curvature of individual boundary pixel is estimated with equation 4.22.

$$BCI = Image \times Masking \quad (4.19)$$

$$Masking = (Stack(corr) \oplus S(mask)) - (Stack(corr) \ominus S(mask)) \quad (4.20)$$

$$\sigma_v^2(T_1, T_2) = \max_{1 \leq T_1, T_2 \leq L} \sigma_v^2(T_1, T_2) \quad (4.21)$$

$$K(n) = \frac{x'(n)x''(n) - y'(n)y''(n)}{((x'(n)^2 + y'(n)^2)^{3/2}} \quad (4.22)$$

where  $K(n)$  is the curvature of individual boundary point.  $x'(n)$ ,  $x''(n)$ ,  $y'(n)$ ,  $y''(n)$  are first as well as second order derivatives of boundary point w.r.t  $x$  and  $y$  coordinates respectively. The curvature for classification of synovial fluid is estimated using equation 4.23.

$$\tau_{th} = mean(K) - 0.75 * std(K) \quad (4.23)$$

The boundary points with higher than curvature threshold ( $\tau$ ) is classified as cartilage points and lower threshold values are classified as synovial points.

### 4.3 Performance Evaluation and Discussions

Experimentation on several MR datasets were carried out to illustrate the applicability of the suggested method. T1, T2, and Flair images from a local infirmary and the Osteoarthritis Initiative (OAI) dataset were used for the training assessment. Dice similarity coefficient (DSC), average surface distance (ASD), root mean squared error (RMSE), volume difference (VD), and volume overlap error (VOE) were used to improve the performance of the developed Discrete-MultiResUNet architecture. To demonstrate the increase in architectural effectiveness, the model was trained without entropy loss. These performance assessment measures are derived by comparing the outcomes of the proposed methodology to the ground facts achieved by experienced manual segmentation. Figure 4.9 depicts the automated seed point selection procedure in MR slices, as well as the related first bone area extraction procedure. The suggested approach can locate and pick seed locations in extremely tiny areas of bones.

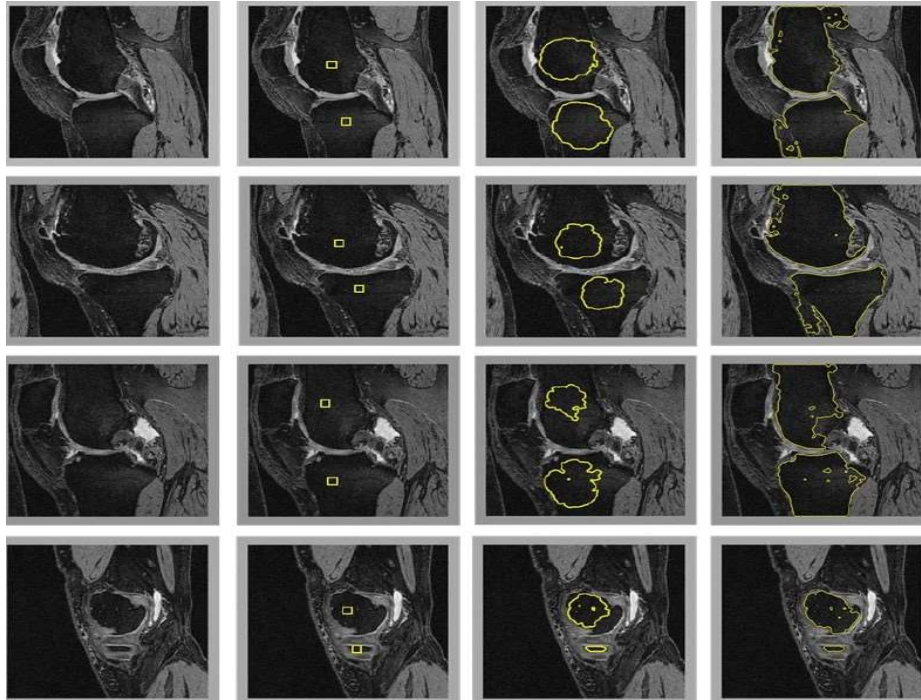


Figure 4.9. Automated seed point identification and bone region extraction. (Row 1) Original image, (Row 2) Identification of seed point in femur and tibia bones. (Row 3) Evolution of femur and tibia bone regions. (Row 4) Bone region extracted for femur and tibia bones.

The outcomes of the initial bone feature extraction stage, as illustrated in figure 4.9, demonstrate that curved evolved not only removes bone but also part of the tissues around the bone. Figure 4.10 depicts the ultimate segmentation accuracy of boundary detection and analysis. To illustrate the resilience of the proposed approach, slices from datasets are displayed. The very first column displays the initial MR image, the second column displays the manual segmented MR image, the third column displays bone extraction prior to boundary adjustment, the fourth column displays the significant findings MR image, and the last column displays segmentation overlain on the actual images.

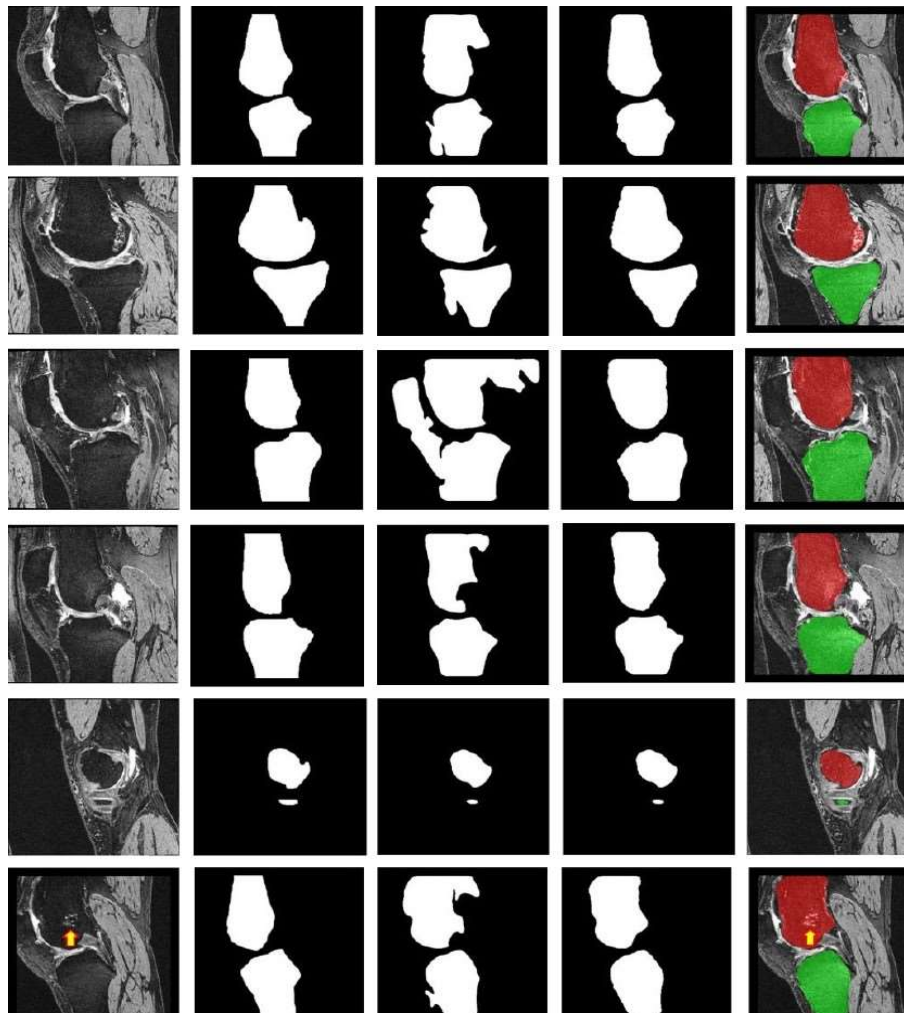


Figure 4.10. (a) Original image (b) Manual segmentation (c) Bone extraction (d) Bone extraction after boundary correction (e) Segmentation overlain on original image.

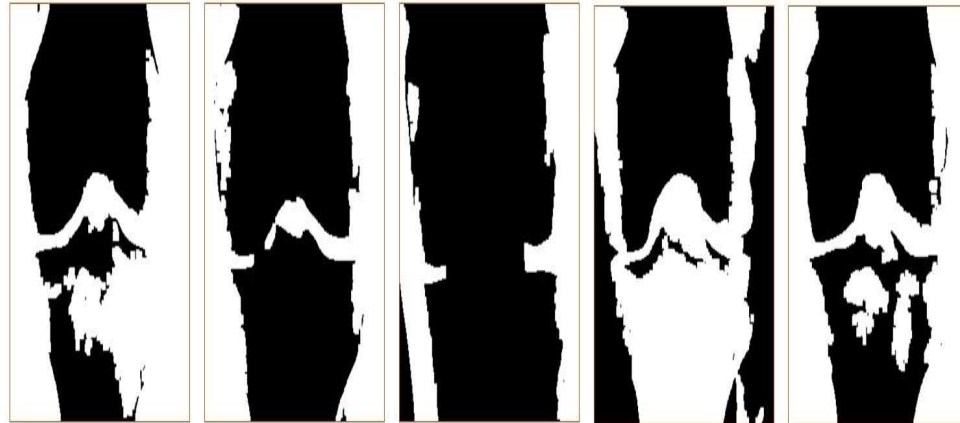


Figure 4.11. Masked MR images surrounded the bone tissues.

Figure 4.11 depicts the masking of the femoral and tibial tissue boundaries. Figure illustrates different MR images that show bone and tissue boundary masked. The effectiveness of the suggested approach is assessed in this dissertation employing measures such as dice similarity coefficient (DSC), average surface distance (ASD), root mean square distance (RMSD), volume difference (VD), and volume overlap error (VOE), which are mentioned in the preceding chapter. These performance measurements are derived from the suggested approach and compared to expert-provided ground truth data.

Independent quantitative analyses for the femoral and tibial bones were performed to offer a better understanding of the suggested approach. As observed in the table 4.1 the DSC, ASD, and RMSD values for femur bone were 98.3%,  $0.16\text{mm} \pm 0.08$ , and  $0.36\text{mm} \pm 0.04$  respectively. Similarly, the DSC, ASD, and RMSD values for tibia bone were 98.5%,  $0.17\text{mm} \pm 0.04$ , and  $0.37\text{mm} \pm 0.04$  respectively. The femoral cartilage values for VD and VOE are  $1.4 \pm 5.93$  and  $18.3 \pm 5.56$  respectively. The tibial cartilage values for VD and VOE are  $-1.0 \pm 11.82$  and  $24.5 \pm 6.43$  respectively. The results obtained for Osteoarthritis Initiative (OAI) were quite similar to local dataset. In table 4.2 demonstrates the DSC, ASD, and RMSD values for femoral tissue such as  $97.6 \pm 0.33$ ,  $0.14\text{mm} \pm 0.03$ , and  $0.38\text{mm} \pm 0.08$  respectively. Similarly, the DSC, ASD, and RMSD values for tibial tissue were 96.2%,  $0.15\text{mm} \pm 0.04$  and  $0.39\text{mm} \pm 0.06$  respectively. The VD and VOE for femoral and tibial cartilage were  $1.7 \pm 6.68$ ,  $19.4 \pm 3.79$ ,  $-1.4 \pm 9.12$  and  $21.3 \pm 2.90$  respectively.



Table 4.1. DSC, ASD, and RMSD values for local dataset.

	<i>DSC (%)</i>	<i>ASD (mm)</i>	<i>RMSD</i> <i>(mm)</i>	<i>VD (%)</i>	<i>VOE</i> <i>(%)</i>
<i>Femoral bone</i>	98.3 ± 0.40	0.16 ± 0.08	0.36 ± 0.04	-0.07 ± 0.88	2.7 ± 0.52
<i>Tibial bone</i>	98.5 ± 0.37	0.17 ± 0.04	0.37 ± 0.06	-0.04 ± 0.84	2.8 ± 0.61
<i>Femoral cartilage</i>	88.4 ± 3.48	0.18 ± 0.07	0.38 ± 0.11	1.4 ± 5.93	18.3 ± 5.56
<i>Tibia cartilage</i>	85.4 ± 4.57	0.22 ± 0.16	0.63 ± 0.36	-1.0 ± 11.82	24.5 ± 6.43

Table 4.2. DSC, ASD, and RMSD values for OAI dataset.

	<i>DSC (%)</i>	<i>ASD (mm)</i>	<i>RMSD</i> <i>(mm)</i>	<i>VD (%)</i>	<i>VOE</i> <i>(%)</i>
<i>Femoral bone</i>	97.6 ± 0.33	0.14 ± 0.03	0.38 ± 0.08	-0.17 ± 0.57	2.5 ± 0.83
<i>Tibial bone</i>	96.2 ± 0.42	0.15 ± 0.04	0.39 ± 0.06	-0.14 ± 0.92	2.2 ± 0.31
<i>Femoral cartilage</i>	86.4 ± 2.77	0.16 ± 0.06	0.40 ± 0.14	1.7 ± 6.68	19.4 ± 3.79
<i>Tibia cartilage</i>	83.4 ± 5.13	0.23 ± 0.19	0.69 ± 0.29	-1.4 ± 9.12	21.3 ± 2.90

The assessment for lateral and medial meniscus of femur and tibia bones are shown in table 4.3. The mean difference (MD) values obtained are  $-33.53\text{mm}^3$ , and  $-25.26\text{mm}^3$  for lateral and medial meniscus volume. The standard deviation (SD) values for lateral meniscal length and width obtained were 0.37mm and 0.45mm. The SD values obtained for lateral and medial meniscal volume were 35.62mm and 33.75mm. The lower limit (LL) value obtained for lateral and medial meniscal length were -0.54mm

and -0.32mm. The upper limit (UL) values obtained for lateral and medial meniscal volume were 32.70mm<sup>3</sup> and 41.54mm<sup>3</sup>.

Table 4.3. Assessment of meniscus for knee MR image

	<i>MD</i>	<i>SD</i>	<i>LL (d-2s)</i>	<i>UL (d+2s)</i>
<i>Lateral meniscal length (mm)</i>	0.21	0.37	-0.54	0.94
<i>Lateral meniscal width (mm)</i>	0.45	0.45	-0.49	1.31
<i>Medial meniscal length (mm)</i>	0.52	0.42	-0.32	1.35
<i>Medial meniscal width (mm)</i>	0.18	0.46	-0.72	1.10
<i>Lateral meniscal volume (mm<sup>3</sup>)</i>	-33.53	35.62	-95.80	32.70
<i>Medial meniscal volume (mm<sup>3</sup>)</i>	-25.26	33.75	-96.66	41.54

#### 4.4 Conclusion

This chapter discusses the automatic segmentation technique from knee MR images. This segmentation is obtained in several stages like denoising, initial seed selection, bone area extraction, lastly boundary outflow recognition and adjustment, and lastly masking the tissues. In order to separate cartilage from synovial tissue curvature

estimation is adopted that is capable of partitioning these tissues with BCI. Since, cartilage being on the surface of bones whereas synovial fluid has no curvature because of fluid nature direct segmentation from MR images is difficult due to variation in intensity values. This technique overcomes the present leakages of boundary selection of cartilage, non-cartilage (synovial) regions and corrects the tissue selection. This proposed technique has presented exemplary performance in selection and masking the knee tissue structure. The performance of proposed technique is validated through various quantitative and qualitative parameters such as DSC, ASD, RMSD, VD, and VOE for femur and tibia bone, and for meniscus MD and SD. The parameters obtained for both local and OAI datasets are of significantly high value in terms of performance and clinical applicability of proposed system.

## Chapter 5

### Automatic Classification of Rheumatoid Arthritis with KL Grading

This chapter presents the proposed architecture of ResNet50 with optimization of model. The chapter is structured in following manner: Section 5.1 describes introduction about classification using KL grading, Section 5.2 describes ResNet50 architecture with Adam optimizer, Section 5.3 illustrates results and discussions, finally concludes the chapter in Section 5.4.

#### 5.1 Introduction

The main proportion of the expense of treatment arises from patients' lack of awareness and unable to detect and diagnose symptoms early since their impact may be reduced or their progression of future incapacitation can be slowed. Only accessible health support alternatives for early diagnosis and behavioral intervention due to the severe stage of RA. Medical imaging has been used to make an early diagnosis of RA. These MR images have been effectively used in a wide range of applications, including medical issue monitoring, treatment, and assessment. Advances in intelligent systems and medical imaging methods have resulted in a rapid increase in the potential use of AI Technology in different medical activities such as diagnoses, early evaluation, and classification. These medical imaging techniques produce a visual depiction of the interior of the body. MR images have been shown to be trustworthy and gold standard for clinical examination of tissue and joints among numerous medical modalities such as X-ray[138], Computerized tomography, Ultrasonography, and MR imaging to identify obvious stages of knee Arthritis[58].

X-ray images of Arthritis are often inspected by healthcare professionals, who subsequently define the seriousness of knee Arthritis according on KL grade levels[158]. KL assessment is the standard method for assessing the seriousness of knee Arthritis and is widely adopted worldwide. As illustrated in figure 5.1, the KL grading divides the knee MR images into five classes ranging from zero to four. The diagnosis accuracy varies and is dependent on the expertise and cautiousness of the

health care professional. Fine-grained classification of images is necessary for effective categorization of knee RA diagnosis. However, if conventional procedures meant for classification are used, this classification process will be extremely difficult for features, pixel, transforms, histogram, etc. These manual methods require expert in domain knowledge, efforts, and laborious task. Therefore, the classification process has been automated instead of manual.


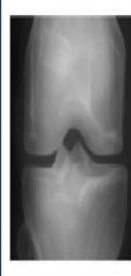
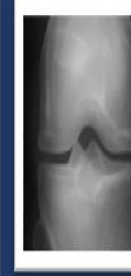


K-L Grade	<i>Grade 0</i>	<i>Grade 1</i>	<i>Grade 2</i>	<i>Grade 3</i>	<i>Grade 4</i>
Sample images					
Classification	<i>Normal</i>	<i>Doubtful</i>	<i>Mild</i>	<i>Moderate</i>	<i>Severe</i>
Description	<i>No features of OA</i>	<i>Minute Osteophyte: Doubtful significance</i>	<i>Definite Osteophyte: Normal Joint Space</i>	<i>Moderate joint space reduction</i>	<i>Joint Space greatly reduced: subchondral sclerosis</i>

Figure 5.1. KL grading stages for knee RA (Source: [159])

Intelligent technologies have ushered in a new era of computer-assisted diagnostics. As sophisticated models, intelligent systems that enable clinical assessment and have the ability to achieve human-level performance are utilized. Convolutional neural networks (CNN) [145] have indeed been commonly used in medicine imaging, segmentation, and classification tasks, acquiring all significant and useful image characteristics. These intelligent systems investigated the study of RA-affected knee joints and offered an end-to-end categorization framework. These advanced technologies additionally assist high - dimensional data in not only classifying and yet also predicting the course of knee RA.

The primary pathological characteristics are obvious on MR imaging as cartilage erosion may be evaluated by seeing joint space narrowing/ width (JSN/ JSW) and bone degradation in the joint region. As previously stated, the KL classification is the standard method for diagnosing knee RA. Unfortunately, the KL classification suffers from expertise subjectivity, and its effectiveness is dependent on healthcare

professionals' expertise, which may be influenced by intra- and inter observer inconsistency. Even the same specialist might misinterpret the seriousness of RA development in the knee over time. Misinterpretation in the near grading (grades 3 and 4) is yet another significant shortcoming of the KL grading system. The Osteoarthritis Research Society International (OARSI) recently proposed an alternative grading system which is more feature specific. The new approach is based on characteristics such as femoral osteophytes, tibial osteophytes, and joint space narrowing / breadth, which are evaluated individually in a specific way.

Furthermore, the revised OARSI system grading method, like KL classification, suffers from subjectivity such as intra- and inter observer inconsistency, making early development of knee RA diagnosis a difficult task. Rheumatologists utilize the intelligent medical diagnostic system (IMDS) to evaluate the severity of knee RA in order to create a common basis for them. Because of the prevalence of knee RA, a completely automated knee RA severity rating system is desperately required. Numerous approaches for automatically identifying the seriousness of knee RA based on the clinical characteristics of the knee joint have already been explored in this research. These machine learning and deep learning-based approaches may have adequately assessed the seriousness of knee RA. Furthermore, the diagnostic accuracy of these approaches has surpassed that of humans and exceeds that of experienced professionals. Deep learning (DL) is a machine learning approach that learn from the characteristics of an MR image in order to better understand and categorize the KL classification of knee RA. In this research, a deep learning approach (ResNet50) with an optimization technique is developed. Section 5.2 goes through the suggested technique with further detail.

## **5.2Methodology**

Framework for the diagnosis of RA with KL grading is depicted in figure 5.2. This framework is capable of classifying the knee MR images using KL grading system. The steps carried out are denoising, segmentation (tissue selection, boundary correction, and masking), and followed by classification. Step by step discussion on the process of grading is discussed in this section. The MR images are autonomously

evaluated in this research, revealing the presence of bone deterioration and joint space narrowing abnormalities. The framework uses ResNet50 architecture that is variant of ResNet model consisting of 48 layers of convolutional along with 1 max-pooling, and 1 average pool. In figure 5.2 the knee input data images are denoised with proposed SANR\_CNN architecture [149][150] as discussed in section 3.3, the preprocessed knee MR images are then segmented using the developed hybrid approach, i.e. Discrete-MultiResUNet [160] with boundary correction and masking the tissue structure as discussed in section 4.2. The features such as joint space narrowing, synovial fluid, cartilage thickness, meniscus volume with width is extracted for further classification using KL grading.

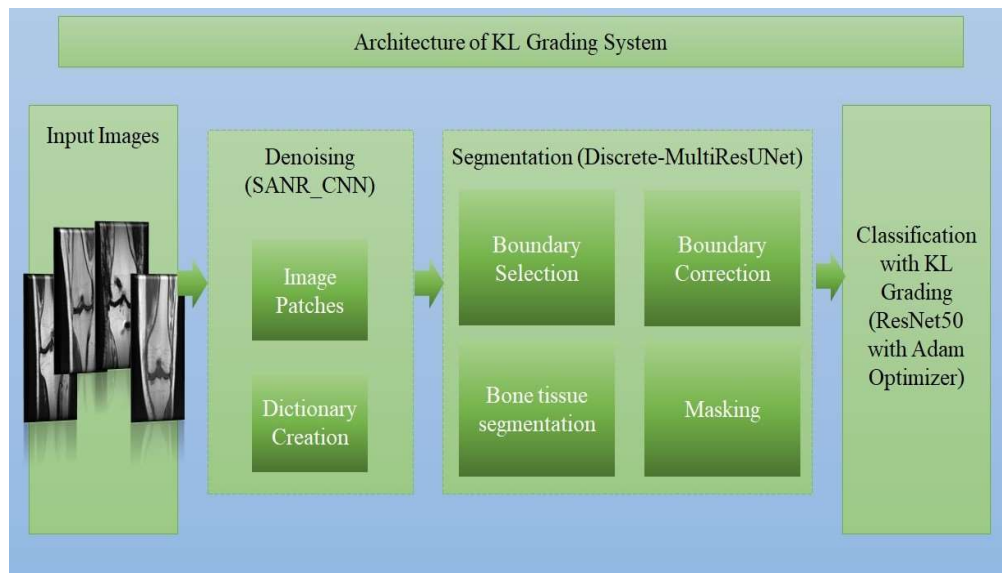


Figure 5.2. Proposed classification framework with KL Grading.

### 5.2.1 ResNet50 Architecture

The ResNet architecture is inspired by VGG architecture that concentrates on depth of network. This ResNet design is basically identical to networks with convolutional, pooling, activation function, and a fully - connected layer. Figure 5.3 demonstrates the ResNet framework with skip connection. The skip connection in the ResNet architecture ignores certain layers and sends the data from one layer as the input to the appropriate layers. Due to skip connection the weights are not biased, and they will allow the lower layers of model to learn as good as higher layer. The information

from the initial layers is passed to deeper layers by matrix dot product calculation. These ResNet layers are residual network made up from residual blocks where the weights will get multiplied with input 'x'. The activation function  $f()$ , with output as  $h(x)$  is denoted as shown in equation 5.1 and 5.2. The skip connection is padded with zero values to increase the dimension where equation 5.3 denotes the projection method.

$$h(x) = f(wx + b) \tag{5.1}$$

$$h(x) = f(x) + x \tag{5.2}$$

$$h(x) = f(x) + w \cdot x \tag{5.3}$$

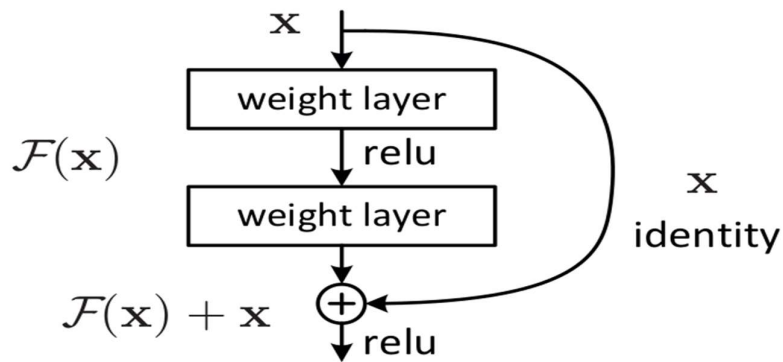


Figure 5.3. Skip connection used in ResNet architecture.

**Identity Block**

The identity block is a typical component in residual network (ResNet) design that conforms to the scenario in which the input activation and output activation have the same dimensions. Figure 5.4 depicts the identification block.

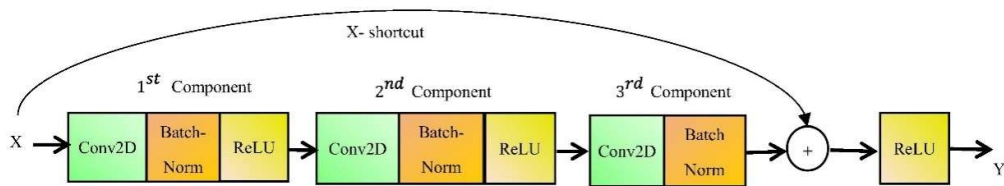


Figure 5.4. Identity block in ResNet architecture.

$$y = F[x, (W_i)] + x \tag{5.4}$$



The identity component is described in equation 5.4, wherein  $x$  and  $y$  are input, and output vectors of the layer under consideration. The residual function mapping is denoted as  $F\{x, \{W_i\}\}$ . The first component in figure 5.4 consists of two-dimensional convolutional layer with  $(1 \times 1)$  kernel size, a stride of  $(1,1)$ . The second component is identical to the first but has a filter size of  $(f \times f)$ , while the third component is similar to the first component but lacks activation component i.e., ReLU.

### Convolutional Block

When the input and output parameters don't really coincide, the convolution component is utilized. Figure 5.5 depicts a convolutional component with a Conv2D layer in the shortcut path. These pathways are determined depending on the size of the incoming information.

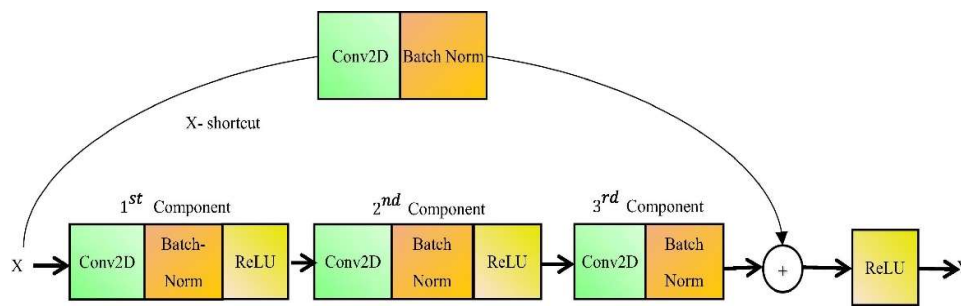


Figure 5.4. Convolutional block between shortcut path of ResNet architecture.

As illustrated in equation 5.5, the shortcut connections use linear projection  $W_s$  to enlarge the dimensionality between  $x$  and  $F$ , wherein  $F$  is the output of the multilayered layer and  $x$  and  $y$  are the input layer and aggregated corresponding output of the convolutional component, correspondingly. The design of the convolution component is built in much the same fashion as the identity component, but with an additive 2D convolutional layer instead of a 3D convolutional layer. The input 'x' is aligned with the primary route in this shortcut. Depending on the output dimension, the convolutional kernel size  $(1 \times 1)$  with stride  $(s, s)$ . Eventually, the shortcut is merged with the primary path's output. The primary objective of shortcut is to overcome the problem of disappearing gradients.

$$y = F\{[x, (W_i)]\} + W_s x \quad (5.5)$$

The ResNet50 design is divided into five stages, each of which has a convolutional component and an identity component. Each convolutional block has three convolutional layers, so each identity block contains three convolutional layers as well. Over 23 million learnable characteristics are available in the ResNet50 framework. Several low- and high-level characteristics are learned by the architecture from input layers. Table 5.1 depicts the ResNet50 design with detailed information for every layer. The ResNet design includes filter configurations with varying sizes and channel numbers. For example, at Conv\_x (x – denotes layer to x at Conv3, wherein x=1, 2, 3, because [size of filter, total number of channels X 3]).

Table 5.1. ResNet50 architecture Layer Description.

<i>Layer Name</i>	<i>50-Layer</i>
<i>Conv1</i>	7 X 7, 64, stride 2
<i>Conv2_x</i>	3 X 3 max pool, stride 2
	$\left\{ \begin{array}{l} 1 \text{ X } 1, 64 \\ 3 \text{ X } 3, 64 \\ 1 \text{ X } 1, 256 \end{array} \right\} \text{ X } 3$
<i>Conv3_x</i>	$\left\{ \begin{array}{l} 1 \text{ X } 1, 128 \\ 3 \text{ X } 3, 128 \\ 1 \text{ X } 1, 512 \end{array} \right\} \text{ X } 4$
<i>Conv4_x</i>	$\left\{ \begin{array}{l} 1 \text{ X } 1, 256 \\ 3 \text{ X } 3, 256 \\ 1 \text{ X } 1, 1024 \end{array} \right\} \text{ X } 6$
<i>Conv5_x</i>	$\left\{ \begin{array}{l} 1 \text{ X } 1, 512 \\ 3 \text{ X } 3, 512 \\ 1 \text{ X } 1, 2048 \end{array} \right\} \text{ X } 3$
<i>Average pool, 1000-d Fully connected (FC), Soft-max layer</i>	

The ResNet50 architecture is comprised of 5 stages is demonstrated in stages as follows:

Stage 1: The phase is made up of 2D convolutional filters with 7 X 7 dimensions and a stride of (2, 2). The channel's standardization is finished by batch normalization and the activation function ReLU, accompanied by max-pooling with stride (2, 2).

Stage 2: The phase is made up of one 2D convolution block and three identity blocks, each having (64, 64, 256) filters, a kernel size of (3 X 3) and a stride of (1, 1).

Stage 3: The phase is made up with one convolution component and four identity blocks, each of which employs three filters of size (128, 128, 512), with kernel size (3 X 3) and stride (2,2).

Stage 4: The stage consists with one convolution component and six identity blocks, including both filter sizes (256, 256, 1024) and kernel sizes (3 x 3) and stride (2, 2).

Stage 5: The phase is made up with one convolution component and three identity blocks, each with a different filter size (512, 512, 2048), kernel size (3 X 3), and stride (2, 2). Ultimately, using an aggregate pooling layer paired with a 1000-d fully connected layer and a soft-max layer.

### **5.2.2 Adam Optimization Technique**

Adam is the adaptive learning algorithm developed for the advancement of deep neural network algorithms. The Adam is combined with momentum from the RMSprop and the Stochastic gradient descent. Squared gradients are used to scale the learning rate such as RMSprop and employ momentum by utilizing moveable gradient averages rather than gradients themselves, like SGDs, with momentum. The algorithm calculates individual learning rates for various parameters and uses adaptive learning rate techniques to determine the various learning rates for each parameter. Adagrad also offers benefits that function in sparsely graded environments but struggles to optimize neural networks non-convexly and RMSprop to overcome some of Adagrad issues and operate inline.

Adam employs first and second gradients estimations to modify the neural network's learning rate for specific weights. The  $N^{\text{th}}$  moment of a random variable, described in equation 5.6 to the order of  $n$ , wherein  $m$  represents momentum and  $x$  is a random process.

$$m_n = E[X^n] \quad (5.6)$$

The first is average momentum, while the second is uncentered variance momentum. Adam utilises exponentially weighted moving average values estimated on gradients with mini batches to compute momentum, as illustrated in equations 5.7 and 5.8, wherein  $m$  and  $v$  are moving average values,  $g$  is slope on existing mini batches, and  $\beta$  is the computation hyper-tuning parameter. Because  $m$  and  $v$  are approximations of first and second moments, we get the condition given in equations 5.9 and 5.10.

$$m_t = \beta_1 m_{t-1} + (1 - \beta_1) g_t \quad (5.7)$$

$$v_t = \beta_2 v_{t-1} + (1 - \beta_2) g_t^2 \quad (5.8)$$

$$E[m_t] = E[g_t] \quad (5.9)$$

$$E[v_t] = E[g_t^2] \quad (5.10)$$

The estimators' assumed outcomes must approximate the parameter being assessed. If the properties in equation 5.9 and 5.10 are true, then we have unbiased estimators. As the values won't be held true for moving averages because the averages are initialized to zeros. To prove this, the initial value of  $m$  is first gradient as shown in equation 5.11. The equation 5.11 can be rewritten as shown in equation 5.12.

$$\begin{aligned} m_0 &= 0 \\ m_1 &= \beta_1 m_0 + (1 - \beta_1) g_1 = (1 - \beta_1) g_1 \\ m_2 &= \beta_1 m_1 + (1 - \beta_1) g_2 = \beta_1 (1 - \beta_1) g_1 + (1 - \beta_1) g_2 \\ m_3 &= \beta_1 m_2 + (1 - \beta_1) g_3 = \beta_1^2 (1 - \beta_1) g_1 + \beta_1 (1 - \beta_1) g_2 + \beta_1 (1 - \beta_1) g_3 \end{aligned} \quad (5.11)$$

$$m_t = (1 - \beta_1) \sum_{i=0}^t \beta_1^{t-i} g_i \quad (5.12)$$

Let's the expected value of  $m$  is denoted as shown in equation 5.13 with bias correction in first momentum estimator.

$$\begin{aligned}
E[m_t] &= E[(1 - \beta_1) \sum_{i=1}^t \beta_1^{t-i} g_i] \\
&= E[g_i] (1 - \beta_1) \sum_{i=1}^t \beta_1^{t-i} + \zeta \\
&= E[g_i] (1 - \beta_1^t) + \zeta
\end{aligned} \tag{5.13}$$

The following equation 5.13 reveals two aspects: (i) They have a biased estimator. (ii) It may have little impact unless it is applied at the start of the learning since the beta coefficient to the order of t is nil. Equations 5.14 and 5.15 illustrate the approximated formulae with the necessary modification to anticipated values.

$$\hat{m}_t = \frac{m_t}{1 - \beta_1^t} \tag{5.14}$$

$$\hat{v}_t = \frac{v_t}{1 - \beta_2^t} \tag{5.15}$$

$$w_t = w_{t-1} - \eta \frac{\hat{m}_t}{\sqrt{\hat{v}_t + \epsilon}} \tag{5.16}$$

Equation 5.16 shows exactly Adam conducts the weight update, wherein w is the model parameters and eta is the scaling factor. However, the Adam has some disadvantages related to weight decay. So, slight modification in Adam optimizer to use weight decay with update rule is shown in equation 5.17. The equation defines regularization by small relative amount ( $\lambda$ ) of weight decay parameter than other weights. The weight decaying adaptable formula is shown in Equation 5.18, wherein b is the batch size, B is the overall number of input points per epoch, and T is the maximum number of epochs. The weight decay rate is used to regularise all weights. Using Adam weight decay reduces testing errors, aids in the decoupling of learning algorithm, and regularises hyper-parameters.

$$w_t = w_{t-1} - \eta \left( \frac{\hat{m}_t}{\sqrt{\hat{v}_t + \epsilon}} + \lambda w_{t-1} \right) \tag{5.17}$$

$$\lambda = \lambda_{norm} \sqrt{\frac{b}{BT}} \tag{5.18}$$

### 5.3 Results and Discussions

To illustrate the experimental observations, the proposed ResNet50 technique's performance was evaluated with a variety of characteristics such as confusion matrix, efficiency, precision, sensitivity, specificity, F1-measure, mean absolute error (MAE),

and joint space narrowing (JSN). Purpose of providing linearity in training using Adam optimizer, the dataset is generally split by k-fold cross validation. The training rate was set to 0.001, while the weight decaying was adjusted to 0.0001. The proposed research performed on an Intel core i3-7130U Processor operating at 2.70GHz with 12 GB RAM. The dataset was classified by the model based on its KL classification / scoring. If the JSN value is zero, the arthritis is labelled as grade 0; if the JSN value is less than 10%, the arthritis is labelled as grade 1,(doubtful arthritis). If the JSN value is between 11% and 25%, it is labelled as mild arthritis; if it is between 26% and 75%, it is labelled as moderate arthritis; and if it is higher than 75%, it is labelled as degenerative arthritis (severe arthritis).

Table 5.2 demonstrates the datasets used for analysis of results for progression of arthritis. First dataset was collected from local hospital and second collected from Osteoarthritis Initiative (OAI) database. The local dataset was a raw data so, needed to be pre-process as discussed in chapter 3. The OAI dataset was a pre-processed data so directly used for experiments. Both datasets were consisting of different training, testing and validation samples. The data was divided according to k-fold cross validation approach into training set (70%), validation (10%), and testing set (20%).

Table 5.2. Datasets used for experimental analysis.

<i>Dataset</i>	<i>Local</i>			<i>OAI</i>		
	Training	Testing	Validation	Training	Testing	Validation
<i>Grade 0</i>	10115	2578	1193	2286	639	328
<i>Grade 1</i>	7132	1783	967	1046	296	153
<i>Grade 2</i>	5256	1329	650	1516	447	212
<i>Grade 3</i>	4379	1052	508	757	223	106
<i>Grade 4</i>	4833	1186	624	173	51	27

As the proposed architecture uses transfer learning that helps in convergence of deep learning model (ResNet50). Table 5.3 describes the performance parameters used for local dataset. The JSN values for grades from 0 to 4 are well estimated and grade 4

has value of 0.99. The proposed model achieved sensitivity of 0.97 on an average value for all grades. The specificity achieved for grade 1 and grade 4 are 0.84 and 0.92 respectively. The model also achieved an accuracy of 97.98%, 95.50%, 95.26%, 96.73%, and 98.15%, for grade 0, 1, 2, 3, and 4 respectively. The MAE estimated was 0.092 and 0.203 for grade 0 and grade 2 respectively. Table 5.4 describes the performance parameters used for OAI dataset.

Table 5.3. Different performance parameters with KL grade on local dataset.

<i>KL grades</i>	<i>JSN</i>	<i>Precision (%)</i>	<i>Sensitivity</i>	<i>Specificity</i>	<i>F1-score</i>	<i>Accuracy (%)</i>	<i>MAE</i>	<i>AUC</i>
<i>Grade 0</i>	0.98	0.99	0.97	0.90	0.98	97.98	0.092	0.97
<i>Grade 1</i>	0.98	0.95	0.98	0.84	0.97	95.50	0.197	0.96
<i>Grade 2</i>	0.97	0.95	0.98	0.87	0.97	95.26	0.203	0.96
<i>Grade 3</i>	0.98	0.98	0.97	0.86	0.98	96.73	0.119	0.97
<i>Grade 4</i>	0.99	0.99	0.99	0.92	0.99	98.15	0.088	0.97

Table 5.4. Different performance parameters with KL grade on OAI dataset.

<i>KL grades</i>	<i>JSN</i>	<i>Precision (%)</i>	<i>Sensitivity</i>	<i>Specificity</i>	<i>F1-score</i>	<i>Accuracy (%)</i>	<i>MAE</i>	<i>AUC</i>
<i>Grade 0</i>	0.96	0.97	0.96	0.91	0.96	97.68	0.082	0.97
<i>Grade 1</i>	0.96	0.97	0.97	0.86	0.97	96.37	0.317	0.97
<i>Grade 2</i>	0.95	0.95	0.96	0.85	0.98	96.76	0.283	0.96
<i>Grade 3</i>	0.96	0.98	0.97	0.87	0.97	97.10	0.039	0.97

<i>Grade</i>	0.98	0.98	0.98	0.88	0.98	98.77	0.028	0.97
4								

Table 5.5. Comparative analysis of different techniques related to lateral and medial femur and tibia tissue with JSN value.

<i>Techniques</i>	<i>Femur</i>		<i>Tibia</i>		<i>JSN</i>		<i>Accuracy (%)</i>	<i>MAE</i>
	L	M	L	M	L	M		
<i>SVM</i> [133]	0.71	0.73	0.78	0.77	0.91	0.87	86.53	0.319
<i>RF</i> [161]	0.68	0.69	0.80	0.78	0.90	0.87	87.84	0.308
<i>VGG</i> [58]	0.84	0.81	0.82	0.79	0.91	0.87	90.45	0.216
<i>CNN</i> [137]	0.83	0.84	0.82	0.79	0.91	0.87	91.89	0.285
<i>Dense-Net</i> [58]	0.85	0.84	0.83	0.80	0.92	0.88	93.77	0.270
<i>ResNet34</i> [162]	0.86	0.86	0.84	0.82	0.92	0.88	94.39	0.216
<i>Proposed Model</i>	0.88	0.86	0.86	0.89	0.93	0.91	96.85	0.105

Table 5.5 provides a comparative analysis of several techniques used to address femoral and tibial tissues, wherein L indicates lateral, and M represents medial. Only the medial and lateral compartments of femoral and tibial tissue are examined. The proposed architecture achieved an accuracy of 96.85% which is quite good compared to other existing techniques. The residual network of 34 layers (ResNet34) also achieved good results with an accuracy of 94.39% which is near to proposed architecture. The Dense-Net model gained good result for lateral JSN value of 0.92. For the lateral compartment, the support vector machine (SVM), oxfordNet (VGG), and convolutional neural network (CNN) methods simultaneously obtained a really reasonable result of 0.91. The random forest (RF) gained less attention for



every compartment analysed. Table 5.6 illustrates the performance measures achieved for proposed model. Figure 5.6 illustrates the confusion matrix estimated for proposed model. The confusion matrix illustrates the classification model's performance on the testing dataset. The true-positive were 4433 knee MR images, the true-negative sample images were 3245. Table 5.6 shows some parameters such as false negative and positive rate that are 0.0378 and 0.0229 respectively. It also has a coefficient of correlation of 0.9258 and a false discovery rate of 0.0169.

Table 5.6. Performance parameters achieved for proposed model.

<i>Performance parameters</i>	<i>Obtained value</i>
<i>Sensitivity or Recall</i>	0.9622
<i>Specificity</i>	0.9771
<i>Precision</i>	0.9831
<i>Negative predicted value</i>	0.9491
<i>False-positive rate</i>	0.0229
<i>False discovery rate</i>	0.0169
<i>False-negative rate</i>	0.0378
<i>Accuracy</i>	0.9685
<i>F1 score</i>	0.9726
<i>Matthew's correlation coefficient</i>	0.9258

**Confusion Matrix**

Output Class	Normal	4433	76	0.984 0.016
	RA	174	3245	0.051 0.949
		0.963 0.037	0.978 0.022	0.96 0.04
		Normal	RA	
		Target Class		

Figure 5.6. Confusion matrix for proposed architecture (ResNet50)

A unique technique for automatically identifying and evaluating knee RA is proposed in this research. The model used Knee MR images that are collected from local and OAI dataset. The proposed approach that is residual network (ResNet50) was trained with Adam optimizer with slight modification in weight decay hyperparameter. Therefore, the training provided less errors in testing of knee images. To my knowledge, Oka et al.,[163] used to evaluate knee characteristics, whereas Tiulpin et al.,[158] used a systematic technique to evaluate form and texture characteristics to diagnose arthritis. Unfortunately, these experiments had flaws, such as the fact that the text size chosen was excessively tiny in comparison to previous research, because there was prejudice in arthritis assessment. Unlike the prior research, the suggested model chose a complete contrast amongst training, testing, and validation datasets. The proposed technique's primary benefit was that it demonstrated the model's potential to learn important RA characteristics from diverse datasets. The technique involves many phases to improve the robustness of the system in order to generate a clinically relevant model. The model pre-processed with proposed denoised approach, then segmented for region of interest with masking the tissue structure. Then the relevant features are extracted and utilized for classifying the knee images with grading using JSN value. With the Adam optimizer, the approach regularises the learning and introduces additional variability into the dataset.

## **5.4 Conclusion**

There are numerous constraints to the proposed study. The validation dataset was chosen through both datasets; however, an alternate method would have been to exclude this data. Nevertheless, the developed model outperformed the other models in terms of clinical performance; it learnt local dataset results and produced higher classification efficiency for early RA assessment. Another disadvantage is the lower image quality, which may result in the loss of fine-grained detail in the images. It is feasible to even use the actual image resolution with suitable information to enhance the output. Moreover, following ground truth assessment, the professionals significantly happen to disagree with KL classification in several of the incorrectly classified images. As a result, it is conceivable that the KL grading system in the RA dataset is incorrect in some situations. Furthermore, the suggested model might be

enhanced significantly by using a new loss function that optimises and utilises a bigger quantity of data from diverse sources during learning. Finally, the images adopted for the study have been captured in uniform circumstances, with a positioning frame added. As a result, the technique cannot be immediately applied to every health care, and more research is required to comprehend the approach, which was trained using local and OAI datasets.

The likelihood offered for certain KL grades mirrors the selection process of experts, who choose amongst different KL grade levels (grade 1 and 2) by taking the closest one into account. This will help the healthcare in general providing several benefits by reducing cost and focusing on RA conditions. The research community benefits from using the proposed methodology as a framework for assessing big datasets (local and OAI).

## Chapter 6

### Conclusion and Future Scope

This dissertation's significance may be divided into two main categories, which are as follows: Section 6.1 summarizes the work presented in the thesis, highlighting the significant contribution of the proposed approach for knee arthritis, and Section 6.2 addresses the research's future opportunities.

#### 6.1 Summary of Deductions

In past few years, machine learning techniques, particularly CNN, have proven to be extremely effective in a wide range of complicated medical applications. This dissertation was a study and develop an intelligent medical diagnostic system (IMDS) based on machine learning for the diagnosis of knee arthritis. Implementation of these models has contributed to major transformation in the field of information retrieval and medical domain has also affected by this renovation. Intelligent system imitates diagnostic systems to work like human brain. In this research the intelligent system was proposed for denoising the MR images, segmentation the region of interest, and classify the image with KL grading. The primary goal of this thesis is to enhance the state-of-the-art in intelligent systems for assessing the severity of knee RA by using machine learning-based approaches. According to the research, automated evaluation of knee RA severity techniques have a low effectiveness for grade assessment. The suggested method explored and developed novel approaches for automatically classifying knee RA images employing convolutional neural networks (CNN).

This thesis describes a system for assessing RA development and classifying knee MR images. The cornerstone of this approach is denoising, which includes reducing noise levels while retaining the integrity of MR images using the developed sparse aware noise reduction convolutional neural network (SANR CNN). The challenge was to preserve the information and reduce computational time, which the proposed model achieved better in terms of PSNR, SSIM, MSE, and EM values. The dictionary learning approach store the weights during training combined with CNN, obtained possibly reduced complexity of testing the images.

The automatic segmentation approach suffers from various challenges that are addressed with design of hybrid model proposed Discrete-MultiResUNet. The proposed model has demonstrated to perform in compliance with manual segmentation by experts. The quantitative measures based on segmentation shown good outcomes that can demonstrate that involves zero human intervention. The available techniques have dependencies in terms of training and testing datasets that involves human interventions at some stage that turn into biasing errors. The proposed model achieves accurate and efficient segmentation of femoral and tibial tissues. This is achieved through seed selection, boundary leakage identification, and boundary correction. The model also achieves good result for masking of tissue outliers. The performance of proposed segmentation architecture is validated through various quantitative parameters such as DSC, VD, VOE, ASD, and RMSE values.

The new approach is presented based on ResNet50 to automatically quantify the knee RA features specifically JSN. The ResNet50 architecture is trained separately based on lateral and medial features obtained from feature extraction phase. The ResNet50 architecture is trained with Adam optimizer with slight modification in weight decay to increase the training accuracy. The approach provided better classification accuracy along with KL grades. High classification performance for KL grading and JSN value was obtained, which was similar to the gold standard for knee RA assessment. A progressive improvement was achieved for other performance metrics with error analysis compared with previous methods. The proposed study's predicted outcome is categorical KL grading (0, 1, 2, 3, and 4). Because the RA is progressive rather than discrete, the proper quantification is required.

## **6.2 Future Scope of Work**

Artificial intelligence in medical application is a dynamic and worthy research domain. Intelligent techniques have been continuously improved and combined with other techniques for efficient diagnosis of knee arthritis. Likewise, the proposed framework in this research can be extended for predicting other types of arthritis like Osteoarthritis, Gout, Juvenile arthritis, and Psoriatic arthritis. Further, several possibilities are there in future validating large number of samples. The suggested

work's limitations can be solved in future advancements to enable the capacity to segment extremely tiny bone areas from knee slices. In the event of bone splitting, the proposed technique is incapable of segmenting several bone sections. Because the technique works on single level set function initialization for each femur and tibia tissue. As, the technique can be extended to patella tissue, but the thesis limits to femur and tibia tissue only. The suggested research may be expanded to various datasets for future investigation and clinical analysis after validation. The thesis can also be extended with other features related to RA to design intelligent medical diagnostic system.

## List of Publications

Sujeet More and Jimmy Singla, “*Intelligent Medical Diagnostic Systems for Arthritis*”, International Journal of Recent Technology and Engineering (IJRTE), Volume 8, Issue 2S11, September 2019, ISSN 2277-3878.

Sujeet More and Jimmy Singla, “*Critical Findings on Restoration of Magnetic Resonance Images*”, International Journal of Innovative Technology and Exploring Engineering (IJITEE), Volume 9, Issue 5, March 2020, ISSN 2278-3075.

Sujeet More, Jimmy Singla, Ahed Abugabah and Ahmad Ali AlZubi, “*Machine Learning Techniques for Quantification of Knee Segmentation from MRI*”, Hindawi Complexity, Volume 2020, <https://doi.org/10.1155/2020/6613191>

Sujeet More, Jimmy Singla, Oh-Young Song, Usman Tariq and Sharaf Malebary, “*Denoising Medical Images Using Deep Learning in IOT Environment*”, Computer, Materials & Continua, Tech Science Press, Volume 69, Issue 3, <https://doi.org/10.32604/cmc.2021.018230>

Sujeet More and Jimmy Singla, “*Machine Learning Methods for Knee Feature Extraction from MR Images*”, International Conference on Smart Electronics and Communication (ICOSEC 2020), 10<sup>th</sup> – 12<sup>th</sup> September 2020.

Sujeet More and Jimmy Singla, “*A Study on Automated Grading System for Early Prediction of Rheumatoid Arthritis*”, 6<sup>th</sup> International Conference on Communication and Electronics Systems (ICCES 2021), 8<sup>th</sup> – 10<sup>th</sup> July 2021.

Sujeet More and Jimmy Singla, “*Machine Learning Approaches for Image Quality Improvement*”, 2<sup>nd</sup> International Conference on Image Processing and Capsule Networks (ICIPCN 2021), 27<sup>th</sup> – 28<sup>th</sup> May 2021.

Sujeet More and Jimmy Singla, “*Discrete-MultiResUNet: Segmentation and feature extraction model for knee MR images*”, Journal of Intelligent and Fuzzy Systems, Volume 41, pp 3771 – 3781, <https://doi.org/10.3233/JIFS-211459>

Sujeet More and Jimmy Singla, “*A generalized deep learning framework for automatic rheumatoid arthritis severity grading*”, Journal of Intelligent and Fuzzy Systems, Volume 41, pp 7603 – 7614, <https://doi.org/10.3233/JIFS-212015>



## Bibliography

- [1] Y. Tanaka, “Rheumatoid arthritis,” *Inflammation and Regeneration*, vol. 40, no. 1, p. 20, Dec. 2020, doi: 10.1186/s41232-020-00133-8.
- [2] T. Neogi, “The epidemiology and impact of pain in osteoarthritis,” *Osteoarthritis and Cartilage*, vol. 21, no. 9, pp. 1145–1153, Sep. 2013, doi: 10.1016/j.joca.2013.03.018.
- [3] S. A. Oliveria, D. T. Felson, J. I. Reed, P. A. Cirillo, and A. M. Walker, “Incidence of symptomatic hand, hip, and knee osteoarthritis among patients in a health maintenance organization,” *Arthritis & Rheumatism*, vol. 38, no. 8, pp. 1134–1141, Aug. 1995, doi: 10.1002/art.1780380817.
- [4] S. More and J. Singla, “Intelligent medical diagnostic systems for arthritis,” *International Journal of Recent Technology and Engineering*, vol. 8, no. 2 Special Issue 11, pp. 3626–3629, 2019, doi: 10.35940/ijrte.B1455.0982S1119.
- [5] N. Akkoc and S. Akar, “Epidemiology of rheumatoid arthritis in Turkey,” *Clinical Rheumatology*, vol. 25, no. 4, pp. 560–561, Apr. 2006, doi: 10.1007/s10067-005-0092-2.
- [6] A. J. Barr *et al.*, “The relationship between three-dimensional knee MRI bone shape and total knee replacement-A case control study: Data from the Osteoarthritis Initiative,” *Rheumatology (United Kingdom)*, vol. 55, no. 9, pp. 1585–1593, 2016, doi: 10.1093/rheumatology/kew191.
- [7] M. Byra *et al.*, “Knee menisci segmentation and relaxometry of 3D ultrashort echo time cones MR imaging using attention U-Net with transfer learning,” *Magnetic Resonance in Medicine*, vol. 83, no. 3, pp. 1109–1122, 2020, doi: 10.1002/mrm.27969.
- [8] T. A. Blackburn and E. Craig, “Knee anatomy. A brief review,” *Physical Therapy*, vol. 60, no. 12, pp. 1556–1560, Dec. 1980, doi: 10.1093/ptj/60.12.1556.
- [9] X. Hong, Z. Wang, L. Guo, X. Chan, Y. Wei, and Z. Wei, “Quantitative

- evaluation of knee cartilage and meniscus destruction in patients with rheumatoid arthritis using T1  $\rho$  and T2 mapping,” *European Journal of Radiology*, vol. 96, no. July, pp. 91–97, 2017, doi: 10.1016/j.ejrad.2017.09.018.
- [10] S. U. Jari and J. Noble, “Meniscal tearing and rheumatoid arthritis,” pp. 157–158, 2001, doi: 10.1016/S0968-0160(00)00077-6.
- [11] D. L. Scott, F. Wolfe, and T. W. J. Huizinga, “Rheumatoid arthritis,” *The Lancet*, vol. 376, no. 9746, pp. 1094–1108, 2010, doi: 10.1016/S0140-6736(10)60826-4.
- [12] C. Kokkotis, S. Moustakidis, E. Papageorgiou, G. Giakas, and D. E. Tsaopoulos, “Machine learning in knee osteoarthritis: A review,” *Osteoarthritis and Cartilage Open*, vol. 2, no. 3, p. 100069, 2020, doi: 10.1016/j.ocarto.2020.100069.
- [13] B. G. Ashinsky *et al.*, “Machine learning classification of OARSI-scored human articular cartilage using magnetic resonance imaging,” *Osteoarthritis and Cartilage*, vol. 23, no. 10, pp. 1704–1712, 2015, doi: 10.1016/j.joca.2015.05.028.
- [14] J. C. Buckland-Wright, D. G. Macfarlane, J. A. Lynch, M. R. Jasani, and C. R. Bradshaw, “Joint space width measures cartilage thickness in osteoarthritis of the knee: High resolution plain film and double contrast macroradiographic investigation,” *Annals of the Rheumatic Diseases*, vol. 54, no. 4, pp. 263–268, Apr. 1995, doi: 10.1136/ard.54.4.263.
- [15] A. J. Chaudhari *et al.*, “High-resolution <sup>18</sup>F-FDG PET/CT for assessing disease activity in rheumatoid and psoriatic arthritis: Findings of a prospective pilot study,” *British Journal of Radiology*, vol. 89, no. 1063, p. 20160138, Jul. 2016, doi: 10.1259/bjr.20160138.
- [16] A. D. do Prado *et al.*, “Ultrasound and its clinical use in rheumatoid arthritis: where do we stand?,” *Advances in rheumatology (London, England)*, vol. 58, no. 1, p. 19, Dec. 2018, doi: 10.1186/s42358-018-0023-y.
- [17] N. Boutry, M. Morel, R. M. Flipo, X. Demondion, and A. Cotten, “Early

- rheumatoid arthritis: A review of MRI and sonographic findings,” *American Journal of Roentgenology*, vol. 189, no. 6, pp. 1502–1509, Dec. 2007, doi: 10.2214/AJR.07.2548.
- [18] I. Sudoł-Szopińska, L. Jans, and J. Teh, “Reumatoidalne zapalenie stawów w badaniu MR i ultrasonografii,” *Journal of Ultrasonography*, vol. 17, no. 68, pp. 5–16, Mar. 2017, doi: 10.15557/jou.2017.0001.
- [19] J. A. Narváez, J. Narváez, E. de Lama, and M. de Albert, “MR imaging of early rheumatoid arthritis,” *Radiographics*, vol. 30, no. 1, pp. 143–163, 2010, doi: 10.1148/rg.301095089.
- [20] H. Bruder, H. Fischer, R. Graumann, and M. Deimling, “A new steady-state imaging sequence for simultaneous acquisition of two MR images with clearly different contrasts,” *Magnetic Resonance in Medicine*, vol. 7, no. 1, pp. 35–42, May 1988, doi: 10.1002/mrm.1910070105.
- [21] E. K. Lee, E. J. Lee, S. Kim, and Y. S. Lee, “Importance of contrast-enhanced fluid-attenuated inversion recovery magnetic resonance imaging in various intracranial pathologic conditions,” *Korean Journal of Radiology*, vol. 17, no. 1, pp. 127–141, 2016, doi: 10.3348/kjr.2016.17.1.127.
- [22] H. Alder *et al.*, “Computer-based diagnostic expert systems in rheumatology: Where do we stand in 2014?,” *International Journal of Rheumatology*, vol. 2014, 2014, doi: 10.1155/2014/672714.
- [23] K. J. Kim and I. Tagkopoulos, “Application of machine learning in rheumatic disease research,” *Korean Journal of Internal Medicine*, vol. 34, no. 4, pp. 708–722, 2019, doi: 10.3904/kjim.2018.349.
- [24] M. Hügler, P. Omoumi, J. M. van Laar, J. Boedecker, and T. Hügler, “Applied machine learning and artificial intelligence in rheumatology,” *Rheumatology Advances in Practice*, vol. 4, no. 1, pp. 1–10, 2021, doi: 10.1093/rap/rkaa005.
- [25] M. Botvinick, S. Ritter, J. X. Wang, Z. Kurth-Nelson, C. Blundell, and D. Hassabis, “Reinforcement Learning, Fast and Slow,” *Trends in Cognitive Sciences*, vol. 23, no. 5, pp. 408–422, May 2019, doi:

10.1016/j.tics.2019.02.006.

- [26] I. T. Jolliffe and J. Cadima, “Principal component analysis: A review and recent developments,” *Philosophical Transactions of the Royal Society A: Mathematical, Physical and Engineering Sciences*, vol. 374, no. 2065, p. 20150202, Apr. 2016, doi: 10.1098/rsta.2015.0202.
- [27] K. P. Adlassnig, H. Leitich, and G. Kolarz, “On the applicability of diagnostic criteria for the diagnosis of rheumatoid arthritis in an expert system,” *Expert Systems With Applications*, vol. 6, no. 4, pp. 441–448, Oct. 1993, doi: 10.1016/0957-4174(93)90036-6.
- [28] B. C. Stoel, “Artificial intelligence in detecting early RA,” *Seminars in Arthritis and Rheumatism*, vol. 49, no. 3, pp. S25–S28, 2019, doi: 10.1016/j.semarthrit.2019.09.020.
- [29] B. Stoel, “Use of artificial intelligence in imaging in rheumatology-current status and future perspectives,” *RMD Open*, vol. 6, no. 1, pp. 1–10, 2020, doi: 10.1136/rmdopen-2019-001063.
- [30] L. C. Parish, “An historical approach to the nomenclature of rheumatoid arthritis,” *Arthritis & Rheumatism*, vol. 6, no. 2, pp. 138–158, Apr. 1963, doi: 10.1002/art.1780060206.
- [31] D. Aletaha *et al.*, “2010 Rheumatoid arthritis classification criteria: An American College of Rheumatology/European League Against Rheumatism collaborative initiative,” *Arthritis and Rheumatism*, vol. 62, no. 9, pp. 2569–2581, 2010, doi: 10.1002/art.27584.
- [32] S. Murakami, K. Hatano, J. Tan, H. Kim, and T. Aoki, “Automatic identification of bone erosions in rheumatoid arthritis from hand radiographs based on deep convolutional neural network,” *Multimedia Tools and Applications*, vol. 77, no. 9, pp. 10921–10937, 2018, doi: 10.1007/s11042-017-5449-4.
- [33] A. E. Wluka, S. Stuckey, J. Snaddon, and F. M. Cicuttini, “The determinants of change in tibial cartilage volume in osteoarthritic knees,” *Arthritis and*

*Rheumatism*, vol. 46, no. 8, pp. 2065–2072, 2002, doi: 10.1002/art.10460.

- [34] B. Norman, V. Pedoia, and S. Majumdar, “Use of 2D U-net convolutional neural networks for automated cartilage and meniscus segmentation of knee MR imaging data to determine relaxometry and morphometry,” *Radiology*, vol. 288, no. 1, pp. 177–185, Jul. 2018, doi: 10.1148/radiol.2018172322.
- [35] R. J. Hemalatha, V. Vijaybaskar, and T. R. Thamizhvani, “Automatic localization of anatomical regions in medical ultrasound images of rheumatoid arthritis using deep learning,” *Proceedings of the Institution of Mechanical Engineers, Part H: Journal of Engineering in Medicine*, vol. 233, no. 6, pp. 657–667, Jun. 2019, doi: 10.1177/0954411919845747.
- [36] S. More, J. Singla, A. Abugabah, and A. A. Alzubi, “Machine Learning Techniques for Quantification of Knee Segmentation from MRI,” *Complexity*, vol. 2020, 2020, doi: 10.1155/2020/6613191.
- [37] B. J. Heard, J. M. Rosvold, M. J. Fritzler, H. El-Gabalawy, J. P. Wiley, and R. J. Krawetz, “A computational method to differentiate normal individuals, osteoarthritis and rheumatoid arthritis patients using serum biomarkers,” *Journal of the Royal Society Interface*, vol. 11, no. 97, 2014, doi: 10.1098/rsif.2014.0428.
- [38] I. Goldie and A. Nachemson, “Synovial ph in rheumatoid knee-joints I. The effect of synovectomy,” *Acta Orthopaedica*, vol. 40, no. 5, pp. 634–641, 1969, doi: 10.3109/17453676908989529.
- [39] R. Stahl *et al.*, “Assessment of cartilage-dedicated sequences at ultra-high-field MRI: Comparison of imaging performance and diagnostic confidence between 3.0 and 7.0 T with respect to osteoarthritis-induced changes at the knee joint,” *Skeletal Radiology*, vol. 38, no. 8, pp. 771–783, Aug. 2009, doi: 10.1007/s00256-009-0676-z.
- [40] J. Fripp, S. Crozier, S. K. Warfield, and S. Ourselin, “Automatic segmentation and quantitative analysis of the articular cartilages from magnetic resonance images of the knee,” *IEEE Transactions on Medical Imaging*, vol. 29, no. 1,

pp. 55–64, Jan. 2010, doi: 10.1109/TMI.2009.2024743.

- [41] R. Bitar *et al.*, “MR pulse sequences: What every radiologist wants to know but is afraid to ask,” *Radiographics*, vol. 26, no. 2, pp. 513–537, Mar. 2006, doi: 10.1148/rg.262055063.
- [42] M. Jarraya *et al.*, “Susceptibility artifacts detected on 3T MRI of the knee: Frequency, change over time and associations with radiographic findings: Data from the Joints on Glucosamine Study,” *Osteoarthritis and Cartilage*, vol. 22, no. 10, pp. 1499–1503, Oct. 2014, doi: 10.1016/j.joca.2014.04.014.
- [43] J. Folkesson, E. B. Dam, O. F. Olsen, P. C. Pettersen, and C. Christiansen, “Segmenting articular cartilage automatically using a voxel classification approach,” *IEEE Transactions on Medical Imaging*, vol. 26, no. 1, pp. 106–115, Jan. 2007, doi: 10.1109/TMI.2006.886808.
- [44] B. K. Paunipagar and D. D. Rasalkar, “Imaging of articular cartilage,” *Indian Journal of Radiology and Imaging*, vol. 24, no. 3, pp. 237–248, 2014, doi: 10.4103/0971-3026.137028.
- [45] P. K. Paul, M. Kris Jasani, D. Sebok, A. Rakhit, A. W. Dunton, and F. L. Douglas, “Variation in MR signal intensity across normal human knee cartilage,” *Journal of Magnetic Resonance Imaging*, vol. 3, no. 4, pp. 569–574, Jul. 1993, doi: 10.1002/jmri.1880030404.
- [46] T. G. Williams *et al.*, “Measurement and visualisation of focal cartilage thickness change by MRI in a study of knee osteoarthritis using a novel image analysis tool,” *British Journal of Radiology*, vol. 83, no. 995, pp. 940–948, 2010, doi: 10.1259/bjr/68875123.
- [47] D. A. Binks *et al.*, “Potential role of the posterior cruciate ligament synovio-entheseseal complex in joint effusion in early osteoarthritis: a magnetic resonance imaging and histological evaluation of cadaveric tissue and data from the Osteoarthritis Initiative,” *Osteoarthritis and cartilage / OARS, Osteoarthritis Research Society*, vol. 22, no. 9, pp. 1310–1317, Sep. 2014, doi: 10.1016/j.joca.2014.06.037.

- [48] F. Eckstein, F. Cicuttini, J. P. Raynauld, J. C. Waterton, and C. Peterfy, “Magnetic resonance imaging (MRI) of articular cartilage in knee osteoarthritis (OA): morphological assessment,” *Osteoarthritis and Cartilage*, vol. 14, no. SUPPL. 1, pp. 46–75, 2006, doi: 10.1016/j.joca.2006.02.026.
- [49] E. B. Dam *et al.*, “Identification of progressors in osteoarthritis by combining biochemical and MRI-based markers,” *Arthritis Research and Therapy*, vol. 11, no. 4, p. R115, 2009, doi: 10.1186/ar2774.
- [50] P. R. Kornaat *et al.*, “MR imaging of articular cartilage at 1.5T and 3.0T: Comparison of SPGR and SSFP sequences,” *Osteoarthritis and Cartilage*, vol. 13, no. 4, pp. 338–344, 2005, doi: 10.1016/j.joca.2004.12.008.
- [51] A. L. Samuel, “Some studies in machine learning using the game of checkers,” *IBM Journal of Research and Development*, vol. 44, no. 1–2, pp. 207–219, Jul. 2000, doi: 10.1147/rd.441.0206.
- [52] H. Sharon, I. Elamvazuthi, C. K. Lu, S. Parasuraman, and E. Natarajan, “Development of rheumatoid arthritis classification from electronic image sensor using ensemble method,” *Sensors (Switzerland)*, vol. 20, no. 1, p. 167, Dec. 2020, doi: 10.3390/s20010167.
- [53] T. Fawcett, “An introduction to ROC analysis,” *Pattern Recognition Letters*, vol. 27, no. 8, pp. 861–874, Jun. 2006, doi: 10.1016/j.patrec.2005.10.010.
- [54] N. Basu, G. T. Jones, G. J. Macfarlane, and K. L. Druce, “Identification and Validation of Clinically Relevant Clusters of Severe Fatigue in Rheumatoid Arthritis,” *Psychosomatic Medicine*, vol. 79, no. 9, pp. 1051–1058, Nov. 2017, doi: 10.1097/PSY.0000000000000498.
- [55] Y. C. Lee *et al.*, “Subgrouping of patients with rheumatoid arthritis based on pain, fatigue, inflammation, and psychosocial factors,” *Arthritis and Rheumatology*, vol. 66, no. 8, pp. 2006–2014, Aug. 2014, doi: 10.1002/art.38682.
- [56] R. Bro and A. K. Smilde, “Principal component analysis,” *Analytical Methods*, vol. 6, no. 9, pp. 2812–2831, 2014, doi: 10.1039/c3ay41907j.

- [57] A. E. Ilesanmi and T. O. Ilesanmi, “Methods for image denoising using convolutional neural network : a review,” *Complex & Intelligent Systems*, no. 0123456789, 2021, doi: 10.1007/s40747-021-00428-4.
- [58] P. Chen, L. Gao, X. Shi, K. Allen, and L. Yang, “Fully automatic knee osteoarthritis severity grading using deep neural networks with a novel ordinal loss,” *Computerized Medical Imaging and Graphics*, vol. 75, pp. 84–92, 2019, doi: 10.1016/j.compmedimag.2019.06.002.
- [59] Y. Zhang, Z. Yang, J. Hu, S. Zou, and Y. Fu, “MRI Denoising Using Low Rank Prior and Sparse Gradient Prior,” *IEEE Access*, vol. 7, pp. 45858–45865, 2019, doi: 10.1109/ACCESS.2019.2907637.
- [60] H. Wang, R. Zheng, F. Dai, Q. Wang, and C. Wang, “High-field mr diffusion-weighted image denoising using a joint denoising convolutional neural network,” *Journal of Magnetic Resonance Imaging*, vol. 50, no. 6, pp. 1937–1947, 2019, doi: 10.1002/jmri.26761.
- [61] S. Biswas, H. K. Aggarwal, and M. Jacob, “Dynamic MRI using model-based deep learning and SToRM priors: MoDL-SToRM,” *Magnetic Resonance in Medicine*, vol. 82, no. 1, pp. 485–494, 2019, doi: 10.1002/mrm.27706.
- [62] M. Ran *et al.*, “Denoising of 3D magnetic resonance images using a residual encoder–decoder Wasserstein generative adversarial network,” *Medical Image Analysis*, vol. 55, pp. 165–180, 2019, doi: 10.1016/j.media.2019.05.001.
- [63] J. Chen, G. Zhang, S. Xu, and H. Yu, “A blind CNN denoising model for random-valued impulse noise,” *IEEE Access*, vol. 7, pp. 124647–124661, 2019, doi: 10.1109/ACCESS.2019.2938799.
- [64] M. T. Islam, S. M. Mahbubur Rahman, M. Omair Ahmad, and M. N. S. Swamy, “Mixed Gaussian-impulse noise reduction from images using convolutional neural network,” *Signal Processing: Image Communication*, vol. 68, pp. 26–41, Oct. 2018, doi: 10.1016/j.image.2018.06.016.
- [65] D. Yin *et al.*, “Speckle noise reduction in coherent imaging based on deep learning without clean data,” *Optics and Lasers in Engineering*, vol. 133, p.



106151, Oct. 2020, doi: 10.1016/j.optlaseng.2020.106151.

- [66] Q. Zhang, Q. Yuan, J. Li, F. Sun, and L. Zhang, “Deep spatio-spectral Bayesian posterior for hyperspectral image non-i.i.d. noise removal,” *ISPRS Journal of Photogrammetry and Remote Sensing*, vol. 164, pp. 125–137, Jun. 2020, doi: 10.1016/j.isprsjprs.2020.04.010.
- [67] E. Giannatou, G. Papavieros, V. Constantoudis, H. Papageorgiou, and E. Gogolides, “Deep learning denoising of SEM images towards noise-reduced LER measurements,” *Microelectronic Engineering*, vol. 216, p. 111051, Aug. 2019, doi: 10.1016/j.mee.2019.111051.
- [68] X. Feng, Q. Huang, and X. Li, “Ultrasound image de-speckling by a hybrid deep network with transferred filtering and structural prior,” *Neurocomputing*, vol. 414, pp. 346–355, Nov. 2020, doi: 10.1016/j.neucom.2020.09.002.
- [69] P. Kokil and S. Sudharson, “Despeckling of clinical ultrasound images using deep residual learning,” *Computer Methods and Programs in Biomedicine*, vol. 194, p. 105477, Oct. 2020, doi: 10.1016/j.cmpb.2020.105477.
- [70] H. J. Kim and D. Lee, “Image denoising with conditional generative adversarial networks (CGAN) in low dose chest images,” *Nuclear Instruments and Methods in Physics Research, Section A: Accelerators, Spectrometers, Detectors and Associated Equipment*, vol. 954, p. 161914, Feb. 2020, doi: 10.1016/j.nima.2019.02.041.
- [71] P. C. Tripathi and S. Bag, “CNN-DMRI: A Convolutional Neural Network for Denoising of Magnetic Resonance Images,” *Pattern Recognition Letters*, vol. 135, pp. 57–63, Jul. 2020, doi: 10.1016/j.patrec.2020.03.036.
- [72] S. Yu, T. Zhang, C. Ma, L. Zhou, J. Yang, and X. He, “Learning a discriminative dictionary with CNN for image classification,” *Lecture Notes in Computer Science (including subseries Lecture Notes in Artificial Intelligence and Lecture Notes in Bioinformatics)*, vol. 9948 LNCS, pp. 185–194, 2016, doi: 10.1007/978-3-319-46672-9\_22.
- [73] K. Srinivasan and N. Muthu, “A Comparative Study and Analysis of Contrast

- Enhancement Algorithms for MRI Brain Image Sequences,” *2018 9th International Conference on Computing, Communication and Networking Technologies, ICCCNT 2018*, pp. 1–7, 2018, doi: 10.1109/ICCCNT.2018.8494068.
- [74] A. Senthil Selvi and R. Sukumar, “Removal of salt and pepper noise from images using hybrid filter (HF) and fuzzy logic noise detector (FLND),” *Concurrency Computation*, vol. 31, no. 12, pp. 3–12, 2019, doi: 10.1002/cpe.4501.
- [75] M. Sahnoun *et al.*, “A Modified DWT-SVD Algorithm for T1-w Brain MR Images Contrast Enhancement,” *Irbm*, vol. 40, no. 4, pp. 235–243, 2019, doi: 10.1016/j.irbm.2019.04.007.
- [76] K. Chen, X. Lin, X. Hu, J. Wang, H. Zhong, and L. Jiang, “An enhanced adaptive non-local means algorithm for Rician noise reduction in magnetic resonance brain images,” *BMC Medical Imaging*, vol. 20, no. 1, pp. 1–9, 2020, doi: 10.1186/s12880-019-0407-4.
- [77] H. M. Rai and K. Chatterjee, “Hybrid adaptive algorithm based on wavelet transform and independent component analysis for denoising of MRI images,” *Measurement: Journal of the International Measurement Confederation*, vol. 144, pp. 72–82, 2019, doi: 10.1016/j.measurement.2019.05.028.
- [78] P. G. Kuppusamy, S. Jayaraman, and J. Joseph, “A customized nonlocal restoration scheme with adaptive strength of smoothening for magnetic resonance images,” *Biomedical Signal Processing and Control*, vol. 49, pp. 160–172, 2019, doi: 10.1016/j.bspc.2018.12.012.
- [79] I. Nagarajan and G. G. Lakshmi Priya, “Removal of noise in MRI images using a block difference-based filtering approach,” *International Journal of Imaging Systems and Technology*, vol. 30, no. 1, pp. 203–215, 2020, doi: 10.1002/ima.22361.
- [80] N. Mittal, A. Raj, and H. Goyal, “Enhancement and Removal of Noise from Medical Images by Wavelet Transform Method,” *Proceedings of the 3rd*

*International Conference on Electronics and Communication and Aerospace Technology, ICECA 2019*, pp. 1126–1130, 2019, doi: 10.1109/ICECA.2019.8821979.

- [81] V. Magudeeswaran, C. G. Ravichandran, and P. Thirumurugan, “Brightness preserving bi-level fuzzy histogram equalization for MRI brain image contrast enhancement,” *International Journal of Imaging Systems and Technology*, vol. 27, no. 2, pp. 153–161, 2017, doi: 10.1002/ima.22219.
- [82] H. Lv and R. Wang, “Denoising 3D Magnetic Resonance Images Based on Low-Rank Tensor Approximation With Adaptive Multirank Estimation,” *IEEE Access*, vol. 7, pp. 85995–86003, 2019, doi: 10.1109/ACCESS.2019.2924907.
- [83] K. Kumar Sharma, D. Gurjar, M. Jyotyana, and V. Kumari, “Denoising of Brain MRI Images Using a Hybrid Filter Method of Sylvester-Lyapunov Equation and Non Local Means,” *Advances in Intelligent Systems and Computing*, vol. 851, pp. 495–505, 2019, doi: 10.1007/978-981-13-2414-7\_46.
- [84] P. Kandhway, A. K. Bhandari, and A. Singh, “A novel reformed histogram equalization based medical image contrast enhancement using krill herd optimization,” *Biomedical Signal Processing and Control*, vol. 56, p. 101677, 2020, doi: 10.1016/j.bspc.2019.101677.
- [85] X. You, N. Cao, H. Lu, M. Mao, and W. Wang, “Denoising of MR images with Rician noise using a wider neural network and noise range division,” *Magnetic Resonance Imaging*, vol. 64, no. May, pp. 154–159, 2019, doi: 10.1016/j.mri.2019.05.042.
- [86] M. Elhoseny and K. Shankar, “Optimal bilateral filter and Convolutional Neural Network based denoising method of medical image measurements,” *Measurement: Journal of the International Measurement Confederation*, vol. 143, pp. 125–135, 2019, doi: 10.1016/j.measurement.2019.04.072.
- [87] V. Hanchate and K. Joshi, “MRI denoising using BM3D equipped with noise invalidation denoising technique and VST for improved contrast,” *SN Applied Sciences*, vol. 2, no. 2, 2020, doi: 10.1007/s42452-020-1937-7.

- [88] I. S. Isa, S. N. Sulaiman, M. Mustapha, and N. K. Karim, "Automatic contrast enhancement of brain MR images using Average Intensity Replacement based on Adaptive Histogram Equalization (AIR-AHE)," *Biocybernetics and Biomedical Engineering*, vol. 37, no. 1, pp. 24–34, 2017, doi: 10.1016/j.bbe.2016.12.003.
- [89] P. R. Desai and I. Hacihaliloglu, "Enhancement and automated segmentation of ultrasound knee cartilage for early diagnosis of knee osteoarthritis," *Proceedings - International Symposium on Biomedical Imaging*, vol. 2018-April, no. Isbi, pp. 1471–1474, 2018, doi: 10.1109/ISBI.2018.8363850.
- [90] F. Ambellan, A. Tack, M. Ehlke, and S. Zachow, "Automated segmentation of knee bone and cartilage combining statistical shape knowledge and convolutional neural networks: Data from the Osteoarthritis Initiative," *Medical Image Analysis*, vol. 52, pp. 109–118, Feb. 2019, doi: 10.1016/j.media.2018.11.009.
- [91] M. Marčan and I. Voiculescu, "Unsupervised segmentation of MRI knees using image partition forests," *Medical Imaging 2016: Biomedical Applications in Molecular, Structural, and Functional Imaging*, vol. 9788, p. 97880D, 2016, doi: 10.1117/12.2216696.
- [92] H. P. Ng, S. H. Ong, K. W. C. Foong, P. S. Goh, and W. L. Nowinski, "Medical image segmentation using k-means clustering and improved watershed algorithm," *Proceedings of the IEEE Southwest Symposium on Image Analysis and Interpretation*, vol. 2006, pp. 61–65, 2006, doi: 10.1109/ssiai.2006.1633722.
- [93] V. Grau, A. U. J. Mewes, M. Alcañiz, R. Kikinis, and S. K. Warfield, "Improved watershed transform for medical image segmentation using prior information," *IEEE Transactions on Medical Imaging*, vol. 23, no. 4, pp. 447–458, 2004, doi: 10.1109/TMI.2004.824224.
- [94] M. S. Swanson *et al.*, "Semi-automated segmentation to assess the lateral meniscus in normal and osteoarthritic knees," *Osteoarthritis and Cartilage*,

vol. 18, no. 3, pp. 344–353, 2010, doi: 10.1016/j.joca.2009.10.004.

- [95] Z. Wang, C. Donoghue, and D. Rueckert, “Patch-based segmentation without registration: Application to knee MRI,” *Lecture Notes in Computer Science (including subseries Lecture Notes in Artificial Intelligence and Lecture Notes in Bioinformatics)*, vol. 8184 LNCS, pp. 98–105, 2013, doi: 10.1007/978-3-319-02267-3\_13.
- [96] K. Zhang, J. Deng, and W. Lu, “Segmenting human knee cartilage automatically from multi-contrast MR images using support vector machines and discriminative random fields,” *Proceedings - International Conference on Image Processing, ICIP*, pp. 721–724, 2011, doi: 10.1109/ICIP.2011.6116655.
- [97] M. A. Baldwin, J. E. Langenderfer, P. J. Rullkoetter, and P. J. Laz, “Development of subject-specific and statistical shape models of the knee using an efficient segmentation and mesh-morphing approach,” *Computer Methods and Programs in Biomedicine*, vol. 97, no. 3, pp. 232–240, 2010, doi: 10.1016/j.cmpb.2009.07.005.
- [98] A. Faisal, S. C. Ng, S. L. Goh, J. George, E. Supriyanto, and K. W. Lai, “Multiple LREK Active Contours for Knee Meniscus Ultrasound Image Segmentation,” *IEEE Transactions on Medical Imaging*, vol. 34, no. 10, pp. 2162–2171, 2015, doi: 10.1109/TMI.2015.2425144.
- [99] H. S. Gan, A. H. A. Karim, K. A. Sayuti, T. S. Tan, and M. R. A. Kadir, “Analysis of parameters’ effects in semi-automated knee cartilage segmentation model: Data from the osteoarthritis initiative,” *AIP Conference Proceedings*, vol. 1775, 2016, doi: 10.1063/1.4965172.
- [100] A. Faisal, S. C. Ng, S. L. Goh, and K. W. Lai, “Knee cartilage segmentation and thickness computation from ultrasound images,” *Medical and Biological Engineering and Computing*, vol. 56, no. 4, pp. 657–669, 2018, doi: 10.1007/s11517-017-1710-2.
- [101] A. Prason, K. Petersen, C. Igel, F. Lauze, E. Dam, and M. Nielsen, “Deep feature learning for knee cartilage segmentation using a triplanar convolutional

- neural network,” *Lecture Notes in Computer Science (including subseries Lecture Notes in Artificial Intelligence and Lecture Notes in Bioinformatics)*, vol. 8150 LNCS, no. PART 2, pp. 246–253, 2013, doi: 10.1007/978-3-642-40763-5\_31.
- [102] Z. Zhou, G. Zhao, R. Kijowski, and F. Liu, “Deep convolutional neural network for segmentation of knee joint anatomy,” *Magnetic Resonance in Medicine*, vol. 80, no. 6, pp. 2759–2770, 2018, doi: 10.1002/mrm.27229.
- [103] K. Zhang, W. Lu, and P. Marziliano, “Automatic knee cartilage segmentation from multi-contrast MR images using support vector machine classification with spatial dependencies,” *Magnetic Resonance Imaging*, vol. 31, no. 10, pp. 1731–1743, 2013, doi: 10.1016/j.mri.2013.06.005.
- [104] C. N. Öztürk and S. Albayrak, “Automatic segmentation of cartilage in high-field magnetic resonance images of the knee joint with an improved voxel-classification-driven region-growing algorithm using vicinity-correlated subsampling,” *Computers in Biology and Medicine*, vol. 72, pp. 90–107, 2016, doi: 10.1016/j.compbiomed.2016.03.011.
- [105] H. Seim, D. Kainmueller, H. Lamecker, M. Bindernagel, J. Malinowski, and S. Zachow, “Model-based Auto-Segmentation of Knee Bones and Cartilage in MRI Data,” *Proc. of Medical Image Computing and Computer-Assisted Intervention (MICCAI); Medical Image Analysis for the Clinic: A Grand Challenge*, pp. 215–223, 2010.
- [106] C. Ahn, T. D. Bui, Y. W. Lee, J. Shin, and H. Park, “Fully automated, level set-based segmentation for knee MRIs using an adaptive force function and template: Data from the osteoarthritis initiative,” *BioMedical Engineering Online*, vol. 15, no. 1, pp. 1–14, 2016, doi: 10.1186/s12938-016-0225-7.
- [107] H. Bakir and J. Zrida, “Automatic knee cartilage segmentation and visualization,” *Proceedings of the 2014 International Conference on Advances in Computing, Communications and Informatics, ICACCI 2014*, pp. 1867–1870, 2014, doi: 10.1109/ICACCI.2014.6968291.

- [108] J. Folkesson, O. F. Olsen, P. Pettersen, E. Dam, and C. Christiansen, "Combining binary classifiers for automatic cartilage segmentation in knee MRI," *Lecture Notes in Computer Science (including subseries Lecture Notes in Artificial Intelligence and Lecture Notes in Bioinformatics)*, vol. 3765 LNCS, pp. 230–239, 2005, doi: 10.1007/11569541\_24.
- [109] J. G. Lee, S. Gumus, C. H. Moon, C. K. Kwoh, and K. T. Bae, "Fully automated segmentation of cartilage from the MR images of knee using a multi-atlas and local structural analysis method," *Medical Physics*, vol. 41, no. 9, 2014, doi: 10.1118/1.4893533.
- [110] C. Kauffmann *et al.*, "Computer-aided method for quantification of cartilage thickness and volume changes using MRI: Validation study using a synthetic model," *IEEE Transactions on Biomedical Engineering*, vol. 50, no. 8, pp. 978–988, 2003, doi: 10.1109/TBME.2003.814539.
- [111] J. Tang, S. Millington, S. T. Acton, J. Crandall, and S. Hurwitz, "Surface extraction and thickness measurement of the articular cartilage from MR images using directional gradient vector flow snakes," *IEEE Transactions on Biomedical Engineering*, vol. 53, no. 5, pp. 896–907, 2006, doi: 10.1109/TBME.2006.872816.
- [112] A. Tack, A. Mukhopadhyay, and S. Zachow, "Knee menisci segmentation using convolutional neural networks: data from the Osteoarthritis Initiative," *Osteoarthritis and Cartilage*, vol. 26, no. 5, pp. 680–688, 2018, doi: 10.1016/j.joca.2018.02.907.
- [113] L. Shan, C. Zach, C. Charles, and M. Niethammer, "Automatic atlas-based three-label cartilage segmentation from MR knee images," *Medical Image Analysis*, vol. 18, no. 7, pp. 1233–1246, 2014, doi: 10.1016/j.media.2014.05.008.
- [114] A. Raj, S. Vishwanathan, B. Ajani, K. Krishnan, and H. Agarwal, "Automatic knee cartilage segmentation using fully volumetric convolutional neural networks for evaluation of osteoarthritis," in *Proceedings - International*

*Symposium on Biomedical Imaging*, 2018, vol. 2018-April, no. Isbi, pp. 851–854, doi: 10.1109/ISBI.2018.8363705.

- [115] C. Lindner, S. Thiagarajah, J. M. Wilkinson, G. A. Wallis, and T. F. Cootes, “Fully automatic segmentation of the proximal femur using random forest regression voting,” *IEEE Transactions on Medical Imaging*, vol. 32, no. 8, pp. 1462–1472, 2013, doi: 10.1109/TMI.2013.2258030.
- [116] S. Kashyap, I. Oguz, H. Zhang, and M. Sonka, “Automated segmentation of knee MRI using hierarchical classifiers and just enough interaction based learning: Data from osteoarthritis initiative,” *arXiv*, vol. 1, pp. 344–351, 2019, doi: 10.1007/978-3-319-46723-8.
- [117] E. B. Dam, M. Lillholm, J. Marques, and M. Nielsen, “Automatic segmentation of high- and low-field knee MRIs using knee image quantification with data from the osteoarthritis initiative,” *Journal of Medical Imaging*, vol. 2, no. 2, p. 024001, 2015, doi: 10.1117/1.jmi.2.2.024001.
- [118] C. Chu, J. Bai, X. Wu, and G. Zheng, “MASCG: Multi-Atlas Segmentation Constrained Graph method for accurate segmentation of hip CT images,” *Medical Image Analysis*, vol. 26, no. 1, pp. 173–184, 2015, doi: 10.1016/j.media.2015.08.011.
- [119] A. Gandhamal, S. Talbar, S. Gajre, R. Razak, A. F. M. Hani, and D. Kumar, “Fully automated subchondral bone segmentation from knee MR images: Data from the Osteoarthritis Initiative,” *Computers in Biology and Medicine*, vol. 88, pp. 110–125, 2017, doi: 10.1016/j.combiomed.2017.07.008.
- [120] B. G. Ashinsky *et al.*, “Predicting early symptomatic osteoarthritis in the human knee using machine learning classification of magnetic resonance images from the osteoarthritis initiative,” *Journal of Orthopaedic Research*, vol. 35, no. 10, pp. 2243–2250, 2017, doi: 10.1002/jor.23519.
- [121] S. Gaj, M. Yang, K. Nakamura, and X. Li, “Automated cartilage and meniscus segmentation of knee MRI with conditional generative adversarial networks,” *Magnetic Resonance in Medicine*, vol. 84, no. 1, pp. 437–449, 2020, doi:



10.1002/mrm.28111.

- [122] V. Pedoia, B. Norman, S. N. Mehany, M. D. Bucknor, T. M. Link, and S. Majumdar, “3D convolutional neural networks for detection and severity staging of meniscus and PFJ cartilage morphological degenerative changes in osteoarthritis and anterior cruciate ligament subjects,” *Journal of Magnetic Resonance Imaging*, vol. 49, no. 2, pp. 400–410, 2019, doi: 10.1002/jmri.26246.
- [123] K. Zhang, W. Lu, and P. Marziliano, “The unified extreme learning machines and discriminative random fields for automatic knee cartilage and meniscus segmentation from multi-contrast MR images,” *Machine Vision and Applications*, vol. 24, no. 7, pp. 1459–1472, 2013, doi: 10.1007/s00138-012-0466-9.
- [124] E. S. Choi, J. A. Sim, Y. G. Na, J. K. Seon, and H. D. Shin, “Machine-learning algorithm that can improve the diagnostic accuracy of septic arthritis of the knee,” *Knee Surgery, Sports Traumatology, Arthroscopy*, no. 0123456789, 2021, doi: 10.1007/s00167-020-06418-2.
- [125] I. Iqbal, G. Shahzad, N. Rafiq, G. Mustafa, and J. Ma, “Deep learning-based automated detection of human knee joint’s synovial fluid from magnetic resonance images with transfer learning,” *IET Image Processing*, vol. 14, no. 10, pp. 1990–1998, 2020, doi: 10.1049/iet-ipr.2019.1646.
- [126] T. A. Perry *et al.*, “Measurement of synovial tissue volume in knee osteoarthritis using a semiautomated MRI-based quantitative approach,” *Magnetic Resonance in Medicine*, vol. 81, no. 5, pp. 3056–3064, 2019, doi: 10.1002/mrm.27633.
- [127] N. Bien *et al.*, “Deep-learning-assisted diagnosis for knee magnetic resonance imaging: Development and retrospective validation of MRNet,” *PLoS Medicine*, vol. 15, no. 11, pp. 1–19, 2018, doi: 10.1371/journal.pmed.1002699.
- [128] A. Saygılı and S. Albayrak, “A new computer-based approach for fully automated segmentation of knee meniscus from magnetic resonance images,”

*Biocybernetics and Biomedical Engineering*, vol. 37, no. 3, pp. 432–442, 2017, doi: 10.1016/j.bbe.2017.04.008.

- [129] I. Štajduhar, M. Mamula, D. Miletić, and G. Ünal, “Semi-automated detection of anterior cruciate ligament injury from MRI,” *Computer Methods and Programs in Biomedicine*, vol. 140, pp. 151–164, 2017, doi: 10.1016/j.cmpb.2016.12.006.
- [130] R. Cheng *et al.*, “Fully automated patellofemoral MRI segmentation using holistically nested networks: Implications for evaluating patellofemoral osteoarthritis, pain, injury, pathology, and adolescent development,” *Magnetic Resonance in Medicine*, vol. 83, no. 1, pp. 139–153, 2020, doi: 10.1002/mrm.27920.
- [131] E. B. Dam, J. Runhaar, S. Bierma-Zienstra, and M. Karsdal, “Cartilage cavity—an MRI marker of cartilage lesions in knee OA with Data from CCBR, OAI, and PROOF,” *Magnetic Resonance in Medicine*, vol. 80, no. 3, pp. 1219–1232, 2018, doi: 10.1002/mrm.27130.
- [132] F. Liu, Z. Zhou, H. Jang, A. Samsonov, G. Zhao, and R. Kijowski, “Deep convolutional neural network and 3D deformable approach for tissue segmentation in musculoskeletal magnetic resonance imaging,” *Magnetic Resonance in Medicine*, vol. 79, no. 4, pp. 2379–2391, 2018, doi: 10.1002/mrm.26841.
- [133] T. Yang, H. Zhu, X. Gao, Y. Zhang, Y. Hui, and F. Wang, “Grading of metacarpophalangeal rheumatoid arthritis on ultrasound images using machine learning algorithms,” *IEEE Access*, vol. 8, pp. 67137–67146, 2020, doi: 10.1109/ACCESS.2020.2982027.
- [134] J. Antony, K. McGuinness, N. E. O’Connor, and K. Moran, “Quantifying radiographic knee osteoarthritis severity using deep convolutional neural networks,” *Proceedings - International Conference on Pattern Recognition*, vol. 0, pp. 1195–1200, 2016, doi: 10.1109/ICPR.2016.7899799.
- [135] Y. Du, J. Shan, R. Almajalid, and M. Zhang, “Knee osteoarthritis severity level

- classification using whole knee cartilage damage index and ANN,” *Proceedings - 2018 IEEE/ACM International Conference on Connected Health: Applications, Systems and Engineering Technologies, CHASE 2018*, pp. 19–21, 2019, doi: 10.1145/3278576.3278585.
- [136] H. Dehghani, Y. Feng, D. Lighter, L. Zhang, and Y. Wang, “Deep neural networks improve diagnostic accuracy of rheumatoid arthritis using diffuse optical tomography,” *Optics InfoBase Conference Papers*, vol. Part F142-, 2019, doi: 10.1117/12.2526787.
- [137] K. Üreten, H. Erbay, and H. H. Maraş, “Detection of rheumatoid arthritis from hand radiographs using a convolutional neural network,” *Clinical Rheumatology*, vol. 39, no. 4, pp. 969–974, 2020, doi: 10.1007/s10067-019-04487-4.
- [138] B. Liu, J. Luo, and H. Huang, “Toward automatic quantification of knee osteoarthritis severity using improved Faster R-CNN,” *International Journal of Computer Assisted Radiology and Surgery*, vol. 15, no. 3, pp. 457–466, 2020, doi: 10.1007/s11548-019-02096-9.
- [139] K. A. Thomas *et al.*, “Automated Classification of Radiographic Knee Osteoarthritis Severity Using Deep Neural Networks,” *Radiology: Artificial Intelligence*, vol. 2, no. 2, p. e190065, 2020, doi: 10.1148/ryai.2020190065.
- [140] B. Norman, V. Padoia, A. Noworolski, T. M. Link, and S. Majumdar, “Applying Densely Connected Convolutional Neural Networks for Staging Osteoarthritis Severity from Plain Radiographs,” *Journal of Digital Imaging*, vol. 32, no. 3, pp. 471–477, 2019, doi: 10.1007/s10278-018-0098-3.
- [141] J. Antony, K. McGuinness, K. Moran, and N. E. O’Connor, “Automatic detection of knee joints and quantification of knee osteoarthritis severity using convolutional neural networks,” *arXiv*, vol. 1, pp. 376–390, 2017, doi: 10.1007/978-3-319-62416-7.
- [142] S. D. H. Dang and L. Allison, “Using Deep Learning to Assign Rheumatoid Arthritis Scores,” *Proceedings - 2020 IEEE 21st International Conference on*

*Information Reuse and Integration for Data Science, IRI 2020*, no. 2, pp. 399–402, 2020, doi: 10.1109/IRI49571.2020.00065.

- [143] J. Chung Wai Cheung, Y. Chow TAM, L. Chun CHAN, and P. Keung CHAN Queen Mary Hospital Chunyi WEN, “Convolutional Neural Network-Based Automatic Measurement of Joint Space Width to Predict Radiographic Severity and Progression of Knee Osteoarthritis,” pp. 1–14, 2021.
- [144] T. Hirano *et al.*, “Development and validation of a deep-learning model for scoring of radiographic finger joint destruction in rheumatoid arthritis,” *Rheumatology Advances in Practice*, vol. 3, no. 2, pp. 1–8, 2019, doi: 10.1093/rap/rkz047.
- [145] J. Rohrbach, T. Reinhard, B. Sick, and O. Dürr, “Bone erosion scoring for rheumatoid arthritis with deep convolutional neural networks,” *Computers and Electrical Engineering*, vol. 78, pp. 472–481, 2019, doi: 10.1016/j.compeleceng.2019.08.003.
- [146] R. T. Wahyuningrum, L. Anifah, I. K. Eddy Purnama, and M. Hery Purnomo, “A New Approach to Classify Knee Osteoarthritis Severity from Radiographic Images based on CNN-LSTM Method,” *2019 IEEE 10th International Conference on Awareness Science and Technology, iCAST 2019 - Proceedings*, pp. 1–6, 2019, doi: 10.1109/ICAwST.2019.8923284.
- [147] S. Shanmugam and J. Preethi, “Design of rheumatoid arthritis predictor model using machine learning algorithms,” *SpringerBriefs in Applied Sciences and Technology*, no. 9789811066979, pp. 67–77, 2018, doi: 10.1007/978-981-10-6698-6\_7.
- [148] H. H. Nguyen, S. Saarakkala, M. B. Blaschko, and A. Tiulpin, “Semixup: In-And Out-of-Manifold Regularization for Deep Semi-Supervised Knee Osteoarthritis Severity Grading from Plain Radiographs,” *IEEE Transactions on Medical Imaging*, vol. 39, no. 12, pp. 4346–4356, 2020, doi: 10.1109/TMI.2020.3017007.
- [149] S. More *et al.*, “Security Assured CNN-Based Model for Reconstruction of

- Medical Images on the Internet of Healthcare Things,” *IEEE Access*, vol. 8, pp. 126333–126346, 2020, doi: 10.1109/ACCESS.2020.3006346.
- [150] S. More, J. Singla, O.-Y. Song, U. Tariq, and S. Malebary, “Denoising Medical Images Using Deep Learning in IoT Environment,” *Computers, Materials & Continua*, vol. 69, no. 3, pp. 3127–3143, 2021, doi: 10.32604/cmc.2021.018230.
- [151] S. More and J. Singla, “A Study on Automated Grading System for Early Prediction of Rheumatoid Arthritis,” *Proceedings of the 6th International Conference on Communication and Electronics Systems, ICCES 2021*, pp. 1293–1300, 2021, doi: 10.1109/ICCES51350.2021.9489144.
- [152] X. Gu, Z. Shen, J. Xue, Y. Fan, and T. Ni, “Brain Tumor MR Image Classification Using Convolutional Dictionary Learning With Local Constraint,” *Frontiers in Neuroscience*, vol. 15, no. May, pp. 1–12, 2021, doi: 10.3389/fnins.2021.679847.
- [153] Y. Gu and K. Li, “A Transfer Model Based on Supervised Multi-Layer Dictionary Learning for Brain Tumor MRI Image Recognition,” *Frontiers in Neuroscience*, vol. 15, no. May, pp. 1–10, 2021, doi: 10.3389/fnins.2021.687496.
- [154] K. Dabov, A. Foi, V. Katkovnik, and K. Egiazarian, “Image denoising by sparse 3-D transform-domain collaborative filtering,” *IEEE Transactions on Image Processing*, vol. 16, no. 8, pp. 2080–2095, Aug. 2007, doi: 10.1109/TIP.2007.901238.
- [155] Y. Chen and T. Pock, “Trainable Nonlinear Reaction Diffusion: A Flexible Framework for Fast and Effective Image Restoration,” *IEEE Transactions on Pattern Analysis and Machine Intelligence*, vol. 39, no. 6, pp. 1256–1272, Jun. 2017, doi: 10.1109/TPAMI.2016.2596743.
- [156] K. Zhang, W. Zuo, Y. Chen, D. Meng, and L. Zhang, “Beyond a Gaussian denoiser: Residual learning of deep CNN for image denoising,” *IEEE Transactions on Image Processing*, vol. 26, no. 7, pp. 3142–3155, Jul. 2017,

doi: 10.1109/TIP.2017.2662206.

- [157] S. Gai and Z. Bao, “New image denoising algorithm via improved deep convolutional neural network with perceptive loss,” *Expert Systems with Applications*, vol. 138, p. 112815, Dec. 2019, doi: 10.1016/j.eswa.2019.07.032.
- [158] A. Tiulpin, J. Thevenot, E. Rahtu, P. Lehenkari, and S. Saarakkala, “Automatic knee osteoarthritis diagnosis from plain radiographs: A deep learning-based approach,” *Scientific Reports*, vol. 8, no. 1, pp. 1–10, 2018, doi: 10.1038/s41598-018-20132-7.
- [159] D. Saini, T. Chand, D. K. Chouhan, and M. Prakash, “A comparative analysis of automatic classification and grading methods for knee osteoarthritis focussing on X-ray images,” *Biocybernetics and Biomedical Engineering*, vol. 41, no. 2, pp. 419–444, 2021, doi: 10.1016/j.bbe.2021.03.002.
- [160] S. More and J. Singla, “Discrete-MultiResUNet: Segmentation and feature extraction model for knee MR images,” *Journal of Intelligent & Fuzzy Systems*, vol. 41, no. 2, pp. 3771–3781, 2021, doi: 10.3233/jifs-211459.
- [161] H. Sharon, I. Elamvazuthi, C. K. Lu, S. Parasuraman, and E. Natarajan, “Development of rheumatoid arthritis classification from electronic image sensor using ensemble method,” *Sensors (Switzerland)*, vol. 20, no. 1, pp. 1–26, 2020, doi: 10.3390/s20010167.
- [162] A. Tiulpin and S. Saarakkala, “Automatic grading of individual knee osteoarthritis features in plain radiographs using deep convolutional neural networks,” *arXiv*, pp. 1–12, 2019, doi: 10.3390/diagnostics10110932.
- [163] H. Oka *et al.*, “Fully automatic quantification of knee osteoarthritis severity on plain radiographs,” *Osteoarthritis and Cartilage*, vol. 16, no. 11, pp. 1300–1306, 2008, doi: 10.1016/j.joca.2008.03.011.